

LA-UR-01-3096

*Approved for public release;  
distribution is unlimited.*

*Title:* COMPREHENSIVE STUDY OF THE  
GEOSYNCHRONOUS PLASMA ENVIRONMENT:  
TRANSPORT AND LOSS

*Author(s):* HAJE KORTH, NIS-1

*Submitted to:* TECHNICAL UNIVERSITY OF BRAUNSCHWEIG,  
GERMANY

# Los Alamos

NATIONAL LABORATORY

Los Alamos National Laboratory, an affirmative action/equal opportunity employer, is operated by the University of California for the U.S. Department of Energy under contract W-7405-ENG-36. By acceptance of this article, the publisher recognizes that the U.S. Government retains a nonexclusive, royalty-free license to publish or reproduce the published form of this contribution, or to allow others to do so, for U.S. Government purposes. Los Alamos National Laboratory requests that the publisher identify this article as work performed under the auspices of the U.S. Department of Energy. Los Alamos National Laboratory strongly supports academic freedom and a researcher's right to publish; as an institution, however, the Laboratory does not endorse the viewpoint of a publication or guarantee its technical correctness.

**Comprehensive Study of the  
Geosynchronous Plasma Environment:  
Transport and Loss**

Der Gemeinsamen Naturwissenschaftlichen Fakultät  
der Technischen Universität Carolo-Wilhelmina  
zu Braunschweig  
zur Erlangung des Grades eines  
Doktors der Naturwissenschaften  
(Dr. rer. nat.)

genehmigte  
**Dissertation**

von Haje Korth  
aus Northeim

1. Referent: Prof. Dr. Karl-Heinz Glaßmeier  
2. Referent: Prof. Dr. Peter Weidelt  
eingereicht am: 9. August, 2001  
mündliche Prüfung (Disputation) am: 25. Oktober, 2001  
Druckjahr: 2001

To my family



# Vorveröffentlichungen

Teilergebnisse aus dieser Arbeit wurden mit Genehmigung der Gemeinsamen Naturwissenschaftlichen Fakultät, vertreten durch den Mentor der Arbeit, in folgenden Beiträgen vorab veröffentlicht:

## Publikationen

1. H. Korth, M. F. Thomsen, J. E. Borovsky und D. J. McComas,  
Plasma Sheet Access to Geosynchronous Orbit,  
**J. Geophys. Res.**, 104, 25047–25061, 1999.
2. H. Korth und M. F. Thomsen,  
Plasma Sheet Access to Geosynchronous Orbit:  
Generalization to Numerical Global Field Models,  
**J. Geophys. Res.**, im Druck, 2001.
3. H. Korth, M. F. Thomsen, K.-H. Glaßmeier und W. S. Phillips,  
Particle Tomography of the Inner Magnetosphere,  
**J. Geophys. Res.**, eingereicht, 2001.

## Tagungsbeiträge

1. H. Korth, M. F. Thomsen, J. E. Borovsky und D. J. McComas (Vortrag),  
Plasma Sheet Access to Geosynchronous Orbit,  
**AGU Spring Meeting 1999** in Boston, MA, USA.
2. H. Korth, M. F. Thomsen, J. E. Borovsky und D. J. McComas (Vortrag),  
Plasma Sheet Access to Geosynchronous Orbit:  
Generalization to Numerical Global Field Models,  
**IGPP Conference 1999** at Yellowstone National Park, WY, USA.
3. H. Korth, M. F. Thomsen, S. D. Lynch, E. E. Dors, R. C. Elphic,  
D. J. McComas, J. P. McFadden, C. W. Carlson und E. J. Lund (Vortrag),  
Causes and Consequences of a Cool, Dense Plasma Sheet Population  
in the Dawn Region During Intervals of High Geomagnetic Activity,  
**AGU Fall Meeting 1999** in San Francisco, CA, USA.

4. H. Korth, M. F. Thomsen, K.-H. Glaßmeier und W. S. Phillips (Vortrag),  
Tomography of the Inner Magnetosphere,  
**AGU Spring Meeting 2000** in Washington, DC, USA.
5. H. Korth, M. F. Thomsen, K.-H. Glaßmeier und W. S. Phillips (Poster),  
Tomography of the Inner Magnetosphere Using Numerical Field Models,  
**AGU Fall Meeting 2000** in San Francisco, CA, USA.

Los Alamos, den 13. Juli, 2001

Dipl. Phys. Haje Korth

Prof. Dr. Karl-Heinz Glaßmeier

# Contents

<b>1</b>	<b>Introduction</b>	<b>9</b>
1.1	The Earth's Magnetosphere . . . . .	9
1.1.1	Historical Overview . . . . .	9
1.1.2	Magnetospheric Regions . . . . .	10
1.1.3	Magnetospheric Currents . . . . .	13
1.2	Particle Motion in the Magnetosphere . . . . .	15
1.2.1	Single Particle Motion . . . . .	15
1.2.2	Magnetic and Electric Fields in the Magnetosphere . . . . .	19
1.2.3	Adiabatic Invariants . . . . .	23
1.2.4	Drift Trajectories and Alfvén Layers . . . . .	25
1.3	Geomagnetic Activity and its Indices . . . . .	26
1.4	Charged Particle Observations at Geosynchronous Orbit . . . . .	30
<b>2</b>	<b>Spacecraft and Plasma Instrumentation</b>	<b>33</b>
2.1	Overview . . . . .	33
2.2	Electrostatic Analyzers . . . . .	34
2.3	The MPA Instrument . . . . .	36
2.4	MPA Operation: Modes and Cycles . . . . .	37
2.5	Data Products . . . . .	39
2.5.1	Distribution Functions . . . . .	39
2.5.2	Velocity Moments . . . . .	40
2.5.3	Reported Products . . . . .	41
<b>3</b>	<b>Plasma Sheet Access to Geosynchronous Orbit</b>	<b>42</b>
3.1	Overview . . . . .	42
3.2	Introduction . . . . .	42
3.3	Particle Drift Description . . . . .	43
3.4	Statistical Data Analysis . . . . .	48
3.5	Observations . . . . .	52
3.5.1	Protons . . . . .	53
3.5.2	Electrons . . . . .	58
3.6	Discussion . . . . .	58



## Contents

---

3.6.1	Access . . . . .	58
3.6.2	Applications . . . . .	59
3.6.3	Comparison With ATS Measurements . . . . .	63
3.7	Summary . . . . .	64
<b>4</b>	<b>Generalization to Numerical Global Field Models</b>	<b>66</b>
4.1	Overview . . . . .	66
4.2	Introduction . . . . .	66
4.3	Models . . . . .	67
4.3.1	Alfvén Layer Model . . . . .	67
4.3.2	Field Models . . . . .	71
4.4	Model Comparison . . . . .	73
4.5	Discussion . . . . .	84
4.6	Summary . . . . .	87
<b>5</b>	<b>Particle Tomography of the Inner Magnetosphere</b>	<b>89</b>
5.1	Overview . . . . .	89
5.2	Introduction . . . . .	89
5.3	MPA Particle Flux Statistics . . . . .	91
5.4	Global Drift Pattern . . . . .	91
5.5	Charge Exchange Process . . . . .	93
5.6	Tomography Algorithm . . . . .	96
5.7	Application and Discussion . . . . .	103
5.8	Summary and Conclusions . . . . .	109
<b>6</b>	<b>Expansion of the Geosynchronous Studies</b>	<b>111</b>
6.1	Plasma Sheet Access to the Inner Magnetosphere . . . . .	111
6.2	Solar Cycle Dependence of the MPA Observations . . . . .	112
6.3	The Upper Cutoff Energy of the Electron Plasma Sheet as a Measure of Magnetospheric Convection Strength . . . . .	118
6.4	Interpretation of Observations of Magnetic Storms by the Alfvén Layer Paradigm . . . . .	119
<b>7</b>	<b>Summary and Outlook</b>	<b>120</b>
	<b>Bibliography</b>	<b>122</b>
	<b>Acknowledgements</b>	<b>134</b>
	<b>Lebenslauf</b>	<b>135</b>

# 1 Introduction

## 1.1 The Earth's Magnetosphere

### 1.1.1 Historical Overview

In 1600 William Gilbert, personal physician of Queen Elizabeth I, published his book *De Magnete* describing all that was then known about magnetism [Gilbert, 1958]. He also reports on his own experiments with a spherical magnet which he called *Terrella*, the “little Earth”. Using the *Terrella* he observed the same forces that were known to exist on Earth and concluded that the Earth is a magnet itself. The Earth's magnetic field Gilbert proposed is the foundation for the construction known today as the magnetosphere.

In 1839 Carl Friedrich Gauß published a method for mathematically describing the Earth's field  $\underline{B}$  by means of a scalar potential  $\gamma$

$$\underline{B} = -\nabla\gamma, \quad (1.1)$$

expanded at any point  $(r, \vartheta, \varphi)$  in spherical harmonics [Gauß, 1877; Kertz, 1992]:

$$\begin{aligned} \gamma = R_E \sum_{l=1}^{\infty} \left(\frac{R_E}{r}\right)^{l+1} \sum_{m=0}^l (g_l^{mi} \cos m\varphi + h_l^{mi} \sin m\varphi) P_l^m(\cos \vartheta) \\ + R_E \sum_{l=1}^{\infty} \left(\frac{r}{R_E}\right)^l \sum_{m=0}^l (g_l^{me} \cos m\varphi + h_l^{me} \sin m\varphi) P_l^m(\cos \vartheta). \end{aligned} \quad (1.2)$$

The first term in (1.2) represents sources inside the Earth and the second one external sources. Using data from a network of magnetic observatories, Gauß derived the coefficients  $g_l^{mi}$  and  $h_l^{mi}$  due to internal sources of the magnetic field. The calculations confirmed that approximately 99% of the field originates inside the Earth. The existence of the external contribution to the Earth's magnetic field was previously suggested by instrument builder George Graham in 1724 who discovered large irregular disturbances of the compass needle presently called *magnetic storms* [Graham, 1724; Chapman and Bartels, 1940, section 26.9]. But it was not until 1852 that a correlation between the frequency of magnetic storms and the sunspot activity was found by the British scientist Edward Sabine [Sabine, 1852]. The nature of the connection between physical phenomena that occur on the Sun and phenomena that occur in the near-Earth space environment was first revealed by the British

## 1 Introduction

---

astronomer Richard Carrington in 1859. Carrington observed an intense, short-lived brightening of the surface of the Sun in the vicinity of a sunspot [Carrington, 1860]. He noted that the event, known as a *solar flare*, was followed by a particularly large geomagnetic storm, suggesting a causal relationship between solar and geomagnetic events. More observations of such correlations soon followed, leaving no doubt that something was propagating from the Sun to the Earth, causing a magnetic disturbance upon its arrival.

At the turn of the 20th century the findings of the Norwegian Kristian Birkeland and his former mentor Henri Poincaré led to the understanding that flares emitted electron streams, which were steered by the Earth's field toward the auroral zones [Birkeland, 1901; Poincaré, 1896]. Since a stream of electrons carried an electric current, a magnetic disturbance would also be induced. However, negative charge accumulation on the Earth would disrupt the process as pointed out by Frederick Lindemann [Lindemann, 1919]. Lindemann suggested instead that any cloud or stream expelled from the Sun would have to be electrically neutral, containing equal charge from ions and electrons.

The problem of how a neutral beam could cause magnetic disturbances was addressed by Sidney Chapman and Vincent Ferraro in the early 1930s [Chapman and Ferraro, 1930, 1931, 1932]. They found that a current is induced on the front of a perfectly conducting plasma cloud approaching a dipole which corresponds to a magnetic field of an *image dipole* located at twice the distance of the cloud (see Figure 1.1a). By these means Chapman and Ferraro explained the rapid, steplike increase in the magnetic field leading the onset of many magnetic storms.

The Earth's magnetic field also exerts a force on the induced currents which becomes stronger with decreasing distance of the cloud from the Earth. Ultimately, Chapman and Ferraro argued, the force becomes strong enough to stop any further frontal advance of the cloud. However, the flanks that continue to advance form a cavity known as the *Chapman-Ferraro cavity* shown in Figure 1.1b. The flight of Mariner 2 to Venus in 1962 finally revealed the continuous nature of the *solar wind* [Snyder et al., 1963; Neugebauer and Snyder, 1966]. It then became clear that the Chapman-Ferraro cavity was not a temporary feature but exists at all times, and it received the name *magnetosphere*, coined by Gold [1959].

### 1.1.2 Magnetospheric Regions

Since its discovery by Chapman and Ferraro a much more detailed picture of the magnetosphere has evolved. Owing to enormous advances in the development of space-exploration technology it was possible to gather a large and varied database of physical quantities in the magnetosphere. Measurements of the electric and magnetic fields as well as particle distribution and composition data allow the identification of the distinct regions indicated in Figure 1.2.

Flowing at an average speed of 400 km/s, the supersonic solar wind encounters the dipolar magnetic field of the Earth as an obstacle which it cannot simply penetrate. In order to deflect the solar wind around the magnetosphere, a shock wave forms, much like that in

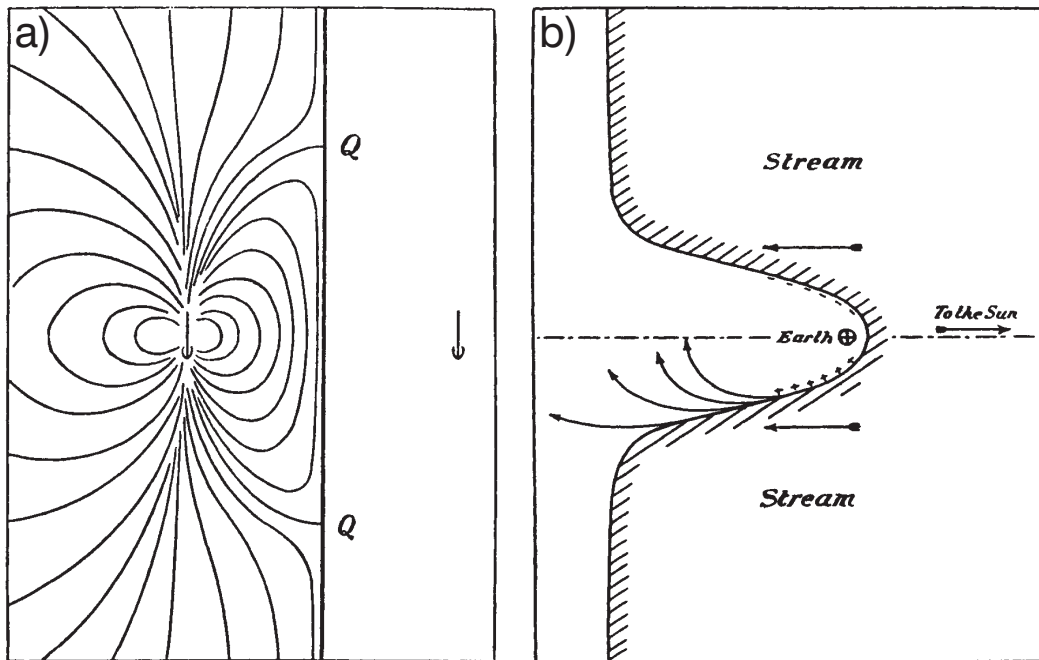


**Figure 1.1:** (a) The Earth’s dipole field, flattened by the addition of the field of an image dipole. (b) The formation of the Chapman-Ferraro cavity. Arrows trace the paths of ions and electrons which Chapman and Ferraro proposed to account for ring current effects (original sketches from *Chapman and Ferraro* [1931]).

front of a supersonic aircraft. This collisionless shock wave, referred to as the *bow shock*, slows the solar wind to subsonic speeds. It has the shape of a hyperboloid that is symmetric to the Sun-Earth line. The distance of the shock’s subsolar point from the center of the Earth is typically  $14 R_E$  (Earth radii,  $1 R_E \approx 6371$  km). The region of subsonic solar wind downstream of the bow shock is called the *magnetosheath*.

The shocked solar wind plasma of the magnetosheath cannot easily penetrate the terrestrial magnetic field. This is a consequence of the fact that the interplanetary magnetic field lines cannot penetrate the terrestrial magnetic field lines and that the solar wind particles cannot leave the interplanetary field lines due to the “frozen-in” characteristic of a highly conducting plasma. The boundary separating the two regions is called the *magnetopause*. Its distance from the center of the Earth (the stand-off distance) is typically  $10 R_E$ , given in a first order approximation by the pressure balance of the solar wind dynamic ram pressure and the magnetic pressure of the terrestrial field. The thickness of the magnetopause under idealized conditions is of the order of a few hundred kilometers, corresponding to a penetration depth of the solar wind particles into the magnetospheric field of about one ion gyroradius [*Baumjohann and Treumann*, 1997, p. 191].

The magnetosphere shields the Earth from incident solar wind particles very effectively

# 1 Introduction

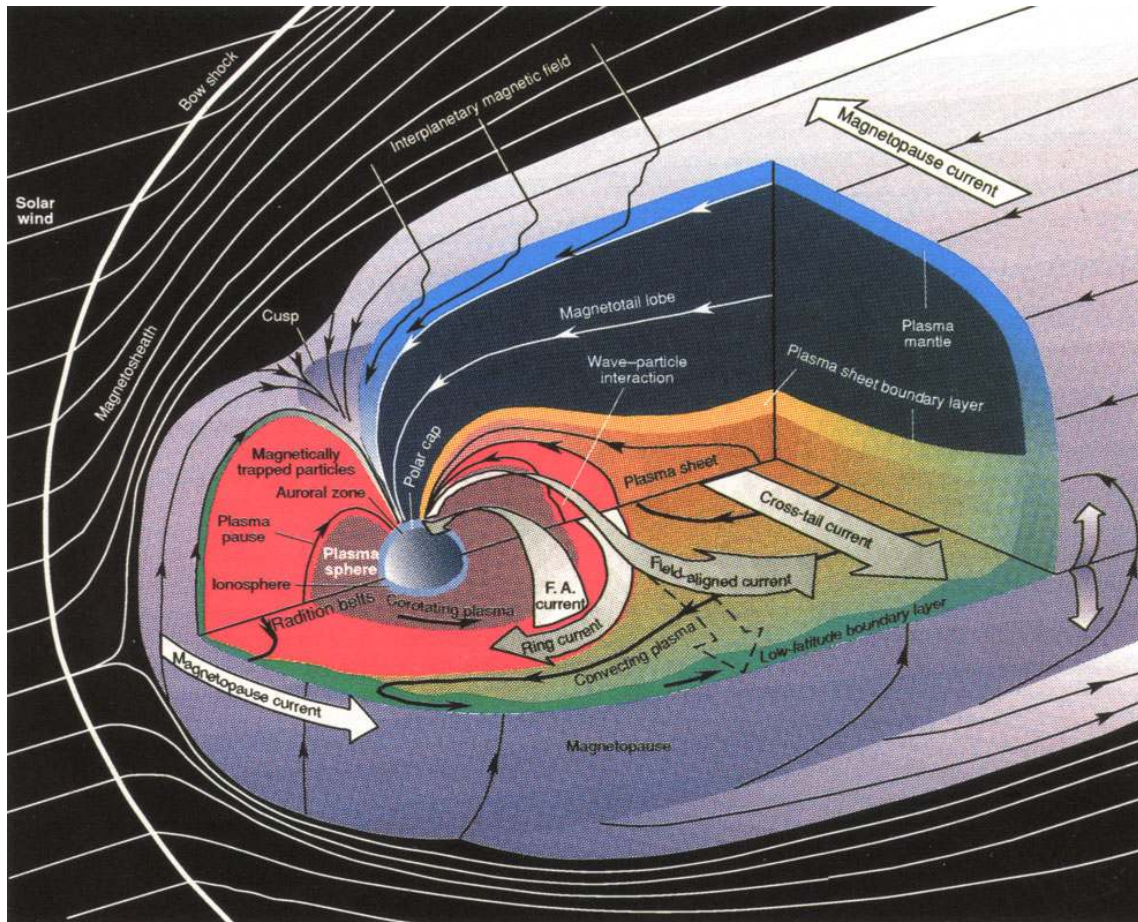


**Figure 1.2:** Three-dimensional view of the Earth's magnetosphere (from Mitchell [1990]).

at lower latitudes. However, at high latitudes the magnetic field lines converge toward the poles, forming two funnel-shaped regions termed the *polar cusps*. Through the cusp regions solar wind plasma can directly advance toward the Earth to lower altitudes and into the magnetosphere.

Located earthward of the magnetopause are the *magnetospheric boundary layers*, which are usually several thousand kilometers thick. A boundary layer is a transition region separating two plasma populations with distinct characteristics. The regions satisfying this criterion are the entry layer (high-altitude cusp), the plasma mantle, the low-latitude boundary layer, and the plasma sheet boundary layer. The entry layer is formed by direct entry of the magnetosheath plasma along open field lines that form the magnetospheric cusp. The plasma mantle is also located on open field lines and separates the tail lobes from the magnetosheath. Its composition consists of a mixture of magnetosheath plasma that entered the magnetosphere through the cusp and ionospheric plasma. The low-latitude boundary layer (LLBL) is found over most of the dayside magnetopause and represents the boundary

## 1 Introduction

---

between the plasma sheet and the magnetosheath. It is presently unknown how much of the LLBL is on open or on closed field lines. Due to the vague understanding of the internal structure of the LLBL, the origin and entry processes of the plasma forming this region are uncertain. Magnetosheathlike as well as magnetospheric populations have been observed here. While the plasma of the entry layer is relatively stagnant, the plasmas of the mantle and the low-latitude boundary layer are characterized by a tailward flow. The boundary between the tail lobes and the plasma sheet is called the plasma sheet boundary layer and is probably located on closed field lines. Its source are particles of other boundary layers such as the plasma mantle and the LLBL that enter this region through a reconnection process.

Most of the magnetotail plasma is concentrated in closed flux tubes around the tail mid-plane in an approximately  $10 R_E$  thick *plasma sheet*. Near the Earth, it reaches down along the field lines into the high-latitude auroral ionosphere. The plasma mantle is believed to be an important source of the plasma sheet [Pilipp and Morfill, 1978]. Reconnection in the distant tail converts antisunward-streaming mantle plasma into beams that stream toward the Earth along field lines. The beams mirror in the region of strong magnetic field near the Earth, creating antisunward streams (see section 1.2.3 for an explanation of the mirror process). The counterstreams tend to be unstable to various plasma waves, which eventually convert the streaming energy to thermal energy, creating the hot, slow-flowing plasma sheet.

The outer parts of the magnetotail directly adjacent to the plasma sheet are called the *magnetotail lobes*. In the lobes, cool ions are often observed flowing away from the Earth, and their composition often suggests an ionospheric origin. The plasma in this region is normally located on open field lines.

Particles on magnetic field lines earthward of the plasma sheet are magnetically trapped. Under stationary magnetospheric conditions, these populations drift around the Earth continuously since they cannot escape from the dipolar magnetic field. Examples for trapped populations are the high-energy *van Allen radiation belt* particles [Van Allen *et al.*, 1958; Van Allen and Frank, 1959] and the dense, cold plasma of the *plasmasphere*.

### 1.1.3 Magnetospheric Currents

The plasmas discussed in section 1.1.2 are usually not stationary but move under the influence of external forces. Sometimes ions and electrons move together, like in the solar wind. But in other plasma regions ions and electrons move in different directions, creating an electric current. These currents and their corresponding electric fields are essential for magnetospheric plasma dynamics. The most significant currents are shown in Figure 1.2 and shall be discussed here.

As noted in section 1.1.1, the compression of the terrestrial magnetic field by the solar wind on the dayside is associated with a current flow across the magnetopause surface. The origin of this *magnetopause current*, also referred to as Chapman-Ferraro current, can be understood from Figure 1.3. When solar wind protons and electrons penetrate the magnetopause boundary, they sense a Lorentz force, which causes them to gyrate. After half an orbit they exit the magnetopause, moving antiparallel to the solar-wind flow. The sense

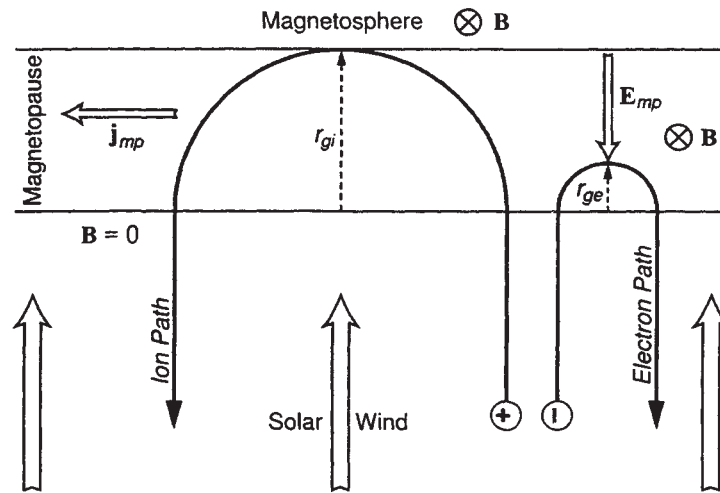


**Figure 1.3:** Specular reflection off the magnetopause (after *Baumjohann and Treumann* [1997]).

of gyration inside the boundary is opposite for the two kinds of particles, leading to the generation of a narrow surface current layer. An additional electric field  $\underline{E}_{mp}$  arises due to protons that penetrate the boundary deeper than electrons. Such an electric field tends to drag the electrons in farther while pushing back the protons. In the equatorial plane the magnetopause current flows from dawn to dusk. It closes on the tail magnetopause where it splits into a northern and a southern current loop.

The tail magnetopause current is additionally fed by the *cross-tail neutral sheet current* which was explained by *Alfvén* [1968] using the model illustrated in Figure 1.4. The model assumes a potential drop between the dawn- and duskside magnetopause. Owing to the presence of the Earth's magnetic field, the electric field resulting from this potential drop induces a particle drift  $\underline{u}$  to the neutral sheet from the north and the south. In absence of the magnetic field in the central plane, the protons and electrons are accelerated in the electric field toward the dusk- and dawnside magnetopause, respectively. This latter motion provides the cross-tail current.

Another large-scale current system, which influences the configuration of the inner magnetosphere, is the *ring current*. The ring current flows around the Earth in the westward direction at radial distances of several Earth radii. It is carried by the radiation belt particles mentioned in section 1.1.2. Since the protons drift westward while the electrons move in eastward direction, a net charge transport results.

Not shown in Figure 1.2 are the currents flowing in the Earth's ionosphere, at altitudes of 100–150 km. The most prominent ones are the *auroral electrojets* inside the auroral oval, the *Sq currents* in the dayside mid-latitude ionosphere, and the *equatorial electrojet* near the magnetic equator.

In addition to the field-perpendicular currents above, currents known as *field-aligned*

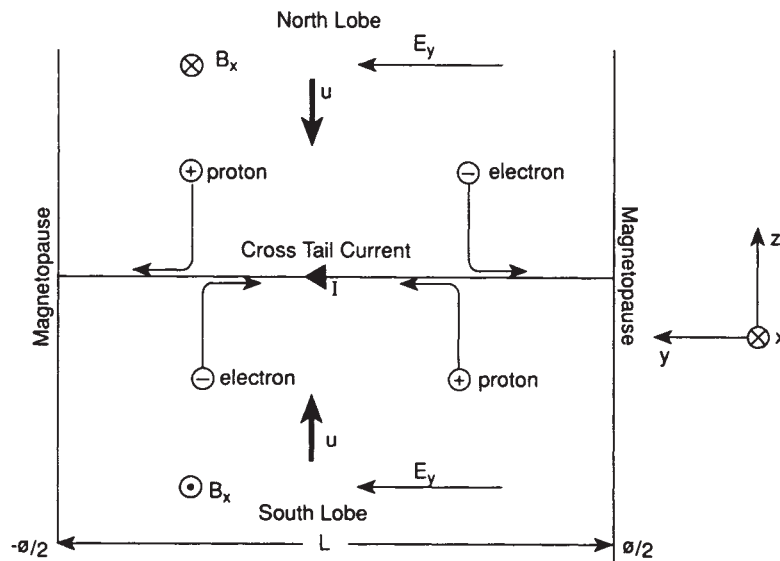


**Figure 1.4:** Cut through the magnetotail looking toward the Sun. The particles drift into the tail current sheet from either lobe. After entering the current sheet, protons and electrons travel to the dusk and dawn magnetopause, respectively, carrying the cross-tail current (from Hughes [1995]).

currents flow along the magnetic field lines. Carried mainly by electrons, the field-aligned currents connect magnetospheric current systems in the magnetosphere to those flowing in the polar ionosphere. They are subdivided into two categories [Iijima and Potemra, 1976a,b]: Region-1 and Region-2 currents (see Figure 1.5). Region-1 currents are located in the poleward half of the auroral oval and flow along the high-latitude boundary of the plasma sheet before they merge with the neutral sheet current deep down in the magnetotail. The Region-2 currents flow in the equatorward half of the auroral oval and are closed by the westward ring current in the near-Earth equatorial plane.

## 1.2 Particle Motion in the Magnetosphere

### 1.2.1 Single Particle Motion

A plasma is an electrically neutral gas composed predominantly of charged particles. Therefore its motion is largely determined by electrical and magnetic forces. If an electric field  $\underline{E}$  and a magnetic field  $\underline{B}$  act on a particle with charge  $q$  and the velocity  $\underline{v}$ , the particle experiences the Lorentz force:

$$\underline{F}_L = q (\underline{E} + \underline{v} \times \underline{B}). \quad (1.3)$$



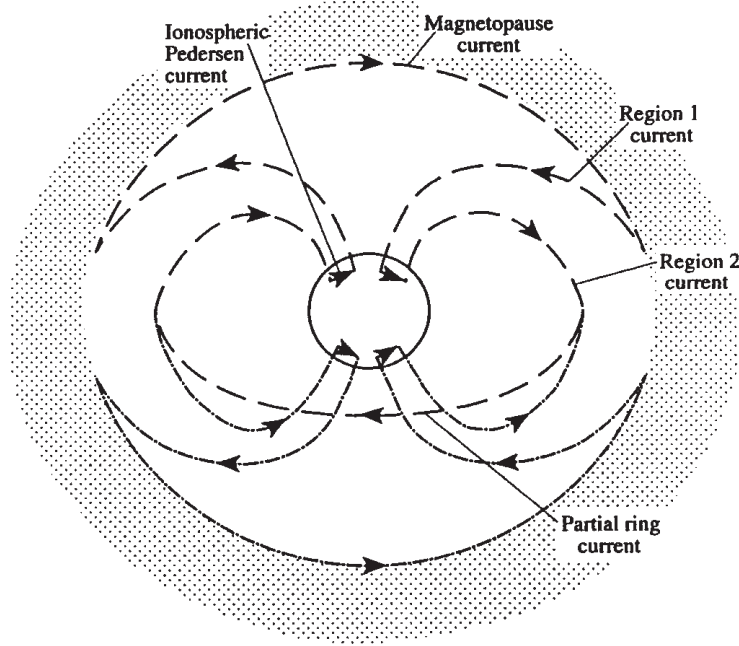


**Figure 1.5:** Sketch of the overall auroral zone current circuit looking at the Earth from the tail, showing both the northern (dashed lines) and the southern (dash-dotted lines) branches of the circuit (from Cowley [2000]).

According to Newton's laws, its equation of motion is then given by

$$m \frac{d\mathbf{v}}{dt} = q (\mathbf{E} + \mathbf{v} \times \mathbf{B}) + \mathbf{F}_g, \quad (1.4)$$

where  $\mathbf{F}_g$  represents nonelectromagnetic forces such as gravitational forces that may be present. In the terrestrial magnetosphere these nonelectromagnetic forces are negligible and are thus omitted from consideration throughout this thesis.

In the absence of an electric field a charged particle in a uniform magnetic field gyrates in circular orbits around the magnetic field lines as can be seen from the following example. Assuming the magnetic field  $\mathbf{B}$  is oriented in the  $z$  direction of a Cartesian coordinate system, the components of (1.4) can be written as

$$\begin{aligned} m \dot{v}_x &= qB v_y, \\ m \dot{v}_y &= -qB v_x, \\ m \dot{v}_z &= 0. \end{aligned} \quad (1.5)$$

Taking the second derivative of (1.5) one obtains

$$\begin{aligned} \ddot{v}_x &= -\omega_g^2 v_x, \\ \ddot{v}_y &= -\omega_g^2 v_y, \end{aligned} \quad (1.6)$$

# 1 Introduction

---

where  $\omega_g = qB/m$  is called the *gyrofrequency*. The solution of the harmonic oscillator (1.6) has the form

$$\begin{aligned} x - x_0 &= r_g \sin \omega_g t, \\ y - y_0 &= r_g \cos \omega_g t, \end{aligned} \tag{1.7}$$

and describes the circular motion of the particle around a guiding center as shown in Figure 1.6. In (1.7)  $r_g = \sqrt{v_x^2 + v_y^2}/|\omega_g|$  is referred to as the *gyroradius*.

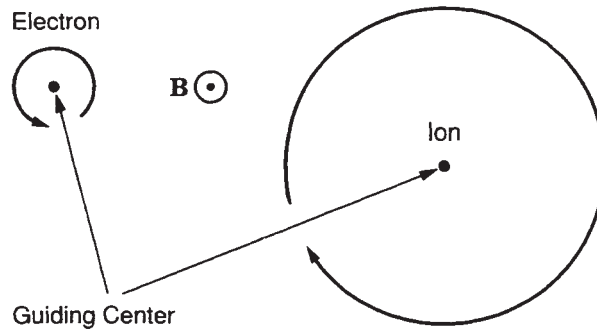


**Figure 1.6:** Gyration of charged particles around a guiding center (from *Baumjohann and Treumann [1997]*).

Taking an electric field  $\underline{E}$  into consideration will modify the gyratory motion. The component of  $\underline{E}$  parallel to the magnetic field is usually canceled out by electrons that are under most circumstances extremely mobile along the magnetic field lines. On the other hand, a perpendicular component of  $\underline{E}$  accelerates the particle during part of the orbit and decelerates it during the remaining part of the orbit. Associated with the acceleration and deceleration is a modulation of the gyroradius, causing the particle to drift in a direction perpendicular to  $\underline{E}$  and  $\underline{B}$  as illustrated in Figure 1.7. The drift of the guiding center is

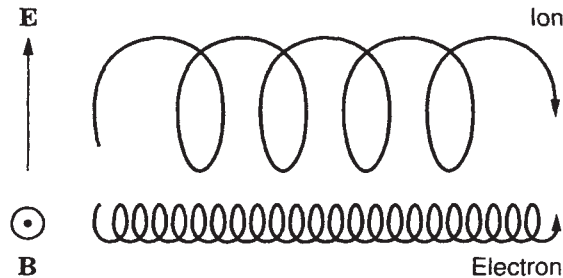


**Figure 1.7:** Particle motion in a uniform magnetic field  $\underline{B}$  in the presence of an electric field  $\underline{E}$  perpendicular to  $\underline{B}$  (from *Baumjohann and Treumann [1997]*).

# 1 Introduction

---

termed  $E \times B$  drift and has the general form

$$v_E = \frac{\underline{E} \times \underline{B}}{B^2}. \quad (1.8)$$

The  $E \times B$  drift velocity is independent of the energy and charge of the particle. Consequently, electrons and ions move in the same direction. Equation (1.8) can be generalized to describe drifts of an arbitrary force  $\underline{F}$  that is capable of accelerating and decelerating particles as they gyrate:

$$v_F = \frac{\underline{F} \times \underline{B}}{qB^2}. \quad (1.9)$$

In addition to the electric drift described above, magnetic drifts are induced if the underlying magnetic field is inhomogeneous. If a gyrating particle senses a gradient in the magnetic field strength from one side of its gyration orbit to the other, the instantaneous radius of curvature of the orbit becomes alternately smaller and larger as depicted in Figure 1.8. As a result the particle will drift in direction perpendicular to  $\underline{B}$  and  $\nabla B$ . Integrating

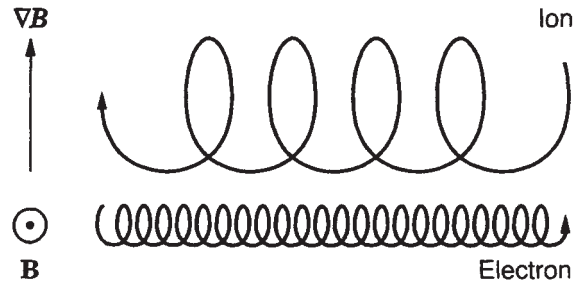


**Figure 1.8:** Particle drift due to a magnetic field gradient (from *Baumjohann and Treumann* [1997]).

over the gyroperiod, the *gradient drift* velocity of the guiding center is found to be [e.g., *Kivelson*, 1995]

$$v_{\nabla} = \frac{mv_{\perp}^2}{2qB^3} (\underline{B} \times \nabla B). \quad (1.10)$$

The gradient drift is proportional to the kinetic energy perpendicular to the magnetic field. Its direction is given by the sign of the particle charge and is therefore opposite for electrons and ions.

An additional drift component is introduced by the curvature of the magnetic field lines. Particles moving along the field direction with the velocity  $v_{\parallel}$  experience the centrifugal force

$$\underline{F}_R = mv_{\parallel}^2 \frac{\underline{R}_c}{R_c^2}, \quad (1.11)$$

## 1 Introduction

---

where  $R_c$  is the local radius of curvature. The resulting *curvature drift* velocity is obtained by inserting (1.11) in the general force drift equation (1.9):

$$\underline{v}_R = \frac{mv_{\parallel}^2}{q} \frac{R_c \times \underline{B}}{R_c^2 B^2}. \quad (1.12)$$

The curvature drift depends on the kinetic energy parallel to the magnetic field, and its direction is determined by the charge of the particle. Adding the electric and magnetic drift components described above, the overall guiding center drift velocity of a particle yields

$$\underline{v}_D = \underline{v}_E + \underline{v}_V + \underline{v}_R = \frac{\underline{E} \times \underline{B}}{B^2} + \frac{mv_{\perp}^2}{2qB^3} (\underline{B} \times \nabla B) + \frac{mv_{\parallel}^2}{q} \frac{R_c \times \underline{B}}{R_c^2 B^2}. \quad (1.13)$$

The large-scale electric and magnetic fields that dominate the plasma motion represented by (1.13) are explained in the next section.

### 1.2.2 Magnetic and Electric Fields in the Magnetosphere

The magnetic field surrounding the Earth is made up of both internal and external sources. The former is generated by a dynamo process in the liquid outer core of the Earth's interior. Its multipole characteristic is evident from the requirement of higher-order spherical harmonics in the Gauß representation of the magnetic potential (1.2), which are essential to adequately describe the terrestrial field. However, near the surface of the Earth the dipolar approximation is often sufficiently accurate:

$$B(r, \lambda) = \frac{B_E R_E^3}{r^3} \frac{\sqrt{1 + 3 \sin^2 \lambda}}{\cos^6 \lambda}, \quad (1.14)$$

where  $\lambda$  is the magnetic latitude,  $r$  is the equatorial distance of the field line from the center of the Earth, and  $B_E$  is the equatorial magnetic field strength at the Earth's surface. At larger distances from the Earth the dipole field becomes distorted by the external field contributions induced by the magnetospheric and ionospheric currents discussed in section 1.1.3.

The large-scale electric fields in the inner magnetosphere are the convection and corotation electric fields. The former is associated with a global plasma circulation pattern that is driven by interaction of the solar wind with the magnetosphere as illustrated in Figure 1.9. If the interplanetary magnetic field (IMF) is directed southward, its field lines merge with the closed field lines of the terrestrial dipole field at the dayside magnetopause (field lines denoted 1). Subsequently the solar wind transports the merged field lines (which are frozen into the plasma flow according to the hydromagnetic theorem) down-tail across the polar cap (field lines marked 2–6). Deep in the magnetotail the two open field lines reconnect again (field line 7), leaving a closed but stretched field line. Releasing magnetic tension the closed field line relaxes earthward, transporting plasma that is tied to the field lines toward

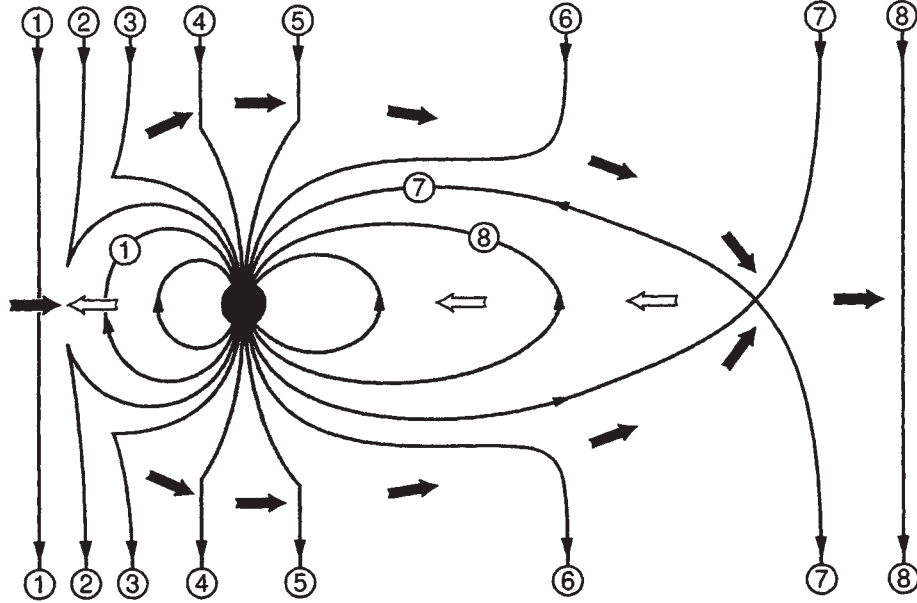


**Figure 1.9:** Field line merging and reconnection at the magnetopause (after *Baumjohann and Treumann [1997]*).

the Earth. The sunward motion of plasma in the inner magnetosphere is is, for an observer on the Earth, equivalent to an electric convection field

$$\underline{E}_c = -\underline{v}_c \times \underline{B}, \quad (1.15)$$

where  $\underline{v}_c$  is the convection speed. For nearly time-stationary conditions the electric field due to convective particle motion is approximately curl-free and can thus be represented by the gradient of a potential function

$$\underline{E}_c = -\nabla U_c. \quad (1.16)$$

In polar coordinates, the potential of a uniform convection electric field in the equatorial plane is given by

$$U_c = -E_0 r \sin \varphi, \quad (1.17)$$

where  $E_0$  is the uniform convection electric field strength in the equatorial plane,  $r$  is the radial distance from the center of the Earth, and  $\varphi$  is the magnetic local time referred to noon (see Figure 1.10). In the inner magnetosphere the convection electric potential is somewhat weaker than described by (1.17). Different drift paths of electrons and protons lead to a charge separation that is associated with a polarization electric field. This electric field is directed from dusk to dawn and shields the inner region from the oppositely directed cross-tail electric field. Taking this *shielding effect* into account leads to a more realistic convection potential

$$U_{cs} = -E_0 r^\gamma \sin \varphi. \quad (1.18)$$

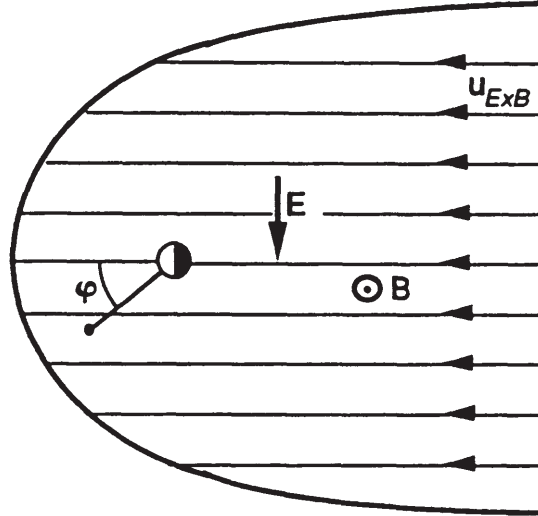


**Figure 1.10:** The coordinate angle  $\varphi$  of the convection potential is zero at local noon,  $\pi/2$  at dusk,  $\pi$  at local midnight, and  $3\pi/2$  at dawn (from Wolf [1995]).

The shielding factor  $\gamma$  was proposed by Volland [1973] and Stern [1975] and has been estimated by these authors to be  $\sim 2$ . This result was confirmed by various authors [e.g., Maynard and Chen, 1975; Ejiri, 1978; Ejiri *et al.*, 1978; Southwood and Kaye, 1979; Elphic *et al.*, 1999]. The total potential difference between the dawn and dusk magnetopause is related to the solar wind electric field and the dayside reconnection rate and usually takes magnitudes between 50–100 kV [Baumjohann and Treumann, 1997, p. 81].

Historically, Volland [1973] derived the shielding factor from the simplified ionospheric electric potential distribution illustrated in Figure 1.11, which assumes the polar cap to be circular with a constant electric field inside. The ionospheric currents and the ionospheric electric fields then form the pattern of electric equipotentials resembling Figure 1.11. Introducing plane polar coordinates  $(\rho, \varphi)$  and denoting the radius of the boundary circle with  $\rho_0$ , a simple analytical model resulting in such potential configuration is

$$U = -U_0 \left( \frac{\rho}{\rho_0} \right) \sin \varphi \quad \rho < \rho_0, \quad (1.19a)$$

$$U = -U_0 \left( \frac{\rho_0}{\rho} \right)^k \sin \varphi \quad \rho > \rho_0, \quad (1.19b)$$

where  $U_0$  equals half of the potential drop across the circle  $\rho = \rho_0$ , and the exponent  $k$  is an adjustable parameter. The larger  $k$  is, the tighter the fringing pattern of equipotentials at  $\rho > \rho_0$  is pressed against the circle. If  $\rho$  is measured from the pole along the surface of the Earth,

$$\rho = R_E \vartheta, \quad (1.20)$$

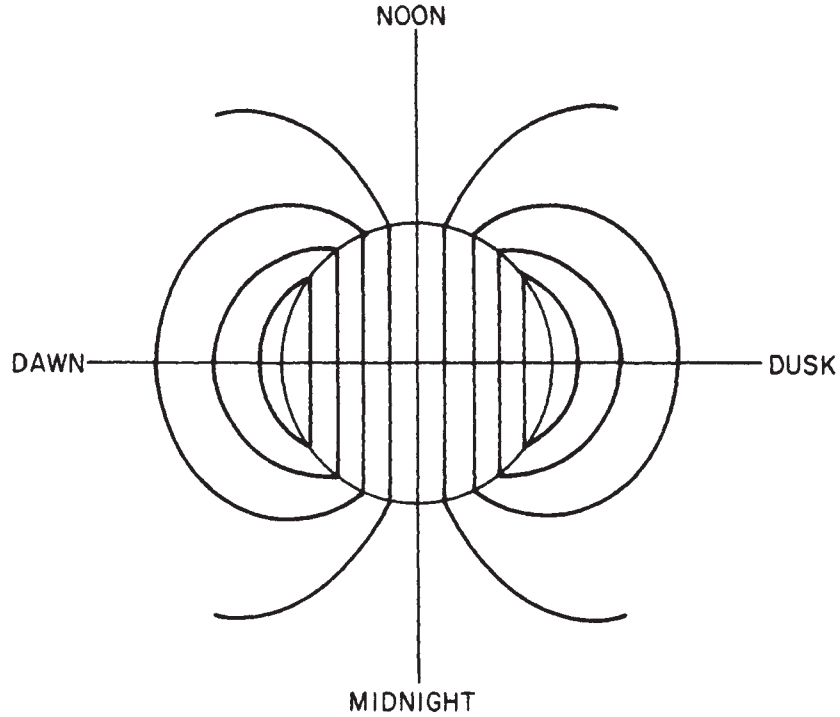


**Figure 1.11:** Schematic view of electric equipotentials in the polar caps (from *Stern* [1977]).

where  $\vartheta$  is the colatitude. In the approximation for small angles ( $\sin \vartheta \approx \vartheta$ ) and under consideration of (1.20), the dipole mapping of the potential pattern (1.19b) to the magnetic equatorial plane gives

$$U_{\text{eq}} = -U_0 \left( \frac{r}{r_0} \right)^{\frac{k}{2}} \sin \varphi \quad r < r_0, \quad (1.21)$$

where  $r$  is the radial distance in the equatorial plane, and  $r_0$  is a normalizing factor. The exponent  $k/2$  in (1.21) affects the electric potential pattern in a similar way as does a polarization electric field, which shields the inner magnetosphere from the convection electric field, and was therefore termed the shielding factor  $\gamma = k/2$ . The *Volland* [1975] choice of the shielding factor  $\gamma = 2$  is based upon observations of the  $S_q^p$  current system [*Nishida*, 1968; *Obayashi and Nishida*, 1968], the *Svalgaard effect* [*Svalgaard*, 1973], and the plasmopause configuration [*Chappell*, 1972; *Carpenter and Park*, 1973].

The corotation electric field is caused by the rotation of the Earth, whose corotating upper atmosphere forces the ionospheric plasma into corotation via ion and electron-neutral collisions. For a nonrotating observer this plasma motion represents an electric field

$$\underline{E}_{\text{cr}} = -(\underline{\Omega}_{\text{E}} \times \underline{r}) \times \underline{B}, \quad (1.22)$$

where  $\underline{\Omega}_{\text{E}}$  is the angular velocity of the Earth's rotation. Using (1.14) to express the mag-

## 1 Introduction

---

netic field, the corotation electric field in the equatorial plane in cylindrical coordinates is

$$\underline{E}_{\text{cr}} = \left( -\frac{\Omega_{\text{E}} B_{\text{E}} R_{\text{E}}^3}{r^2}, 0, 0 \right). \quad (1.23)$$

The potential of the corotation electric field is calculated by integration of (1.23) and found to be

$$U_{\text{cr}} = -\frac{a}{r}, \quad (1.24)$$

where the corotation constant  $a = \Omega_{\text{E}} B_{\text{E}} R_{\text{E}}^3$  amounts to approximately  $92.4 \text{ kV } R_{\text{E}}$ . The sum of the potentials of the convection and corotation electric fields, given by (1.18) and (1.24), respectively, is referred to as the Volland-Stern electric potential [Volland, 1973, 1975, 1978; Stern, 1975]:

$$U_{\text{vs}} = -\frac{a}{r} - E_0 r^\gamma \sin \varphi. \quad (1.25)$$

Since a pair of models for the electric and magnetic fields used in conjunction with the drift velocity equation (1.13) is sufficient for the description of particle drifts in the magnetosphere, such a model combination is referred to as a *convection model* in this thesis. Even though suitable under numerous conditions, the dipolar magnetic field and the Volland-Stern electric potential represent a highly simplified convection model. More sophisticated analytical, semiempirical, and empirical field models that may at times be more realistic exist in the literature and will be introduced as needed at a later time.

### 1.2.3 Adiabatic Invariants

In a dipolar magnetic field three fundamental types of quasi-periodic motions that correspond to different timescales are distinguished [e.g., Roederer, 1970]: As illustrated in Figure 1.12 particles gyrate around the field lines, bounce along the field lines between the mirror points, and execute the drift motion described by (1.13) that is directed eastward for the electrons and primarily westward for the ions. Each of these types of motion is associated with an *adiabatic invariant* that remains nearly constant if the timescale of the field changes is long compared to the periodicity of the particle motion.

The first adiabatic invariant is the magnetic moment  $\mu$  and is related to gyration:

$$\mu = \frac{m v_{\perp}^2}{2B}, \quad (1.26)$$

where  $m$  is the particle mass,  $B$  is the magnetic field strength, and  $v_{\perp}$  is the particle velocity perpendicular to the magnetic field. In order to conserve the magnetic moment, the magnitude of the perpendicular velocity increases as the particle moves poleward along the field line into regions of higher magnetic field strength. Simultaneously the magnitude of the velocity parallel to the magnetic field decreases since the total kinetic energy of the particle has to be conserved if no electric field exists parallel to  $\underline{B}$  [Wolf, 1995]:

$$W_{\text{kin}} = \frac{1}{2} m \left( v_{\parallel}^2 + v_{\perp}^2 \right) = \frac{1}{2} m v_{\parallel}^2 + \mu B = \text{constant}. \quad (1.27)$$



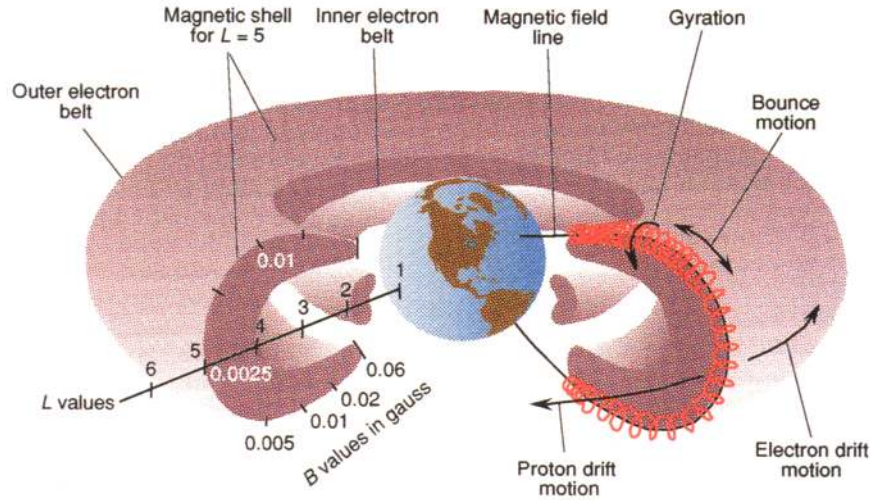


**Figure 1.12:** Trajectories of particles trapped on closed field lines (from *Mitchell* [1990]).

At the *mirror point* the parallel velocity changes its sign, and the particle proceeds toward the opposite hemisphere where the mirror-process is repeated. Since  $v_{\parallel}$  vanishes at the mirror locations, it follows for the kinetic energy from (1.27) that

$$W_{\text{kin}} = \mu B_m, \quad (1.28)$$

where  $B_m$  denotes the magnetic field strength at the mirror point.

Associated with the bounce motion of the guiding center is the second adiabatic invariant which is defined by

$$J = \oint m v_{\parallel} ds, \quad (1.29)$$

where  $v_{\parallel}$  is the parallel particle velocity,  $ds$  is an element of the guiding center path, and the integral is taken over a full oscillation between the mirror points. The parameter  $J$  is conserved if the magnetic field changes occur on timescales that are long compared to the bounce period.

The particle velocity parallel to the magnetic field is obtained from (1.27) as

$$v_{\parallel} = \sqrt{\frac{2}{m}} \sqrt{W_{\text{kin}} - \mu B}. \quad (1.30)$$

Under consideration of (1.28) and (1.30) the second adiabatic invariant then yields

$$J = 2\sqrt{2m\mu} \int_{m_1}^{m_2} \sqrt{B_m - B(s)} ds, \quad (1.31)$$

## 1 Introduction

---

where  $m_1$  and  $m_2$  are the locations of the mirror point. For the applications in this thesis it is convenient to introduce the *modified second adiabatic invariant* [Roederer, 1970, p. 51]

$$K = \frac{J}{2\sqrt{2m\mu}} = \int_{m_1}^{m_2} \sqrt{B_m - B(s)} ds, \quad (1.32)$$

which is a purely field-geometric quantity and as such independent of the particle's mass and energy.

The third adiabatic invariant refers to the drift motion of a particle. As a particle bounces and drifts in a magnetic field that varies slowly along its orbit, it traces out a three-dimensional *drift shell*. The magnetic flux enclosed by the drift shell of a particle

$$\Phi = \iint \underline{B} d\underline{S} \quad (1.33)$$

is defined as its third adiabatic invariant. It is conserved if drift periods are short compared to the timescale of the magnetic field variations.

If the timescale of magnetic field changes becomes comparable to the gyro, bounce, or drift periods, which are of the order of seconds, minutes, and hours, respectively, the invariants are violated. Since the drift motion exhibits the longest periods, it is the third adiabatic invariant that is infringed most often. Violations of the invariants also occur if the spatial scale of magnetic field variations is of the order of the gyroradius.

### 1.2.4 Drift Trajectories and Alfvén Layers

The drifts of particles through the magnetosphere can be calculated from the drift velocity equation (1.13) utilizing adequate models for the electric and magnetic fields such as the Volland-Stern and dipole models described in section 1.2.2. As discussed by many authors, drift trajectories are subdivided into two categories [e.g., Roederer, 1970], which will be discussed separately below for low-energy (cold) and higher-energy (warm/hot) particles.

For low-energy ions and electrons, the gradient and curvature drifts in (1.13) are negligible, and only the  $E \times B$  drift-term is of relevance. Near the Earth, the electric field is dominated by the corotation potential (first term of (1.25)) and points radially inward toward the center of the Earth. Therefore, the  $E \times B$  drift is directed eastward at all local times, forming a class of closed drift trajectories. The corotation potential decreases with increasing distance from the Earth. Far out in the magnetosphere the convection potential dominates, resulting in sunward flow of the particles on open drift trajectories. In the intermediate region convection and corotation are superposed. For zero-energy particles, the boundary between the regions of open and closed drift paths coincides with the last closed (last open) equipotential of the electric field and is termed the *plasma pause* (see Figure 1.13). It separates the plasmasphere from the inner edge of the plasma sheet.

For higher-energy particles, the gradient and curvature drifts become important and outweigh corotation in the near-Earth region. The particles drift on closed trajectories in

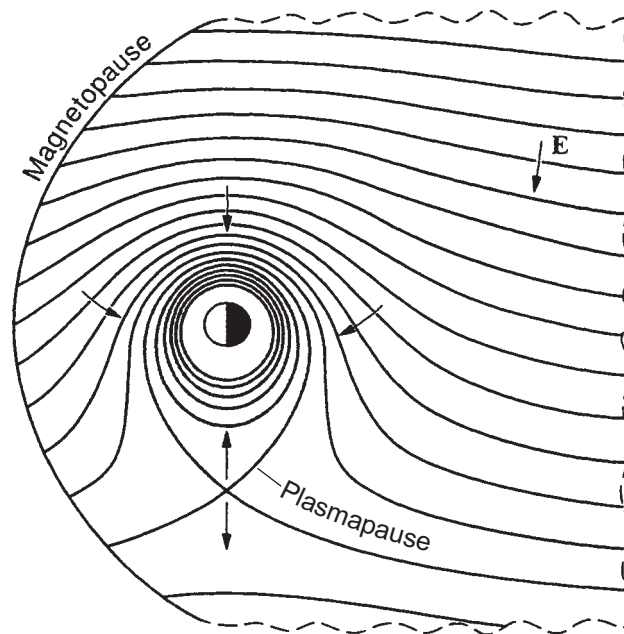


**Figure 1.13:** Electric equipotential contours in the equatorial plane (after *Baumjohann and Treumann [1997]*).

the vicinity of the Earth. However, due to the charge dependence of gradient and curvature drifts, electrons and ions drift in opposite directions, namely eastward and westward, respectively. With increasing distance from the Earth, the magnetic field strength drops rapidly causing gradient and curvature drifts to weaken until eventually the convective drift dominates and the drift paths become open. For nonzero-energy particles, the boundaries between regions of open and closed drift paths are referred to as *Alfvén layers* [e.g., *Alfvén and Fälthammar, 1963; Schield et al., 1969*]. The concept of the Alfvén layers is an important element of this thesis and will be discussed extensively later on. The various drifts mentioned above are summarized in Figure 1.14.

### 1.3 Geomagnetic Activity and its Indices

Magnetospheric convection is a rather dynamic process controlled by density, flow velocity, temperature, and pressure of the solar wind as well as the interplanetary magnetic field strength and direction. The flow velocity of the solar wind and the magnitude of the southward component of the interplanetary field determine the amount of magnetic flux merged per unit time, referred to as the *reconnection rate*, which is rather variable. Moreover, for considerable periods of time the interplanetary field is directed northward, greatly reducing the dayside merging. Thus there are intervals when the magnetosphere is very quiet as well

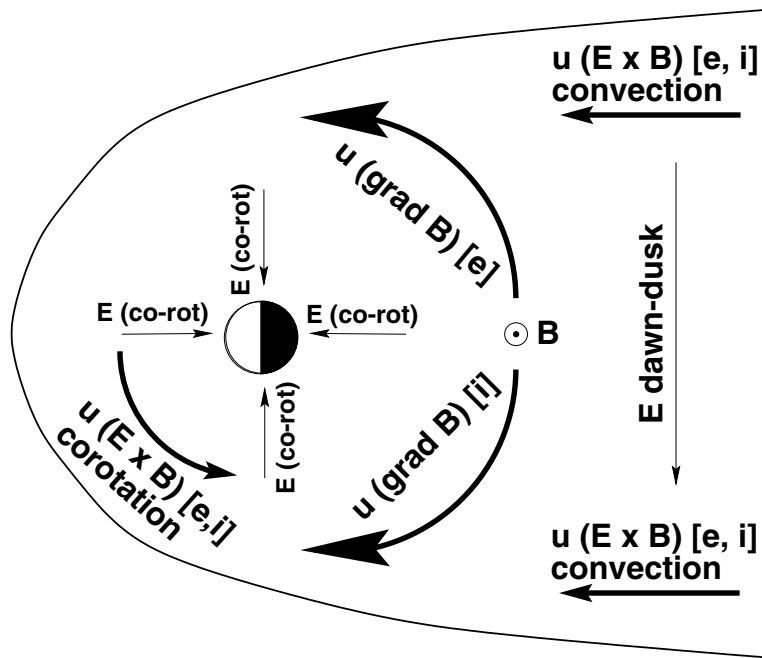


**Figure 1.14:** Components of particle drift  $\underline{u}$  in the equatorial magnetosphere (from *Friedel et al.* [2001]).

as other periods where large amounts of flux are merged on the dayside, resulting in an active magnetosphere.

The *geomagnetic activity* of the magnetosphere is described by a variety of *geomagnetic indices* that are derived from ground-based magnetometer data to ensure continuous coverage. Of over 30 such indices, the  $Kp$ ,  $Dst$ , and  $AE$  indices are most commonly used. A brief description of these indices is given below. For a more detailed discussion of geomagnetic indices and their derivation see *Mayaud* [1980]. In this thesis only the  $Kp$  index is used extensively. An explanation of  $Dst$  and  $AE$  is included to emphasize the distinct characteristics of geomagnetic indices.

The  $Kp$  index, defined by *Bartels* [1949], represents a measure of the worldwide average level of activity. It is based on disturbances of the magnetic field measured at thirteen subauroral stations located at absolute geomagnetic latitudes between  $43^\circ$  and  $62^\circ$ , selected for good longitudinal coverage. The stations and their locations are listed in Table 1.1. The global  $Kp$  index is derived from the  $K$  indices that are locally determined at each station by the following procedure. (The  $K$  index is not to be confused with the modified second adiabatic invariant defined in section 1.2.3.) First, the time series of the two horizontal magnetic field components are corrected for regular variations that are mainly related to the atmospheric dynamo processes. Afterwards the amplitude ranges of the perturbations in the two components are determined and assigned a class number from 0 to 9 according to their magnitudes. The larger of the two class numbers is then assigned to the  $K$  index.

## 1 Introduction

#	Observatory				Geographic		Geomagnetic	
	Code	Name	Location	Active	Lat.	Long.	Lat.	Long.
1	LER	Lerwick	Scotland	1932-actual	60° 08'	358° 49'	62.0°	89.4°
2	MEA	Meanook	Canada	1932-actual	54° 37'	246° 40'	61.8°	305.1°
3	SIT	Sitka	USA	1932-actual	57° 03'	224° 40'	60.4°	279.2°
4	ESK	Eskdalemuir	Scotland	1932-actual	55° 19'	356° 48'	57.9°	84.1°
5	LOV	Lovö	Sweden	1954-actual	59° 21'	17° 50'	57.8°	106.7°
6	AGN	Agincourt	Canada	1932-1969	43° 47'	280° 44'	54.4°	350.2°
	OTT	Ottawa	Canada	1969-actual	45° 24'	284° 27'	56.1°	354.8°
7	RSV	Rude Skov	Denmark	1932-1984	55° 51'	12° 27'	55.5°	99.6°
	BFE	Brorfelde	Denmark	1984-actual	55° 37'	11° 40'	55.4°	98.8°
8	ABN	Abinger	England	1932-1957	51° 11'	359° 37'	53.5°	84.6°
	HAD	Hartland	England	1957-actual	50° 58'	355° 31'	54.0°	80.4°
9	WNG	Wingst	Germany	1938-actual	53° 45'	9° 04'	54.2°	95.3°
10	WIT	Witteveen	Netherlands	1932-1988	52° 49'	6° 40'	53.7°	92.4°
	NGK	Niemegk	Germany	1988-actual	52° 04'	12° 41'	51.9°	97.8°
11	CLH	Cheltenham	USA	1932-1957	38° 42'	283° 12'	49.4°	353.5°
	FRD	Fredericksburg	USA	1957-actual	38° 12'	282° 38'	48.8°	352.9°
12	TOO	Toolangi	Australia	1972-1981	-37° 32'	145° 28'	-45.8°	223.0°
	CNB	Canberra	Australia	1981-actual	-35° 18'	149° 00'	-43.1°	226.4°
13	AML	Amberley	New Zealand	1932-1978	-43° 09'	172° 43'	-47.0°	254.2°
	EYR	Eyrewell	New Zealand	1978-actual	-43° 25'	172° 21'	-47.3°	253.9°

**Table 1.1:** The thirteen observatories of the  $K_p$  network. The observatories are listed in the order of their geomagnetic latitude beginning with the highest one (Source: Geoforschungszentrum Potsdam, Germany).

A three-hour time interval was chosen for the derivation of the index since such intervals seemed to be long enough to give correct indications for perturbations of only one hour or two in duration. At the same time, it is short enough not to affect too much of the day in cases where two successive intervals might be affected by a disturbance. The individual  $K$  values measured at the thirteen observatories are transformed into standardized  $K_s$  values. The standardization was introduced in order to avoid local time influences, which are different from season to season. The  $K_p$  index is then defined as the arithmetic average of the  $K_s$  values determined at each of the thirteen stations. The  $K_p$  index is quantized in thirds of an integer by use of the symbols  $-$ ,  $o$ , and  $+$ . Therefore the interval, for example, from 3.5 to 4.5 includes the  $K_p$  values  $4-$ ,  $4o$ , and  $4+$ . The complete  $K_p$  scale consists of the 28 values  $0o$ ,  $0+$ ,  $1-$ ,  $1o$ ,  $1+$ , ...,  $9-$ ,  $9o$ .

The  $AE$  index and the joint  $AU$  and  $AL$  indices were introduced by *Davis and Sugiura* [1966] as a measure of the global auroral electrojet activity. They are derived from geomagnetic variations in the horizontal component observed at twelve auroral zone observatories located in the northern hemisphere between about  $65^\circ$  and  $70^\circ$  magnetic latitude with a lon-

## 1 Introduction

---

gitudinal spacing of  $10^\circ$ – $40^\circ$ . To normalize the data, a base value for each station is first calculated for each month by averaging all the data from the station on the five international quietest days. This base value is subtracted from each value of one-minute data obtained at the station during that month. Then among the data from all the stations at each given universal time (UT), the largest and smallest values are selected. The *AU* and *AL* indices are respectively defined by the largest and the smallest values so selected. The symbols, *AU* and *AL*, derive from the fact that these values form the upper and lower envelopes of the superposed plots of all the data from these stations as functions of UT. The difference, *AU* minus *AL*, defines the *AE* index. The term *AE* indices is usually used to represent all of these indices (*AU*, *AL*, and *AE*). The *AU* and *AL* indices are intended to express the strongest current intensity of the eastward and westward auroral electrojets, respectively. The *AE* index represents the overall activity of the auroral electrojets. The main uncertainties of the *AE* index result from the longitudinal gaps in the distribution of the twelve observatories, from the small latitudinal range covered by these magnetic stations, and from the effects of strong local field-aligned currents.

The ring current index *Dst* was introduced by *Sugiura* [1964] as a measure of the ring current magnetic field and thus its total energy. Since the westward ring current causes a reduction of the terrestrial dipole field, *Dst* is typically negative. The present *Dst* index is based on hourly averages of the northward horizontal component *H* recorded at four low-latitude observatories: Honolulu, San Juan, Hermanus, and Kakioka. All four observatories are  $20^\circ$ – $30^\circ$  away from the dipole equator to minimize equatorial electrojet effects and are about evenly distributed in local time. The uncertainties of the *Dst* index are mainly caused by magnetic contributions of sources other than the ring current to the *H* component measured at the four observatories, namely the magnetopause current, the partial ring current, and the substorm current wedge.

Geomagnetic activity and the strength of the convection electric field are closely related to each other. During times of enhanced convection more particles than usual are injected from the magnetotail into the inner magnetosphere. Some of these particles contribute to the ring current causing a stronger depression of the horizontal component of the terrestrial magnetic field, which is reflected in the *Dst* index. Increased convection also leads to an intensification of particle precipitation into the auroral oval, the ionospheric footprint of the plasma sheet. The precipitation pattern is reflected in the ionospheric conductivity and ultimately, by Ohm's law, in the strength of the auroral electrojets. The magnetic field associated with the current flow of the auroral electrojets induces a perturbation of the Earth's magnetic field, which is expressed by the *AE* indices. The magnetic observatories of the *Kp* network are located at mid-latitudes. During magnetically disturbed periods these stations record the effects of the auroral electrojet current system and of the magnetospheric ring current. Therefore, the *Kp* index is likewise an appropriate measure of magnetospheric convection.

## 1.4 Charged Particle Observations at Geosynchronous Orbit

Geosynchronous orbit lies within a highly variable and dynamic region of the terrestrial magnetosphere. Depending on the upstream solar wind conditions and the magnetospheric activity level and history, a spacecraft at geosynchronous orbit commonly crosses boundaries between several different magnetospheric regions. These include the plasmasphere [Carpenter, 1966; Chappell *et al.*, 1970], the plasma trough [e.g., Taylor *et al.*, 1966], and the plasma sheet [e.g., McIlwain and Whipple, 1986]. On much rarer occasions geosynchronous spacecraft can encounter the lobe [e.g., Rostoker *et al.*, 1975; Sauvaud and Winckler, 1980], the magnetosheath [e.g., Wrenn *et al.*, 1981; Rufenach *et al.*, 1989], and the region just inside the magnetopause which contains magnetosheathlike plasma, the low-latitude boundary layer [e.g., Eastman *et al.*, 1985]. The observation frequencies of the different regions at geosynchronous orbit were identified by McComas *et al.* [1993] in a statistical study using plasma data from the Los Alamos geosynchronous satellites. Their results are summarized in Table 1.2.

	Abbreviation	Percent of Samples
Plasmasphere	PSp	13.1
Plasma trough	PT	22.5
Plasma sheet	PSh	40.3
Both plasma trough and plasma sheet	PT/PSh	18.6
Empty plasma trough	empty	4.3
Magnetosheath and/or low-latitude boundary layer	MSh/BL	0.7
Lobe	lobe	0.3
Other	other	0.2

**Table 1.2:** Regions encountered by the Los Alamos geosynchronous satellites between February 18 and March 31, 1992 [McComas *et al.*, 1993].

The plasma properties at and near geosynchronous orbit have been studied by several different spacecraft, including ATS<sup>1</sup> 1, ATS 5, ATS 6, GEOS<sup>2</sup> 2, and SCATHA<sup>3</sup>. Although much has been learned from these spacecraft about the plasma environment in this region, most previous studies failed to provide a comprehensive statistical analysis of the geosynchronous observations. An exception is the work by Garrett *et al.* [1981a,b] who examined 50 randomly selected days of plasma data from each of the geosynchronous satellites ATS 5 and ATS 6 collected within one year of their launch. However, the statistics presented by these authors have several shortcomings. First of all, the random selection of less than two

---

<sup>1</sup>Applications Technology Satellite.

<sup>2</sup>Geodynamics Experimental Ocean Satellite.

<sup>3</sup>Spacecraft Charging AT High Altitude.

## 1 Introduction

---

months' worth of data spread over a full year raises concerns due to uncertainties caused by the influence of seasonal variations of the plasma parameters. Furthermore, differences in the design of the plasma instrumentation aboard the two spacecraft may result in discrepancies of the plasma parameters measured by the two instruments. Thus the question whether deviations in the statistics obtained from the ATS 5 and ATS 6 satellites (which were launched about five years apart) are hardware-related or have a physical origin such as, for example, a solar cycle dependence, cannot be answered.

During the last decade numerous spacecraft have been added to the fleet of geosynchronous satellites. Among them are five satellites equipped with plasma instrumentation built by the Los Alamos National Laboratory (LANL). The comprehensive database of the plasma instruments, which are all of the same type, contains over 30 satellite years of data covering a complete solar cycle. This database is very suitable for the statistical studies that form the base of this thesis. In the past, the LANL geosynchronous data have resulted in a number of statistical studies, including magnetopause encounters [McComas *et al.*, 1994], lobe encounters [Thomsen *et al.*, 1994; Moldwin *et al.*, 1995], and plasma sheet encounters [Elphic *et al.*, 1999]. However, until now, no statistical analysis of the flux levels has been performed.

A statistical study of the geosynchronous plasma environment is in great demand for various reasons. For one, these statistics are useful for estimating the charging of spacecraft surfaces due to impacting energetic electrons associated with injection events. Spacecraft charging is believed to be a primary cause for satellite operational anomalies, which are found to cluster near local midnight [McPherson *et al.*, 1975]. Furthermore, such statistics may be applied as boundary conditions to inner-magnetospheric models such as, for example, the Magnetospheric Specification Model (MSM) [Garner *et al.*, 1999; Hilmer and Ginet, 2000, and references therein]. Moreover, detailed information on the particle convection in the inner magnetosphere can be derived from the statistical averages of ion and electron fluxes. The latter aspect is covered extensively in this thesis.

This thesis is subdivided into the following chapters: The Los Alamos geosynchronous satellites and the plasma instrumentation are introduced in chapter 2 to the extent necessary for understanding the studies of this thesis. In chapter 3 the plasma observations at geosynchronous orbit obtained during the year 1996 are statistically analyzed. The statistics of the fluxes show distinct boundaries in local time in the energy range typical for the plasma sheet, which may be interpreted as an access phenomenon. If the particle fluxes are high, geosynchronous orbit lies in the plasma sheet, where "fresh" plasma is transported on open drift trajectories from the magnetotail toward and around the Earth. On the other hand, if the fluxes are low, geosynchronous orbit is located in the region of closed drift trajectories that cannot be directly accessed by the particle populations of the plasma sheet. The boundaries separating regions of open and closed particle trajectories, defined as Alfvén layers in section 1.2.4, can be calculated from electric and magnetic field models. A comparison of the observed statistical flux boundaries with the theoretical Alfvén layers obtained from a simple convection model concludes chapter 3. Nowadays much more sophisticated convection models exist that are believed to be more realistic. Therefore, in chapter 4 I expand



## *1 Introduction*

---

on the model/data comparison to address the question whether these advanced models can improve the drift picture in the inner magnetosphere and do even better at reproducing the statistical boundaries.

The particle tomography of the inner magnetosphere in chapter 5 demonstrates an application for the flux statistics. Particles on open drift trajectories should cross geosynchronous orbit twice during their drift from the nightside plasma sheet, through the inner magnetosphere, and out to the dayside magnetopause. The ratio of incoming and outgoing particle measurements at geosynchronous orbit of every drift path thus contains information about particle losses during the drift through the near-Earth region. For ions, these losses are largely caused by charge exchange reactions with hydrogen atoms. Applying tomographic inversion techniques, the observed statistical losses inside the geosynchronous orbit region are used to infer the spatial distribution of exospheric neutral hydrogen.

The framework of this thesis has been expanded in various directions in collaboration with others. These efforts are summarized in chapter 6. Chapter 7 concludes this work with a summary of the most significant results and an outlook on future research opportunities.

## 2 Spacecraft and Plasma Instrumentation

### 2.1 Overview

Los Alamos National Laboratory operates several satellites at geosynchronous orbit that contain particle detectors as part of the payload in order to monitor the plasma environment the spacecraft operate in. To date, five satellites equipped with electrostatic analyzer instruments called Magnetospheric Plasma Analyzers (MPAs) have been launched. The locations of the spacecraft with the international designators 1989-046, 1990-095, 1991-080, 1994-084, and LANL-97A are shown in Figure 2.1. The satellites are spin-stabilized and

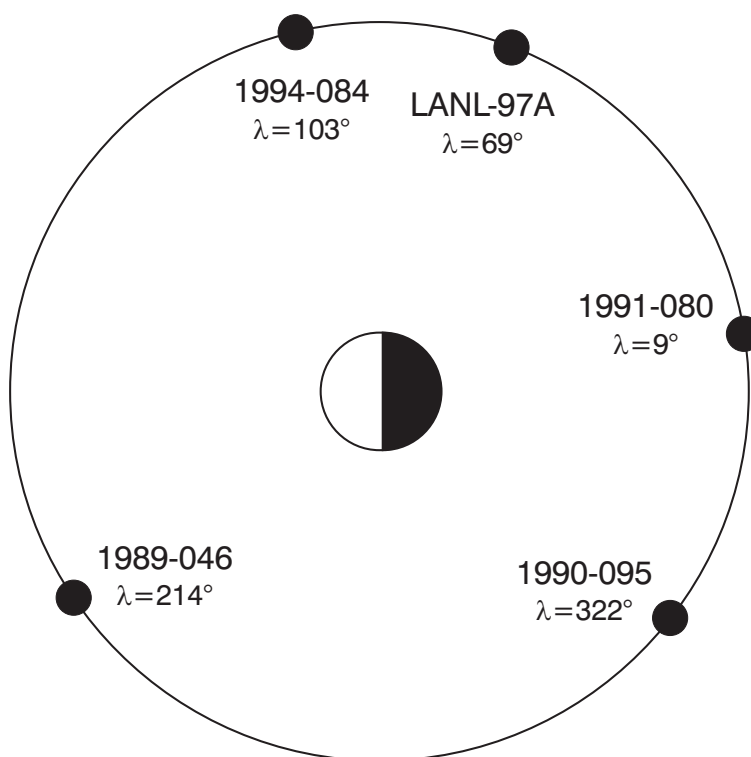


**Figure 2.1:** Configuration of the Los Alamos geosynchronous spacecraft with MPA instruments at 0000 UT on January 1, 1998. Each satellite is labeled with its international designator and its geographic east longitude  $\lambda$ .

spin with a nominal spin rate of 6 rpm (10 s spin period) about an axis which is continuously oriented toward the center of the Earth.

### 2.2 Electrostatic Analyzers

An electrostatic analyzer (ESA) consists of either two cylindrical or two spherical section plates. When a voltage is applied between the plates, incoming charged particles are deflected by an amount proportional to the applied voltage. Only charged particles within a specific range of velocities will be transmitted by the analyzer. Therefore, an electrostatic analyzer can be understood as a particle filter. Even though a large variety of instrument designs exist today, their operating principle is based upon the same basic theory that has been previously discussed by many authors [e.g., *Purcell*, 1938; *Rodgers*, 1951; *Ritchie et al.*, 1960; *Paolini and Theodoridis*, 1967; *Theodoridis and Paolini*, 1969].

Figure 2.2 illustrates the geometry of a curved plate analyzer in the plane of the orbit of a particle with charge  $q$ , mass  $m$ , speed  $v$ , and azimuth angle  $\alpha$  incident at radial distance  $r_0$  between the plates of the analyzer. A particle entering the radial electric field halfway between the analyzer plates at an angle of  $\alpha = 0^\circ$  moves in a circular orbit if the radially outward directed centrifugal force and the radially inward pointing Coulomb force are equal:

$$\frac{mv^2}{R_{av}} = q \frac{V}{\Delta R}, \quad (2.1)$$

where  $V = V_2 - V_1$  is the voltage difference between the outer plate ( $V_2$ ) and the inner plate ( $V_1$ ),  $\Delta R = R_2 - R_1$  is the gap between the analyzer plates, and  $R_{av} = (R_1 + R_2)/2$  is the average radius of the gap. Note that the voltage drop between the analyzer plates has to be applied appropriately for the particle species to be measured. For detection of electrons the inner plate must be charged positively with respect to the outer plate, while for ions the polarity of the voltage needs to be reversed.

Rewriting (2.1) as

$$\frac{\frac{1}{2}mv^2}{q} = \frac{V}{2} \frac{R_{av}}{\Delta R}, \quad (2.2)$$

it can be seen that the ESA identifies the energy per charge ( $E/q$ ) of a particle. As a consequence, the velocity and charge state of transmitted ions cannot be unambiguously distinguished. Equation (2.2) also shows that the potential required for the electric field is only a fraction of the incident particle energy per charge. The analyzer constant relating particle energy to applied analyzer voltage is dependent on the ratio of the average plate radius to plate spacing  $R_{av}/\Delta R$ . It usually ranges from  $\sim 5$  to  $\sim 50$  [*Young*, 1998].

In reality, a radial component to the particle motion exists in addition to the azimuthal one, which leads to elliptically shaped particle orbits within the analyzer [e.g., *Goldstein*, 1980, pp. 76–82]. The equation of the orbit then has the form [*Ritchie et al.*, 1960]:

$$r^{-1} = [(1 + \delta)r_0 \cos^2 \alpha]^{-1} + A \sin \varphi + B \cos \varphi, \quad (2.3)$$

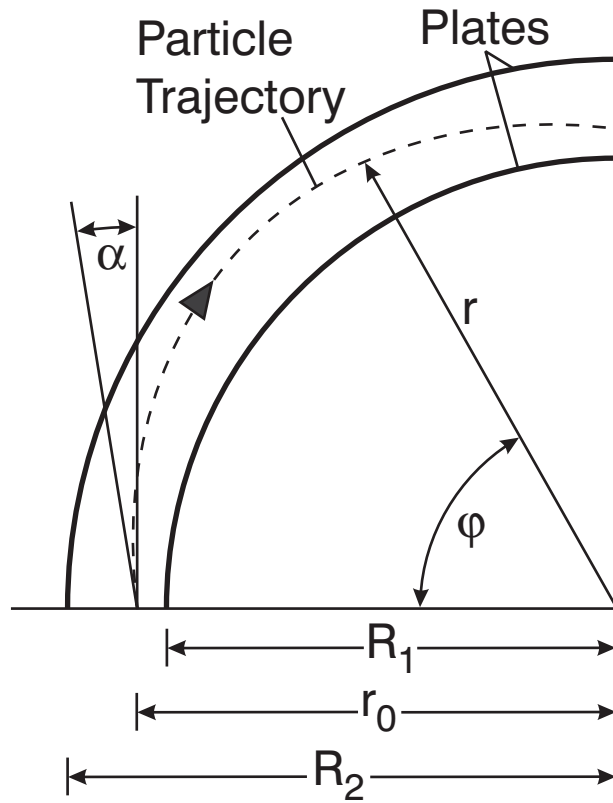


**Figure 2.2:** A schematic representation of a cross section of a curved plate analyzer in the plane of the orbit of a charged particle incident at  $r_0$  (after *Gosling et al.* [1978]). The angle  $\alpha$  is positive as drawn.

where  $r$  and  $\varphi$  are the radial and angular position of the particle,  $r_0$  is the initial radial distance of the particle, and  $\alpha$  is the incident azimuth angle. The energy parameter  $\delta$  is defined by

$$\delta = \frac{E - E_0}{E_0}, \quad (2.4)$$

where  $E = mv^2/2$ , and  $E_0$  is the kinetic energy of a particle which executes a circular orbit of radius  $r_0$ . The values of  $A$  and  $B$  are determined by the initial conditions at  $\varphi = 0^\circ$  which are  $r = r_0$  and  $(1/r_0) dr/d\varphi = \tan \alpha$ :

$$A = -\frac{\tan \alpha}{r_0} \quad \text{and} \quad B = \frac{1}{r_0} \left[ 1 - \frac{1}{(1 + \delta) \cos^2 \alpha} \right]. \quad (2.5)$$

Because of the nature of elliptical particle trajectories, a finite range of initial azimuths and energies are transmitted for a given voltage on the analyzer plates. A more detailed discussion of the passband is given by *Gosling et al.* [1984].

### 2.3 The MPA Instrument

The Magnetospheric Plasma Analyzer is a low weight and power electrostatic analyzer (3.6 kg and 3.5 W), designed to measure three-dimensional  $E/q$  distributions of both ions and electrons in the energy range of  $\sim 1$  eV/ $q$  to  $> 40$  keV/ $q$  with high sensitivity [Bame *et al.*, 1993]. This energy range usually covers the bulk of the particle populations in space plasmas, such as those found in the terrestrial magnetosphere. The MPA field-of-view (FOV) is oriented normal to the spin axis and covers the polar angle range of  $\pm 66^\circ$  about the spacecraft spin equator. Because of the nature of the spin orientation, these spacecraft provide excellent viewing northward and southward along the local magnetic field lines as well as eastward and westward along their orbits. The technical and physical parameters of the MPA instrument are summarized in Table 2.1.

Parameter	Value		
Bending angle	60°		
Average radius [mm]	53		
Plate gap [mm]	1.93		
Analyzer constant ( $R_{av}/\Delta R$ )	27.5		
Aperture length	13.7°		
Number of polar angle detectors	6		
Polar angle field-of-view per detector	$\sim 15^\circ$ FWHM		
Polar angle detector locations	$\pm 11.5^\circ$	$\pm 34.5^\circ$	$\pm 57.5^\circ$
Azimuthal response (full width of half maximum)	8°	12°	21°
Geometric factors [ $\text{cm}^2 \text{sreV/eV}$ ]	$5.7 \times 10^{-4}$	$4.9 \times 10^{-4}$	$3.3 \times 10^{-4}$
Energy range			
Electrons	$\sim 1$ eV – 40 keV		
Ions	$\sim 1$ eV – 44 keV		
Energy resolution ( $\Delta E/E$ )	0.40		

**Table 2.1:** The MPA instrument parameters.

A simplified schematic of the MPA ion and electron optics is illustrated in Figure 2.3. The electrostatic analyzer is composed of a single set of 60° bending angle analyzer plates followed by a set of six channel electron multipliers (CEMs). Charged particles transmitted by the analyzer at a fixed applied voltage are admitted to the CEMs. Here they strike the inner semiconducting surfaces of the device, spawning a cascade of secondary electrons. The entry of a single particle into a CEM results in a pulse of approximately  $10^8$  electrons that are collected by an anode at the exit of the CEM. The increase in sensitivity achieved by this amplification technique allows for single particle counting capability. The six CEMs provide simultaneous measurements of different polar angle FOV look directions centered at  $\pm 11.5^\circ$ ,  $\pm 34.5^\circ$ , and  $\pm 57.5^\circ$  with respect to the spacecraft spin equator (cf. Figure 2.3).

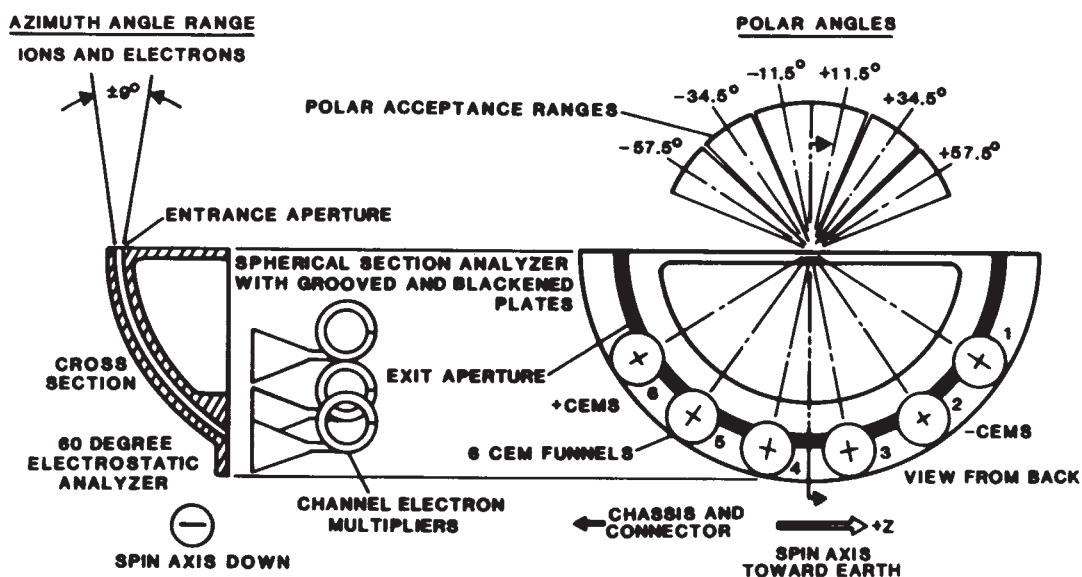


**Figure 2.3:** Cross-sectional view of the MPA charged particle optics system, on the left. A view of the system on the right, taken from behind the analyzer, shows the locations of the six CEM funnels and their nominal polar angle fields-of-view (from *Bame et al.* [1993]).

The spacecraft spin allows the MPA instrument to view over 90% of  $4\pi$  sr each complete rotation (see Figure 2.4).

As mentioned above, the MPA instrument makes observations of both ions and electrons which are analyzed separately using two identical analyzer voltage supplies. These voltage supplies provide positive-polarity sweep voltages from +3280 V to +0.08 V on opposite ESA plates. For electrons, the sweep voltage is applied to the inside plate with the outside plate at 0 V, and for ions the sweep is applied to the outside plate with the inside plate at 0 V. The upper energy limit for analyzed electrons is  $40.4 \text{ keV}/q$  while for ions it is  $43.6 \text{ keV}/q$ . The difference in limits is due to the fact that electrons are accelerated into the analyzer by the analyzer voltage, while ions are decelerated. The nominal lower-energy limit of the MPA instrument is 1 eV. In order to detect the lowest-energy particles of both species with high efficiency, these particles are post-accelerated from the ESA into the CEM funnels.

### 2.4 MPA Operation: Modes and Cycles

The MPA instrument usually operates with a fixed sequence that is used in several commandable modes. The “NORMAL” mode is used almost all of the time. The “BACKGROUND” mode uses the same sequence as the normal mode except that it is run with the analyzer voltage supplies turned off, so that penetrating particle and solar UV-induced background can be evaluated. Furthermore, some calibration modes are available for in-

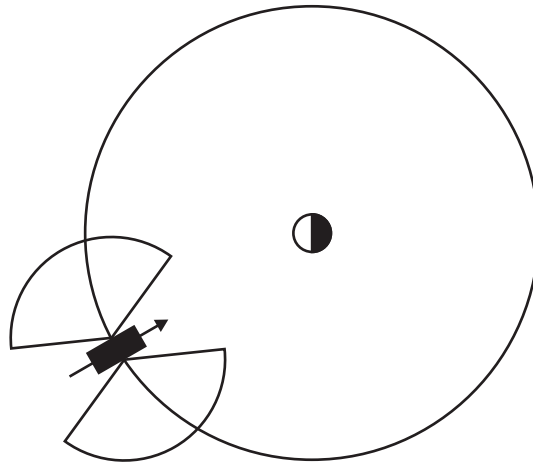


**Figure 2.4:** Owing to the spacecraft spin, the MPA field-of-view covers over 90% of  $4\pi$  sr. The spin axis of the spacecraft, indicated by the arrow, is continuously pointed toward the center of the Earth.

flight adjustment of the instrument.

The fixed sequence of operation that is run in most modes is composed of five types of cycles arranged in an eight cycle sequence that is repeated every 86 s. The order of the sequence is

$$P3 P\theta E3 E2 E\theta P3 E2 E2,$$

where the letters “*E*” and “*P*” refer to electron and ion modes, while the “2”, “3”, and “ $\theta$ ” refer to two-dimensional, three-dimensional, and high-angular-resolution modes, respectively.

During the analyzer voltage sweeps of the two- and three-dimensional cycles, counts are accumulated in 40 contiguous 9-ms counting intervals which are approximately logarithmically spaced in energy. A complete sweep thus requires 360 ms and is followed by a 63-ms recharge of the voltage supply. Approximately 24 sweeps take place during one 10-s revolution of the spacecraft, resulting in an azimuthal resolution of  $\sim 15^\circ$ . Hence a full three-dimensional distribution is characterized by 5760 samples (40 energy  $\times$  24 azimuth  $\times$  6 polar). In the two-dimensional cycles the counts from the six CEMs are summed. These distributions are thus characterized by 960 samples (40 energy  $\times$  24 azimuth  $\times$  1 summed polar). The high-angular-resolution mode provides 99-ms samples every  $3.3^\circ$  of the spacecraft spin for each CEM at a single energy level. For ions these observations are made at the energy of the peak of the most recent three-dimensional ion distribution; for electrons these are made essentially always at  $\sim 120$  eV. In this thesis the measurements from the *P3* and *E3* cycles are used exclusively.

### 2.5 Data Products

#### 2.5.1 Distribution Functions

The MPA instruments are particle counters and their immediate data products are count rates. These count rates are converted to distribution functions by the following procedure, which is described in detail by *Thomsen et al.* [1999]. In a first step, the count rates are corrected for the dead time in the electronics. At times of high count rates, the dead time reduces the measured count rate compared to the true rate. This reduction is reversible by applying the expression

$$C = \frac{C'}{1 - C'(t_d/\tau)}, \quad (2.6)$$

where  $C'$  is the number of counts measured in one accumulation interval  $\tau$  (9 ms),  $t_d = 1.2 \mu\text{s}$  is the relevant dead time [*Bame et al.*, 1993], and  $C$  is the estimated number of true counts per accumulation interval. The true count rates are then corrected for the background counts. Charged particles with sufficiently high energies (typically above  $\sim 1$  MeV for electrons and 10's of MeV for ions) can penetrate directly through the MPA instrument and be detected by the CEMs. Such energetic populations thus produce a background count rate in the detectors which is independent of the analyzer plate voltage. Since all energy channels have the same accumulation interval, the background counts are independent of the energy level.

From the background-corrected count rates,  $C_{ijk}$ , the *differential particle flux*  $F$  is computed within the warm plasma approximation (i.e., that the distribution is uniform over the energy/angle response of the instrument):

$$F_{ijk} [\text{cm}^{-2} \text{s}^{-1} \text{sr}^{-1} \text{eV}^{-1}] = \frac{C_{ijk}}{\tau \varepsilon_{ij} G_j E_i}, \quad (2.7)$$

where  $C_{ijk}$  is the count rate measured by the  $j^{\text{th}}$  detector at particle energy  $E_i$  and sweep number  $k$ ,  $\varepsilon_{ij}$  is the efficiency of the detector  $j$  at energy  $E_i$ ,  $G_j$  is the geometric factor of detector  $j$ , and  $\tau$  is the sample accumulation time (9 ms). The energy  $E_i$  is given in units of eV.

The *phase space density*  $f$  is derived from the differential particle flux as [*Baumjohann and Treumann*, 1997, p. 121]

$$f = \frac{m^2}{2E} F, \quad (2.8)$$

which gives

$$f_{ijk} [\text{cm}^{-6} \text{s}^3] = \frac{K_s F_{ijk} [\text{cm}^{-2} \text{s}^{-1} \text{sr}^{-1} \text{eV}^{-1}]}{E_i [\text{eV}]}, \quad (2.9)$$

where for electrons the species-specific constant  $K_s = m^2/2$  is

$$K_s = K_e = 1.616 \times 10^{-31} [\text{eV}^2 \text{cm}^{-4} \text{s}^4], \quad (2.10)$$



## 2 Spacecraft and Plasma Instrumentation

---

and for ions it is

$$K_s = K_p = 5.449 \times 10^{-25} [\text{eV}^2 \text{cm}^{-4} \text{s}^4], \quad (2.11)$$

assuming that all ions are protons.

Another quantity that is often used in space plasma physics is the *differential energy flux*. The latter is defined as the product of the differential particle flux times the particle energy. The energy flux drops off less rapidly than the particle flux, and this representation is thus often used to highlight features in the high-energy tail of a particle distribution.

It should be noted that the energy  $E_i$  in (2.7) and (2.9) is the measured energy of the particles. Due to surface charging of the spacecraft, the measured energy  $E$  is usually not equivalent to the actual energy of the particles at infinity  $E_\infty$ . However, these energies are related to each other by

$$E = E_\infty - q\Phi_{\text{sc}}, \quad (2.12)$$

where  $q$  is the particle charge, and  $\Phi_{\text{sc}}$  is the spacecraft potential. The level of surface charging of a satellite is determined by the balance of several different currents. These currents include the photoelectron current, the current due to ambient electrons, the current due to ambient ions, and the current due to ejected secondary electrons. If these currents are unbalanced, the spacecraft will charge up, enhancing some of the currents and reducing others until the balance between the currents is reestablished. During substorm injections, the flux of hot electrons increases dramatically, causing a satellite to charge to large negative potentials relative to the ambient medium. As a consequence, ions are accelerated as they approach the negatively charged spacecraft and electrons are decelerated. To accurately calculate velocity moments from these populations it is necessary to correct the energy levels for the spacecraft potential using (2.12).

### 2.5.2 Velocity Moments

At times it may be desirable to express the characteristics of a particle population using macroscopic quantities such as number density, bulk flow velocity, and average temperature, which are the *velocity moments* of the distribution function  $f(\underline{v}, \underline{r}, t)$  [Baumjohann and Treumann, 1997, p. 125]:

$$\mathcal{M}_i(\underline{r}, t) = \int f(\underline{v}, \underline{r}, t) \underline{v}^i d^3v, \quad (2.13)$$

where  $\underline{v}^i$  denotes the  $i$ -fold dyadic product, a tensor of rank  $i$ . The number of moments which can be calculated from the distribution function is in principle infinite. However, only the first few are commonly used to describe the properties of a particle population: The number density  $n$  is given by the zero-order moment

$$n = \int f(\underline{v}) d^3v, \quad (2.14)$$

the mean or bulk flow velocity  $\underline{v}_b$  is defined by the first-order moment

$$\underline{v}_b = \frac{1}{n} \int \underline{v} f(\underline{v}) d^3v, \quad (2.15)$$

## 2 Spacecraft and Plasma Instrumentation

---

and the calculation of the pressure tensor  $\underline{\underline{P}}$  is based on the second-order moment

$$\underline{\underline{P}} = m \int (\underline{v} - \underline{v}_b)(\underline{v} - \underline{v}_b) f(\underline{v}) d^3v. \quad (2.16)$$

The pressure tensor consists of a trace and the traceless off-diagonal part. The former gives, in an isotropic plasma, the isotropic pressure  $p = nk_B T$ , in an anisotropic plasma the anisotropic pressure. The traceless part contains the stresses in the plasma. The thermal pressure  $p$  can be used to define the kinetic temperature of the plasma component:

$$\underline{\underline{T}} = \frac{m}{3k_B n} \int (\underline{v} - \underline{v}_b)(\underline{v} - \underline{v}_b) f(\underline{v}) d^3v. \quad (2.17)$$

The kinetic temperature is a measure of the spread of the particle distribution in velocity space. The temperature tensor can be diagonalized to find the symmetry axis of the distribution, i.e., the magnetic field direction [Thomsen *et al.*, 1996].

For computation of the MPA moments, the integral moments  $\mathcal{M}_i$  are approximated as weighted sums of the phase space density over finite velocity-space elements. The moments are determined separately for the following particle populations: Low-energy ions ( $\sim 1$  eV –  $\sim 100$  eV), high-energy ions ( $\sim 100$  eV –  $\sim 45$  keV), and high-energy electrons ( $\sim 30$  eV –  $\sim 45$  keV). A detailed description of the MPA moments calculations is given by Thomsen *et al.* [1999].

### 2.5.3 Reported Products

The distribution functions and moments computed from the satellite raw data are reported using five different data formats: one VAX binary file, two ASCII<sup>1</sup> files (Unix and VAX), and two CDF<sup>2</sup> files (ISTP<sup>3</sup> key parameters and high-resolution data). The flagship data product is the high-resolution CDF files that contain the full three-dimensional particle distributions. The size of these CDF files is approximately 50 Mb per satellite and day depending on coverage. The other data formats represent reduced data sets, which contain spin-averaged fluxes from detectors 3 and 4 at each ion and electron energy level instead of the full three-dimensional distributions. The file size of these data products is of the order of 2 Mb per satellite and day. Due to computational limitations the reduced data set of the Unix ASCII files is used exclusively in this thesis.

---

<sup>1</sup>American Standard Code for Information Interchange.

<sup>2</sup>Common Data Format, file format developed by NASA.

<sup>3</sup>International Solar Terrestrial Physics, NASA conducted research program.

# 3 Plasma Sheet Access to Geosynchronous Orbit

## 3.1 Overview

One year's worth of Magnetospheric Plasma Analyzer data from three Los Alamos geosynchronous satellites are used for a statistical study of proton and electron fluxes at geosynchronous orbit and their dependence on local time (LT) and geomagnetic activity level as measured by  $Kp$ . When displayed as a function of LT and  $Kp$ , the fluxes exhibit distinct boundaries, which are shown to be consistent with a combination of a global pattern of particle drift through the magnetosphere and loss processes mainly due to charge exchange of the ions and auroral precipitation of the electrons. A Hamiltonian energy conservation approach combined with the  $(U, B, K)$  coordinate transformation introduced by *Whipple* [1978] is used to calculate the theoretical position of the separatrix between open and closed drift trajectories (Alfvén layer) as a function of particle species, energy, local time, and geomagnetic activity level. The comparison of the theoretical boundaries with the observations confirms the predictions of plasma sheet access to the geosynchronous region. The analysis also provides independent statistical support for previously derived relationships between  $Kp$  and the strength of the global convection electric field.

## 3.2 Introduction

The plasma sheet represents an important region in the Earth's magnetosphere that is the source of the higher-energy particle population that is injected into the inner magnetosphere during magnetic substorms [e.g., *DeForest and McIlwain*, 1971; *McComas et al.*, 1993; *Birn et al.*, 1997; *Kerns et al.*, 1994; *Burke et al.*, 1995; *Liemohn et al.*, 1998]. Furthermore, the plasma sheet is believed to be the direct source of ring current particles [e.g., *Smith et al.*, 1979; *Chen et al.*, 1994]. For this reason many ring current simulations have used the plasma sheet properties as an outer boundary condition for their calculations [e.g., *Wolf et al.*, 1982; *Chen et al.*, 1994; *Fok et al.*, 1996]. The simulations have shown that the plasma sheet density has a direct influence on the strength of the ring current. More recent simulations actually use geosynchronous observations as boundary conditions [*Jordanova et al.*, 1998; *Kozyra et al.*, 1998b; *Liemohn et al.*, 1999]. Such measurements provide a

### 3 Plasma Sheet Access to Geosynchronous Orbit

---

direct means of determining whether or not in any given event the plasma sheet has access to geosynchronous orbit and hence to the inner magnetosphere. The purpose of this study is to explore on a statistical basis the conditions under which plasma sheet material has access to geosynchronous orbit and to compare that statistical assessment with the expectations based on a simple model of convective transport in the inner magnetosphere.

In this study I expand on previous work by *Maurice et al.* [1998], who examined the hot-ion properties at geosynchronous orbit under quiet magnetospheric conditions. I use the large database of MPA data described in chapter 2 to address statistically the question of the access of plasma sheet material to geosynchronous orbit and its dependence on local time and geomagnetic activity. The observations are compared with the access predicted for particle drifts in global magnetic and electric fields. I find that the plasma sheet particles do, in fact, have access to geosynchronous orbit, except for particles with higher energies during times of very low magnetic activity. Moreover, on a statistical basis, the access of particles to this region can be understood with the conventional drift paradigm, and the  $Kp$  index provides an appropriate proxy for the strength of the convection.

### 3.3 Particle Drift Description

As discussed in section 1.2.1, the guiding center drift velocity of a particle within the Earth's magnetosphere can be expressed as

$$\mathbf{v}_D = \frac{\mathbf{E} \times \mathbf{B}}{B^2} + \frac{W_{\text{kin},\perp}}{qB^3} (\mathbf{B} \times \nabla B) + \frac{2W_{\text{kin},\parallel}}{q} \frac{\mathbf{R}_c \times \mathbf{B}}{R_c^2 B^2}, \quad (3.1)$$

where  $\mathbf{E}$  is the macroscopic electric field;  $\mathbf{B}$  is the magnetic field;  $W_{\text{kin},\parallel} = \frac{1}{2}mv_{\parallel}^2$  and  $W_{\text{kin},\perp} = \frac{1}{2}mv_{\perp}^2$  are the particle's kinetic energies parallel and perpendicular to  $\mathbf{B}$ , respectively; and  $\mathbf{R}_c$  is the local radius of curvature of the magnetic field line.

The complex drift trajectories resulting from (3.1) can be well described by a Hamiltonian energy conservation approach with an appropriate coordinate transformation [Whipple, 1978]. The main idea is the following: If a particle of arbitrary charge, energy, and pitch angle conserves the first two adiabatic invariants, it also conserves its total energy [e.g., Wolf, 1995]. For a time-stationary magnetic field (hence neglecting any inductive electric fields) the electric field can be written as the gradient of a scalar potential  $U$ . Thus the total energy is

$$W_{\text{tot}} = qU + W_{\text{kin}} = qU + \mu B_m, \quad (3.2)$$

where  $B_m(K)$  is the magnetic field intensity at the mirror point,  $K$  is the modified second invariant defined in section 1.2.3, and  $\mu = mv_{\perp}^2/2B$  is the magnetic moment. Note that at the mirror locations  $W_{\text{kin},\parallel} = 0$  since  $v_{\parallel} = 0$ . Owing to the conservation of total energy, a coordinate transformation into the  $(U, B, K)$  space leads to simple drift trajectories [Whipple,

### 3 Plasma Sheet Access to Geosynchronous Orbit

---

1978], since

$$\frac{dW}{dt} = \frac{d(\mu B_m)}{dt} + \frac{d(qU)}{dt} = 0, \quad (3.3)$$

$$\Rightarrow d(\mu B_m) + d(qU) = 0, \quad (3.4)$$

$$\Rightarrow \underbrace{\mu dB_m + B_m d\mu}_{=0} + q dU + \underbrace{U dq}_{=0} = 0, \quad (3.5)$$

results in

$$\boxed{\frac{\partial U}{\partial B_m} = -\frac{\mu}{q}}. \quad (3.6)$$

Equation (3.6) states that all particle drift trajectories in the  $(U, B, K)$  space are straight lines with the slope  $-\mu/q$ . For a dipole magnetic field and a Volland-Stern electric potential, the mapping into the  $(U, B, K)$  space is double valued [cf. *Whipple, 1978*]. This ambiguity can be resolved by splitting the magnetosphere into a dayside and a nightside portion. The boundary between the two halves of the magnetosphere is the locus of all points where the magnetic field intensity reaches an extremum on the equipotentials. For the electric and magnetic field models considered in this chapter, the separator is the dawn-dusk meridian. A detailed analysis of the separator location for more general field models is given in section 4.3.1.

The Volland-Stern potential configuration due to superposition of a shielded cross-tail field with a corotation field was previously discussed in section 1.2.2 and is repeated here for the reader's convenience:

$$U(r, \varphi) = -\frac{a}{r} - E_0 r^\gamma \sin(\varphi), \quad (3.7)$$

where  $r$  is the distance from the center of the Earth,  $\varphi$  is the magnetic local time referred to noon rather than midnight,  $\gamma$  is the shielding exponent, and  $a$  is the corotation constant. The coefficient  $E_0$  determines the cross-tail electric field strength, which varies with the level of geomagnetic activity. A number of authors have expressed  $E_0$  as a function of the  $Kp$  index. The present study provides an independent assessment of the suitability of some of these parameterizations.

As pointed out in section 1.2.4, a potential function of the form of (3.7) produces two classes of equipotentials: Near the Earth there is a class of potential contours which are continuous around the Earth, corresponding to cold-plasma drift trajectories that are closed; at larger distances, the potential contours extend from the geomagnetic tail, in toward and around the closed-contour region and out to the dayside magnetopause. At dusk the separatrix between open and closed equipotentials corresponds to a stagnation point in the flow, i.e.,  $\partial U/\partial r = 0$ . The distance at 1800 LT to this separatrix between open and closed cold-plasma drift trajectories can be calculated from (3.7), applying a clock angle of  $\varphi = \pi/2$ :

$$U\left(r, \frac{\pi}{2}\right) = -\frac{a}{r} - E_0 r^\gamma. \quad (3.8)$$

### 3 Plasma Sheet Access to Geosynchronous Orbit

---

The derivative of (3.8) with respect to  $r$  is given by

$$\frac{dU\left(r, \frac{\pi}{2}\right)}{dr} = \frac{a}{r^2} - E_0 \gamma r^{\gamma-1}. \quad (3.9)$$

Therefore, the distance of the stagnation point  $r_s$  is subject to the requirement that

$$\frac{a}{r_s^2} - E_0 \gamma r_s^{\gamma-1} = 0 \quad (3.10)$$

and found to be

$$r_s = \left( \frac{a}{\gamma E_0} \right)^{\frac{1}{\gamma+1}}. \quad (3.11)$$

Similarly, the strength of the convection can be obtained as a function of  $r_s$  from (3.10):

$$E_0 = \frac{a}{\gamma r_s^{\gamma+1}}. \quad (3.12)$$

The relationship between  $r_s$  and the radial distance to the separatrix equipotential at midnight  $r_m$  can be derived from the equality of the electric potential at both locations:

$$U\left(r_s, \frac{\pi}{2}\right) = U(r_m, \pi), \quad (3.13)$$

$$\Rightarrow -\frac{a}{r_s} - E_0 r_s^\gamma = -\frac{a}{r_m}. \quad (3.14)$$

Substituting (3.12) for  $E_0$  yields

$$r_m = \frac{r_s}{1 + \frac{1}{\gamma}}. \quad (3.15)$$

The combination of (3.12) and (3.15) then provides a relationship between the cross-tail electric field intensity and the equatorial distance of the separatrix at midnight:

$$E_0 = \frac{a}{\gamma \left(1 + \frac{1}{\gamma}\right)^{\gamma+1} r_m^{\gamma+1}}. \quad (3.16)$$

The nightside separatrix should approximately mark the inner edge of the electron plasma sheet [e.g., *Elphic et al.*, 1999, and references therein]. As argued by previous authors, the inner edge of the electron plasma sheet maps down to the equatorward boundary of the auroral oval [*Gussenhoven et al.*, 1981, 1983]. Denoting the invariant latitude of this boundary at midnight as  $\lambda_m$ , one thus obtains for a dipole field:

$$\boxed{E_0 = \frac{a}{\gamma \left(1 + \frac{1}{\gamma}\right)^{\gamma+1} (\cos^2 \lambda_m)^{\gamma+1}}}. \quad (3.17)$$

### 3 Plasma Sheet Access to Geosynchronous Orbit

---

The latitude of the equatorward edge of the diffuse aurora has been determined from DMSP<sup>1</sup> measurements of precipitating plasma sheet electrons and has been shown to be well correlated with  $Kp$  [Gussenhoven *et al.*, 1981, 1983]. From a large body of DMSP measurements, Gussenhoven *et al.* found the empirical relationship  $\lambda_m = 67.8 - 2.07 Kp$ . Inserting this expression into (3.17) thus provides a method for obtaining the cross-tail electric field as a function of  $Kp$ , which will be referred to as the *Gussenhoven method*.

Another parameterization for the cross-tail electric field was derived by Maynard and Chen [1975] from OGO<sup>2</sup> 3 and 5 midnight plasmopause crossing data. For a shielding exponent  $\gamma=2$  the cross-tail electric field dependence on the  $Kp$  index was found to be  $E_0 = 0.045 / (1 - 0.159 Kp + 0.0093 Kp^2)^3$ . This expression for the strength of the convection field will be referred to as the *Maynard method* in this chapter.

For simplicity only equatorially mirroring particles are considered hereafter. As a result the modified second adiabatic invariant  $K$  is zero at all times and hence can be ignored. It should be noted that a comparison of this simplification with the observations will not be strictly valid since my study involves spin-averaged flux data. However, the observed ratio of perpendicular to parallel temperature is usually greater than 1 ( $T_{\perp}/T_{\parallel} = 1.25$  (median), 1.12 (25th percentile), 1.36 (75th percentile)), indicating that pitch angles closer to  $90^\circ$  are favored, so the  $K=0$  assumption should still provide a reasonable comparison.

With a dipole magnetic field in the equatorial plane given by  $B(r, \varphi) = B_E / r^3$  (see section 1.2.2), the potential at the dawn-dusk terminator becomes

$$U(B) = \pm E_0 \left( \frac{B_E}{B} \right)^{\frac{\gamma}{3}} - a \left( \frac{B}{B_E} \right)^{\frac{1}{3}}, \quad (3.18)$$

where the positive sign represents the dawn terminator ( $\varphi = -\pi/2$ ) and the negative sign gives the dusk terminator ( $\varphi = +\pi/2$ ). Figure 3.1a shows the terminators, labeled  $T_{\text{Dawn}}$  and  $T_{\text{Dusk}}$ , in  $(U, B)$  coordinates calculated from (3.18) for a shielding factor of  $\gamma=1$  and a cross-tail electric field strength of  $E_0 = 1.94 \text{ kV}/R_E$ , which corresponds to  $Kp=5$  in the Gussenhoven model. The Cartesian equivalent of Figure 3.1a is illustrated in Figure 3.1b, where the terminators are depicted by the dawn-dusk meridian.

The area enclosed by the dawn and dusk terminators in the  $(U, B)$  coordinate system represents the space of allowed combinations of  $U$  and  $B$  in which the particle trajectories are given by the straight lines (3.6). Using this approach, open and closed drift trajectories are easily distinguished. Open drift paths originate deep in the magnetotail, corresponding to the low-magnetic-field region near the  $U$  axis. The particles then advance in direction of increasing magnetic field strength until they arrive at either terminator. At the separator the direction of particle motion is reversed toward decreasing  $B$ , where the particles escape to the dayside magnetopause. The green curves in Figures 3.1a and 3.1b illustrate an example of an open drift trajectory for a 10-keV electron.

---

<sup>1</sup>Defense Meteorological Satellite Program.

<sup>2</sup>Orbiting Geophysical Observatory.

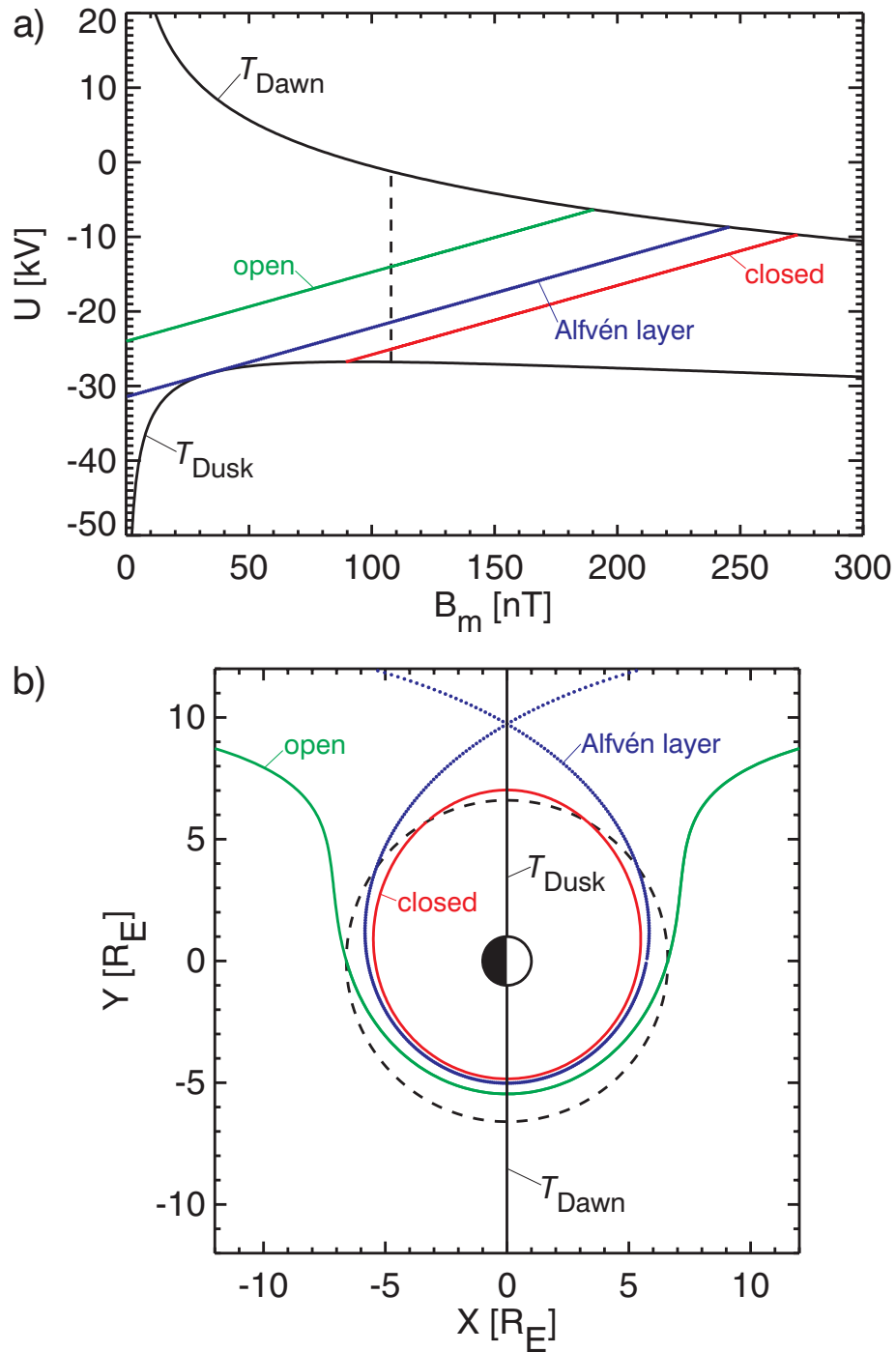


**Figure 3.1:** (a) Illustration of the  $(U, B)$  coordinate system. The terminators (black curves), labeled  $T_{\text{Dawn}}$  and  $T_{\text{Dusk}}$ , are obtained from the Gussenhoven  $\gamma=1$  model for  $Kp=5$  ( $E_0 = 1.94 \text{ kV}/R_E$ ). Examples of open and closed drift trajectories of 10-keV electrons are represented by green and red lines, respectively. The regions of open and closed particle orbits are separated from each other by the 10-keV electron Alfvén layer (blue line), which is tangent to the dusk terminator. (b) The Cartesian equivalent of Figure 3.1a.



### 3 Plasma Sheet Access to Geosynchronous Orbit

---

Particles on closed drift paths usually move repeatedly between the dawn and dusk terminators (red curve in Figure 3.1a) corresponding to particle orbits that are closed around the Earth (see Figure 3.1b). An exception are closed ion drift trajectories in a very limited energy range, which may be connected to the dusk separator at both ends (see Figure 3.2a). As shown in Figure 3.2b, these drift paths do not encircle the Earth and are referred to as “banana” orbits [cf. *Roederer, 1970; Sheldon and Gaffey, 1993*].

Within this drift scenario, particle fluxes should be organized by the boundaries between open and closed drift trajectories. These boundaries are the Alfvén layers discussed in section 1.2.4 (blue curves in Figures 3.1 and 3.2) and can be identified in the  $(U, B)$  space as the straight lines (3.6) that are tangent to the curves (3.18) [*Whipple, 1978*]. By transforming the coordinates of these straight lines from the  $(U, B)$  space back into the Cartesian space, the Alfvén layers for protons and electrons are obtained. Figures 3.3 and 3.4 (left and middle) show the Alfvén boundaries derived for various energies at  $Kp = 0$  and  $Kp = 4$  evaluated with the Gussenhoven  $\gamma = 2$  model. The Earth is shown in the center of each graph, and the dashed circle is the location of geosynchronous orbit at a distance of  $6.6 R_E$  from the Earth’s center. Figures 3.3 and 3.4 (right) show the corresponding local time of the Alfvén boundary at geosynchronous orbit for  $Kp$  ranging from 0 to 9. The shaded regions show the local time ranges for which geosynchronous orbit lies inside the separatrixes, on closed drift paths. For example, Figures 3.3 and 3.4 show that at low values of  $Kp$  (i.e., for weak convection), the higher-energy position of the plasma sheet population does not have access to geosynchronous orbit.

### 3.4 Statistical Data Analysis

The particle data for the present study are taken from the comprehensive database of geosynchronous plasma observations made by the MPA instruments (see chapter 2). As previously discussed, the routine processing of MPA data includes the calculation of several moments of the particle distributions, as well as spin-averaged fluxes at each of the 40 energy levels for both electrons and ions. These data form the basis of the present work, which utilizes one year’s worth of data (1996) from three different satellites, corresponding to approximately one million data points with a time spacing of 86 s on each satellite.

The data are processed in the following way: The data points for each half hour of local time covered by one satellite on a given day are extracted from the database, and the median of the observed parameter is calculated. By calculating the median instead of the average value, outliers in the measurements are eliminated. (Calculations using the average value do not lead to significant differences in the statistics.) Magnetosheath and boundary layer intervals are excluded by accepting only measurements with a proton density of  $< 3 \text{ cm}^{-3}$  and a perpendicular proton temperature of  $> 2000 \text{ eV}$ . The half-hour median values are then sorted into bins according to local time and geomagnetic activity, represented by the  $Kp$  index. Finally, for each LT- $Kp$  bin, the average of all the median values is calculated.

The distribution of data points included in each  $Kp$  bin is equal to the  $Kp$  occurrence dis-

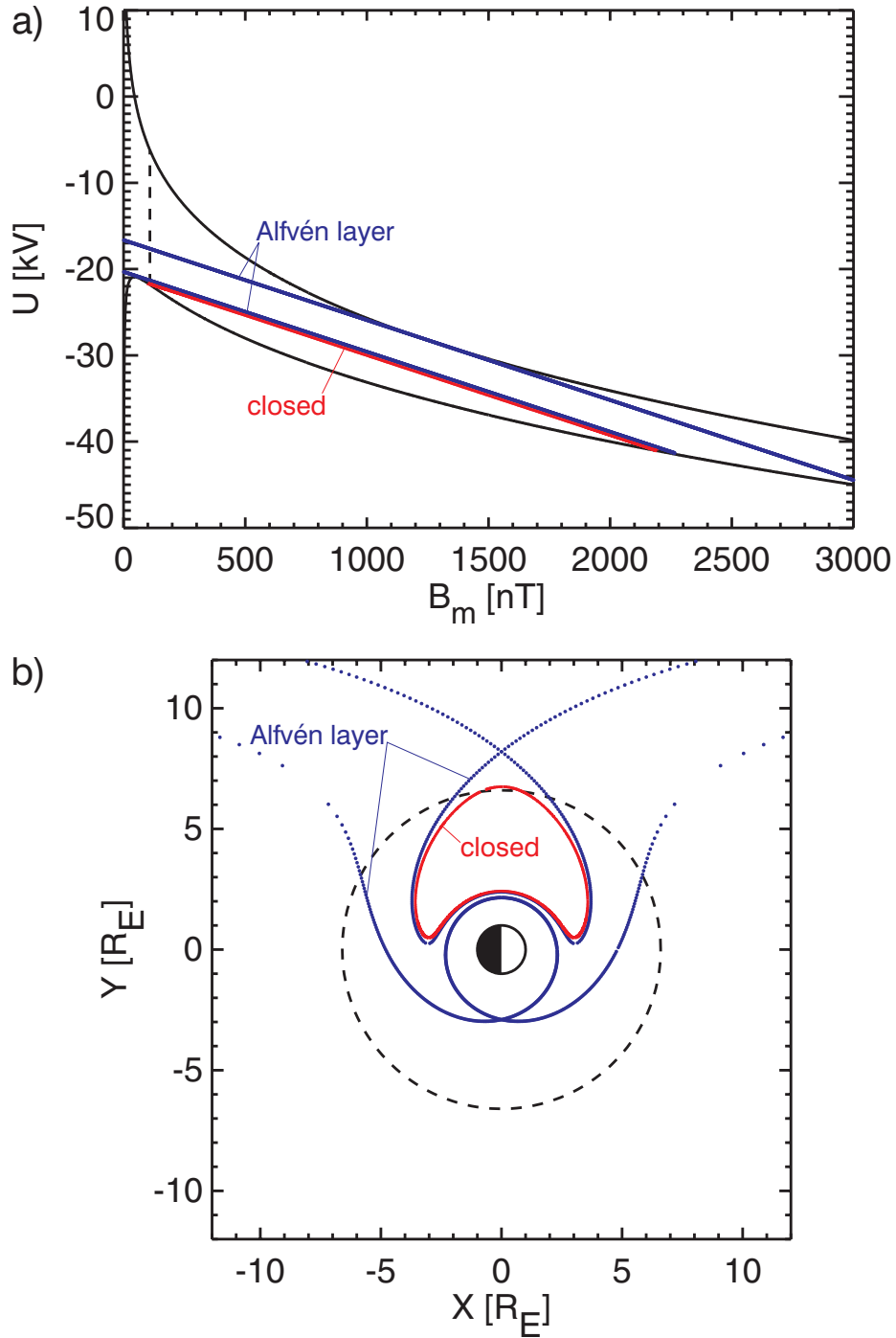


**Figure 3.2:** “Banana” orbits of 1-keV protons in (a)  $(U, B)$  and (b) Cartesian coordinates calculated from the Gussenhoven  $\gamma=1$  model for  $Kp=3$ .

### 3 Plasma Sheet Access to Geosynchronous Orbit

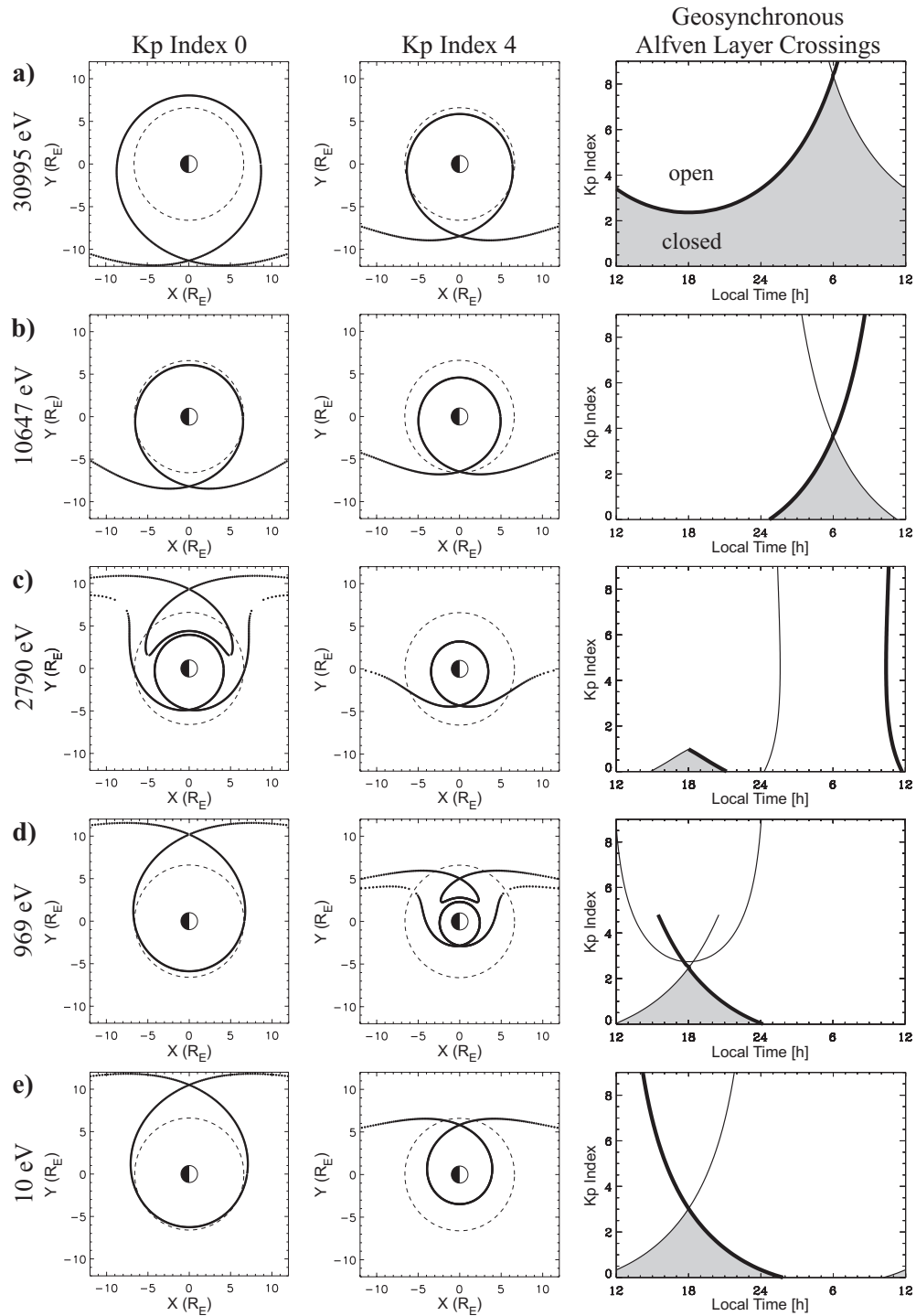


**Figure 3.3:** Open/closed drift separtrices for different energy protons, (a) 30,995 eV, (b) 10,647 eV, (c) 2,790 eV, (d) 969 eV, and (e) 10 eV, calculated assuming a cross-tail electric field that is parameterized by  $Kp$ , for  $Kp=$  (left) 0 and (middle) 4. (right) LT and  $Kp$  dependence of the geosynchronous crossings of the separatrices. The  $Kp$  dependence of the convection field strength is based on the Gussenhoven model for  $\gamma=2$ . Areas of closed drift paths are shaded at right.

### 3 Plasma Sheet Access to Geosynchronous Orbit

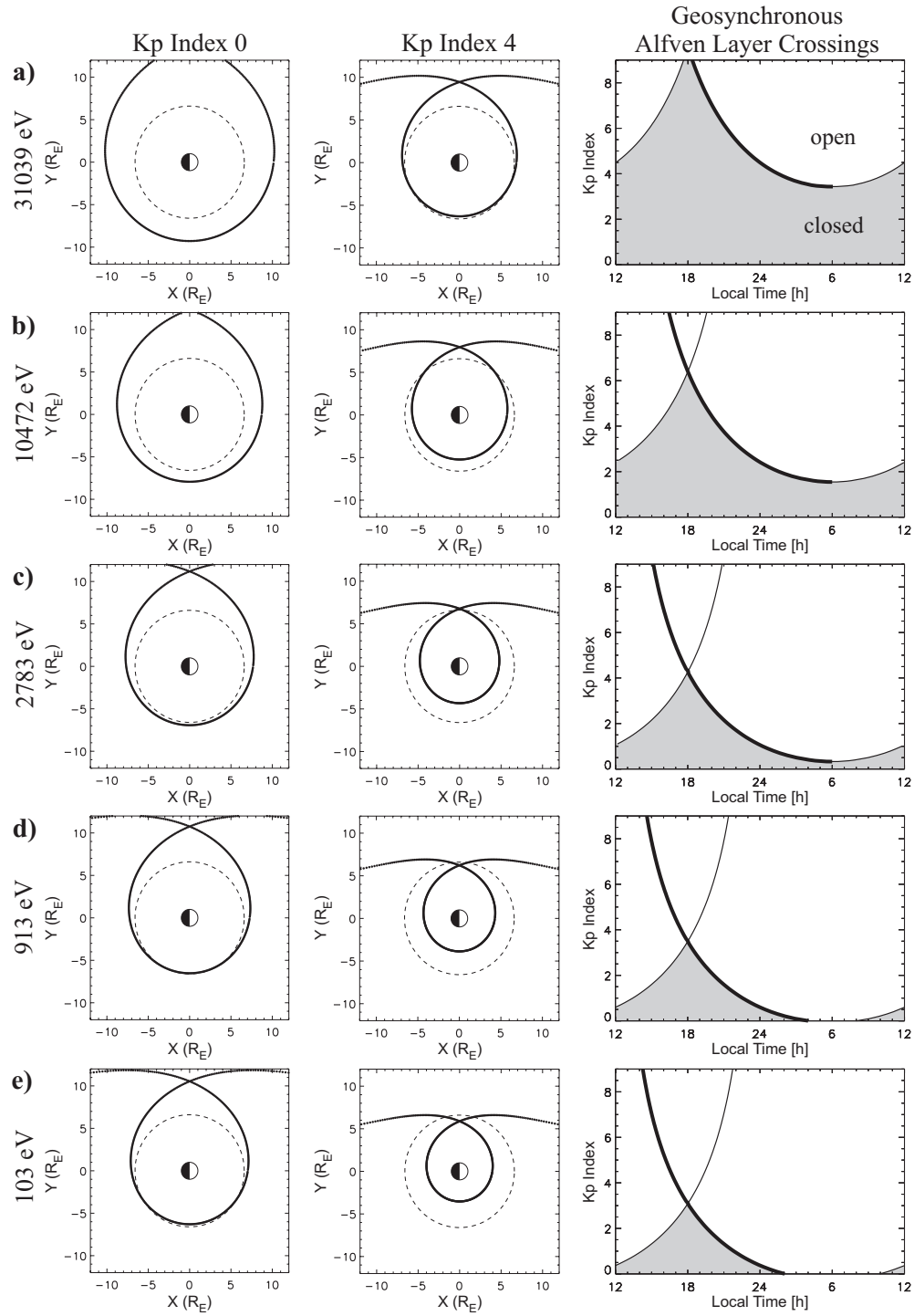


**Figure 3.4:** Open/closed drift separtrices for different energy electrons, (a) 31,039 eV, (b) 10,472 eV, (c) 2,783 eV, (d) 913 eV, and (e) 103 eV, calculated assuming a cross-tail electric field that is parameterized by  $Kp$ , for  $Kp =$  (left) 0 and (middle) 4. (right) LT and  $Kp$  dependence of the geosynchronous crossings of the separatrices. The  $Kp$  dependence of the convection field strength is based on the Gussenhoven model for  $\gamma = 2$ . Areas of closed drift paths are shaded at right.

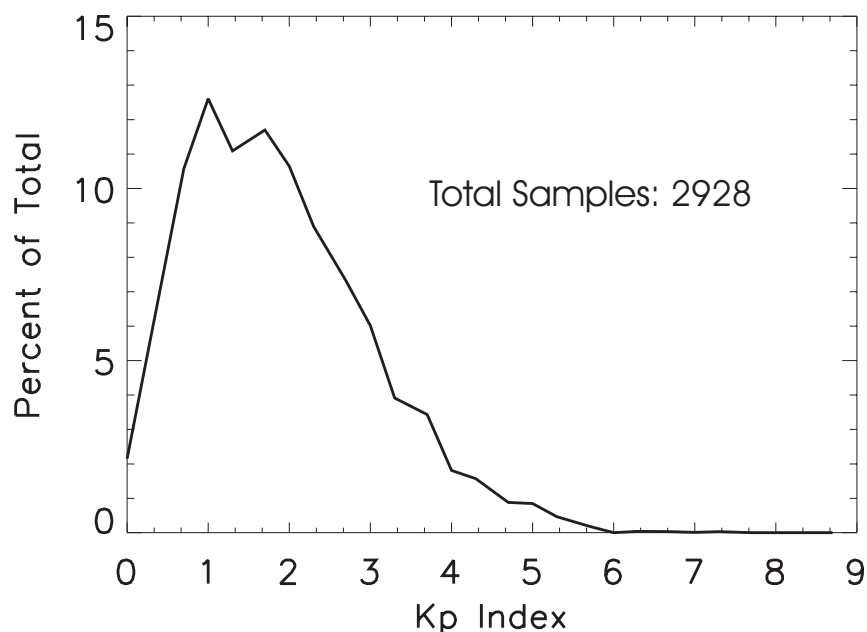


**Figure 3.5:** Occurrence frequency of  $Kp$  for 1996.

tribution shown in Figure 3.5. The distribution in LT for each  $Kp$  range was fairly uniform, so Figure 3.5 provides a good indication of the significance of the derived values in various  $Kp$  ranges. In general, the best statistical representation is achieved for the most common geomagnetic activity levels in the  $Kp$  range from 1– to 3. The better statistics in this activity range will be manifested as smoother transitions between the bins in the distributions presented below. Figure 3.5 also indicates that 1996 was a relatively low  $Kp$  year.

### 3.5 Observations

The results from the statistical analysis of spin-averaged proton and electron fluxes are displayed in a special form which can be understood with the help of an example shown in Figure 3.6 for the proton flux of the 30,995 eV channel. As mentioned in section 3.3 the geosynchronous Alfvén layer crossings at various geomagnetic activity levels (Figure 3.6a, adapted from Figure 3.3a, left and middle) can be transformed into a representation of the crossings as a function of local time and  $Kp$  (Figure 3.6b, adapted from Figure 3.3a, right). For easier differentiation between the open and closed drift trajectory regions, the closed regions are shaded. The curves in Figures 3.6a and 3.6b represent the Gussenhoven  $\gamma=2$  model.

In Figure 3.6c the LT/ $Kp$  locus of the Alfvén layer crossings from Figure 3.6b, as well as for the other convection models I have examined, is overlaid onto the LT/ $Kp$  distribution of average fluxes, compiled as described above. The fluxes are color coded according to the

### 3 Plasma Sheet Access to Geosynchronous Orbit

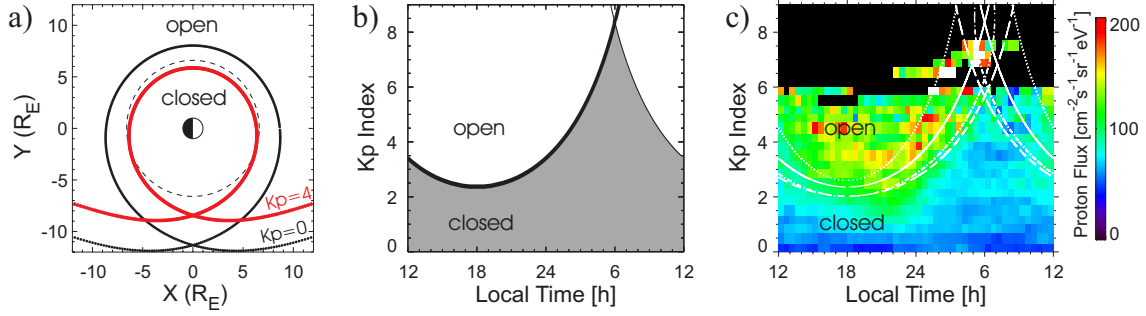


**Figure 3.6:** Illustration of drift-trajectory analysis of geosynchronous flux occurrence statistics for protons with an energy of 30,995 eV. (a) Open/closed drift separatrices in the equatorial plane for 30,995 eV protons for  $K_p=0$  and  $K_p=4$ . (b) Corresponding LT/ $K_p$  locus of the Alfvén layer crossings calculated by the Gussenhoven  $\gamma=2$  model. (c) Curves of the geosynchronous Alfvén layer crossings for different models, overlaid on the average fluxes measured in this energy channel. The dotted, solid, and dashed curves represent shielding factors  $\gamma=1,2,3$ , respectively, for the Gussenhoven model; the Maynard  $\gamma=2$  model is shown as a dash-dotted curve.

color bar shown next to the graph. The black regions indicate data unavailability, and white bins contain flux values exceeding the maximum of the corresponding color bar.

The average observed fluxes for various energies of protons and electrons are shown in Figures 3.7 and 3.8, respectively, in the same manner as illustrated in Figure 3.6c. The corresponding drift separatrices for each energy level, as well as the LT/ $K_p$  dependence of the geosynchronous Alfvén layer crossings, can be found in Figure 3.3 for the protons and Figure 3.4 for the electrons.

Distinct boundaries are evident in the fluxes displayed in Figures 3.7 and 3.8. Some of these boundaries appear to coincide with the calculated open-closed drift boundaries. The sections of the calculated curves that appear to correspond to apparent boundaries in the observed fluxes are marked as thick lines in Figures 3.3 and 3.4. The implications of these comparisons are now considered in more detail.

#### 3.5.1 Protons

In Figure 3.7a the proton fluxes for the high-energy channel (30,995 eV) are low at all local times for low  $K_p$  values. As shown in Figure 3.3, under low-activity conditions, geosynchronous orbit should lie entirely within the region of closed drift trajectories for particles of this energy and should thus be inaccessible to fresh plasma sheet material, consistent with the observed low fluxes. With rising geomagnetic activity the Alfvén layer moves closer and closer to the Earth, giving the plasma sheet access to geosynchronous orbit at an increasing range of local time centered at dusk. Consistent with this expectation, higher fluxes in this energy range are indeed observed at these local times, and the flux boundary is generally

### 3 Plasma Sheet Access to Geosynchronous Orbit

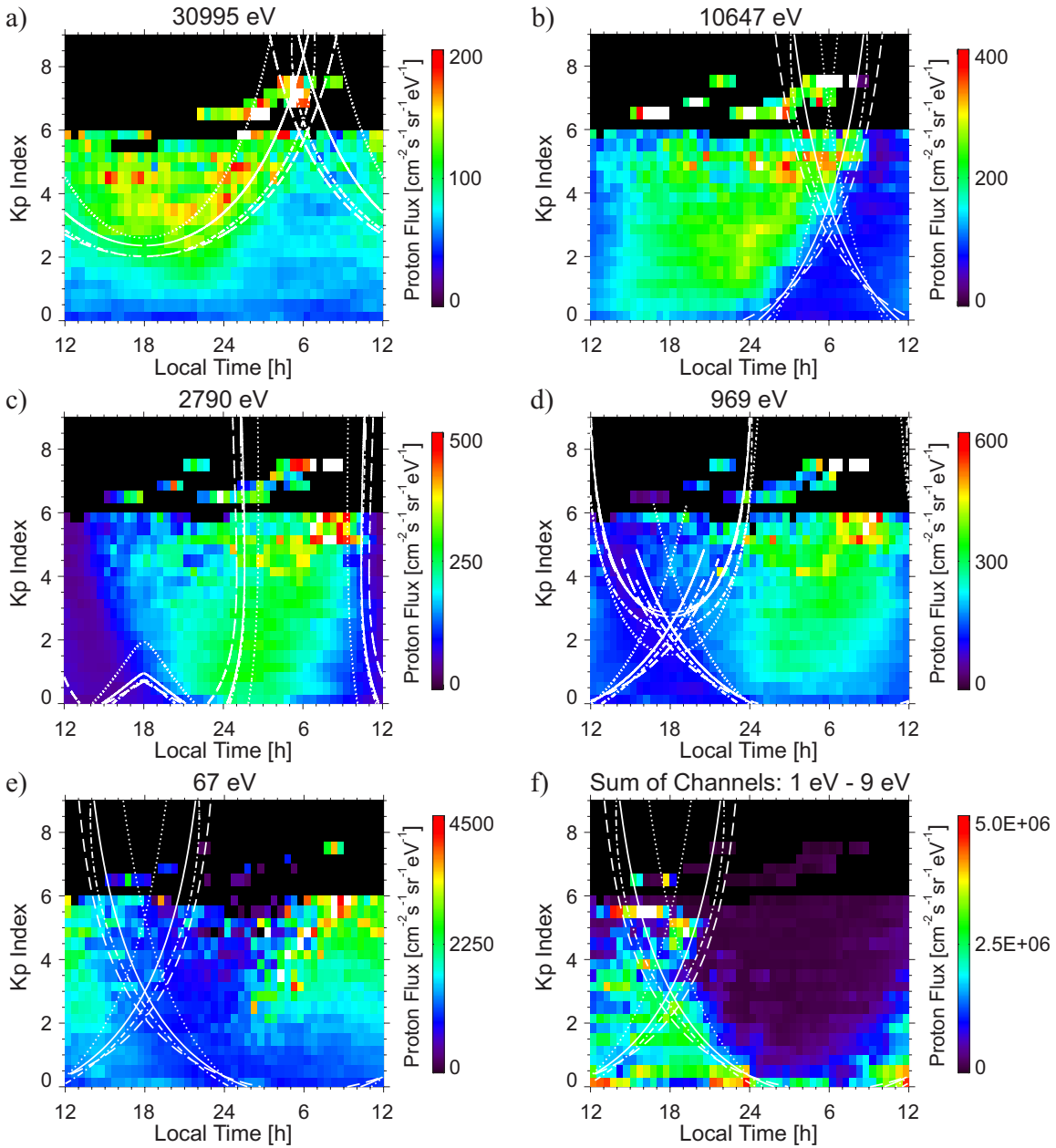


**Figure 3.7:** The 1996-averaged proton flux for six different energy channels, (a) 30,995 eV, (b) 10,647 eV, (c) 2,790 eV, (d) 969 eV, (e) 67 eV, and (f) sum of 1–9 eV, binned according to LT and  $Kp$ . Black indicates no data available, and white bins contain fluxes that exceed the corresponding maximum of the color bar. The overlaid curves represent the local times of geosynchronous Alfvén layer crossings as a function of the  $Kp$  index (see also Figure 3.3) for the Gussenhoven model (dotted curve,  $\gamma=1$ ; solid curve,  $\gamma=2$ ; dashed curve,  $\gamma=3$ ) and the Maynard model (dash-dotted curve,  $\gamma=2$ ).

### 3 Plasma Sheet Access to Geosynchronous Orbit

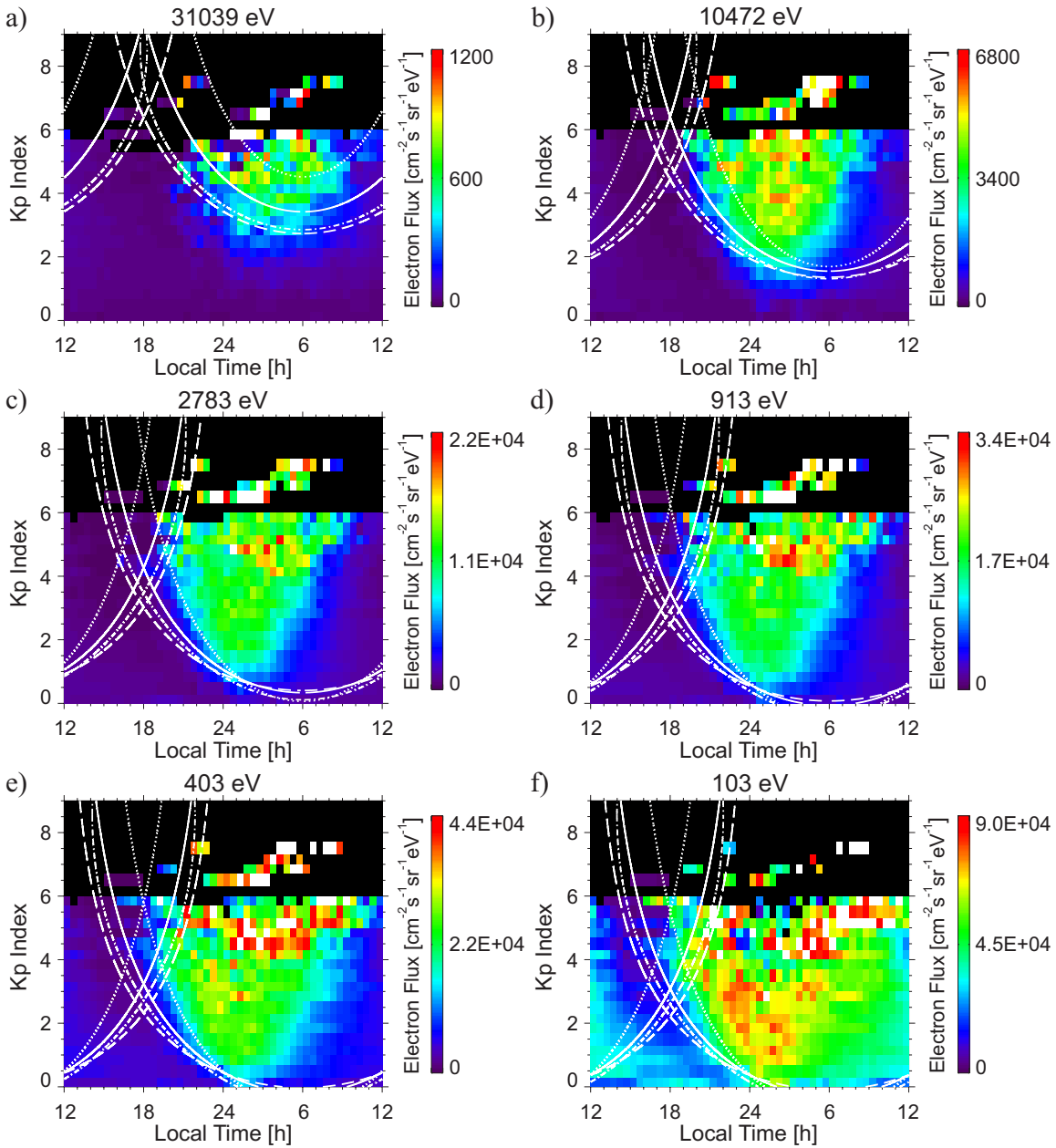


**Figure 3.8:** The 1996-averaged electron flux for six different energy channels, (a) 31,039 eV, (b) 10,472 eV, (c) 2,783 eV, (d) 913 eV, (e) 403 eV, and (f) 103 eV, binned according to LT and  $Kp$ . Black indicates no data available, and white bins contain fluxes that exceed the corresponding maximum of the color bar. The overlaid curves represent the local times of geosynchronous Alfvén layer crossings as a function of the  $Kp$  index (see also Figure 3.4) for the Gussenhoven model (dotted curve,  $\gamma=1$ ; solid curve,  $\gamma=2$ ; dashed curve,  $\gamma=3$ ) and the Maynard model (dash-dotted curve,  $\gamma=2$ ).



### 3 Plasma Sheet Access to Geosynchronous Orbit

---

well described by the calculated boundary between open and closed drift paths at most local times. The exception is a region before noon where the fluxes are substantially lower than in the open drift path region on the nightside. More will be said below about this apparent depletion, which was also noted by *McIlwain* [1972]. The models best representing the statistical flux distribution are the curves using the Gussenhoven  $\gamma=3$  method and the Maynard method.

For the next lower proton energy, 10,647 eV (Figure 3.7b), the models predict that open drift trajectories have access to geosynchronous orbit in the premidnight region at low  $Kp$  values. The observed flux boundary is in remarkably good correspondence with this expectation, showing a clear drop in the flux rate around midnight at the predicted transition from open to closed drift trajectories. Above a  $Kp$  of  $\sim 3$  the model predicts that geosynchronous orbit should lie on open drift trajectories at all local times. Thus one would expect to see plasma sheet flux levels at all local times. Instead, the flux rates at high  $Kp$  show the same drop at increasing local times as the ones at lower geomagnetic activity levels. This behavior can be interpreted, through reference to Figure 3.3, as evidence for the action of significant loss processes during the drift through the near-Earth region (see also *Maurice et al.* [1998] and *Kistler et al.* [1989]). The obvious flux boundary in Figure 3.7b clearly corresponds to the thick curve shown in Figure 3.3b (right). By comparison with Figure 3.3b (middle), it can be seen that this boundary separates drift trajectories that take a direct dawnside route from trajectories that follow the long, circuitous route around the duskside of the Earth. Plasma sheet ions taking the long route have a longer time to suffer losses and hence reach the prenoon sector with significantly lower fluxes. These loss processes themselves cannot be explained by the Alfvén layer model, but the transition between the open drift trajectory region of fresh proton plasma passing the Earth at dawn and the open drift trajectories of depleted protons moving clockwise around the Earth produces a clearly observed flux boundary. The depletion suffered by the protons is principally caused by atmospheric losses, charge exchange, and Coulomb collisions [e.g., *Kistler et al.*, 1989; *Fok et al.*, 1991; *Jordanova et al.*, 1996; *Kozyra et al.*, 1998a]. In the energy range of this study, charge exchange is the most important loss process for protons [*Fok et al.*, 1991; *Jordanova et al.*, 1996]. The observed boundary in Figure 3.7b appears to be best modeled using the Gussenhoven  $\gamma=2, 3$  and the Maynard methods.

At an ion energy of 2,790 eV the theoretical separatrices illustrated in Figure 3.3c become complicated, especially at lower  $Kp$ . Close inspection shows that there is, nonetheless, a good correspondence between the predicted boundaries and the flux observations shown in Figure 3.7c. In Figure 3.7c the region of closed banana orbits predicted near dusk at low  $Kp$  is clearly absent of significant fluxes. The clear boundary just before noon corresponds to the transition from paths that bring fresh plasma sheet material rather directly around the dawnside to the longer drift paths taken by plasma sheet ions coming around the duskside (see Figure 3.3). As discussed above, the flux drop at this boundary is again indicative of appreciable losses during the drift from the nightside. The predicted “boundary” near midnight does not correspond to any flux discontinuity (Figure 3.7c) because it is a boundary based on the future motion of the particles (whether they will go to dawn or dusk), rather than

### 3 Plasma Sheet Access to Geosynchronous Orbit

---

a boundary in the source properties. None of the convection models appears particularly superior for this energy range.

For protons of lower energies ( $\lesssim 1$  keV) the bulge of the closed orbit region is found at dusk instead of dawn (Figure 3.3d), consistent with the observed low proton fluxes at 969 eV in the evening sector at  $Kp < 3$  (Figure 3.7d). At higher  $Kp$ , when the Alfvén layer is completely earthward of geosynchronous orbit and banana orbits exist, a dark lane occupies the region between the two afternoon separatrices. From Figure 3.3d, it is apparent that this region corresponds to drift paths that are very circuitous and probably exposed to significant losses for a long time. At this energy the Gussenhoven  $\gamma=2$  method leads to the closest fit to the statistical boundary.

Temporarily postponing the discussion of Figure 3.7e, I first turn to Figure 3.7f, which shows the statistical distribution of proton fluxes between 1 and 10 eV. This flux distribution in this energy range is essentially a mirror image of the 30-keV channel: The closed drift trajectories have the high fluxes, while the open drift trajectories are essentially empty, at least on the nightside. This mirror image reflects the different sources of the low- and high-energy ion populations: The high-energy protons originate in the plasma sheet, whereas the cold particles originate in the ionosphere and are only able to achieve significant flux levels in the region where flux tubes can circulate many times around the Earth, i.e., the plasmasphere [e.g., *Nishida*, 1966]. The presence of significant cold-proton fluxes on presumably open drift trajectories in the afternoon sector is attributable to plasmaspheric drainage and plasmasphere refilling processes. Drainage occurs when a rapidly increasing convection electric field moves the zero-energy Alfvén layer closer to the Earth, so that dense, cold plasma that was previously on closed drift trajectories finds itself on open drift trajectories that drain to the magnetopause [e.g., *Chen and Grebowsky*, 1974; *Elphic et al.*, 1996, 1997; *Borovsky et al.*, 1998]. In addition, plasma sheet flux tubes that are originally empty of cold plasma are “refilled” (or, more properly, “filled”) with outflowing ionospheric material as they convect across the dayside magnetosphere [e.g., *Chappell*, 1972; *Thomsen et al.*, 1998; *Lawrence et al.*, 1999], which also leads to higher cold-proton fluxes in the afternoon sector. The shape of the evening flux boundary in Figure 3.7f is best approximated with the Gussenhoven  $\gamma=1$  method.

The statistical distribution of the 67 eV ions (Figure 3.7e) does not appear to be organized by any of the calculated open-closed drift boundaries, which raises the question of what may be the source of this population. The plasma sheet is usually too hot to be a good source at these energies. On the other hand, unlike the cold plasma, these particles do not seem to build up in the closed drift region, suggesting that ionospheric refilling processes are not the source. Rather, the source appears to be on open drift trajectories after midnight, particularly at higher activity. This population may be produced by auroral upflows, or it might represent the low-energy edge of a cooler dawnside plasma sheet. An analysis of the pitch angle distribution of these ions may help to discriminate between these possibilities.

### 3.5.2 Electrons

The electron flux statistics (Figure 3.8) are also consistent with the hypothesis that the particle flux boundaries depend on a global convection pattern, coupled with loss processes (in this case, precipitation rather than charge exchange).

The electron drift pattern is much simpler than the drift pattern of the protons since the sum of gradient and corotation drift always results in a counterclockwise motion of the electrons around the Earth. Thus the bulge of the electron Alfvén layers is always at dusk, and there are no banana-shaped drift orbits as there were for the lower-energy protons. For higher energies (e.g. 31,039 eV, Figure 3.4a), geosynchronous orbit should be completely embedded in the trapped orbit region for  $Kp$  values below  $\sim 3$ , leading to low electron fluxes of these energies at all local times, as seen in the statistics (Figure 3.8a). As the geomagnetic activity increases, the Alfvén layer moves closer to the Earth, exposing geosynchronous orbit to the plasma sheet for an increasingly wide local time interval centered at 0600 LT. For all electron energies the most distinct Alfvén layer crossing in Figure 3.8 is the transition from the trapped to open drift trajectories in the premidnight region. As the electrons move to the dayside, they precipitate rapidly into the ionosphere, causing the fluxes to decrease [e.g., *Thomsen et al.*, 1998]. By the time geosynchronous orbit enters the trapped orbit region on the dayside, the electron fluxes in the open drift trajectory region are so far depleted that the crossing is not detectable. This observed behavior is the same for lower-energy channels as well. The appropriate shielding exponent implied by the observations in Figure 3.8 seems to be energy dependent: While the statistical boundaries of higher-energy channels are best fit by the Gussenhoven  $\gamma=3$  model or the Maynard model, the Gussenhoven model with a smaller shielding exponent provides a better match at lower energies.

## 3.6 Discussion

### 3.6.1 Access

The observations show that the average plasma sheet access to geosynchronous orbit varies with local time,  $Kp$  index, and particle species and energy. Moreover, the shapes of the apparent observational boundaries of the differential fluxes in Figures 3.7 and 3.8 are consistent with the flux boundary curves calculated by a relatively simple electric field model. This leads to the conclusion that an electric field consisting of a superposition of a shielded cross-tail electric field and a corotation field is suitable for modeling average conditions at geosynchronous orbit. The boundaries between open and closed drift regions on the nightside are particularly clear. The agreement between observations and this model confirms that the  $Kp$  index provides an appropriate parameterization of the convection electric field.

On the dayside the model boundaries between open and closed drift trajectories are often invisible. Potentially, this could happen if the average convection changes on timescales shorter than the particle drift time. However, an analysis of the autocorrelation time of the  $Kp$  index, which is a measure of the persistence time of the geomagnetic activity, results in

### 3 Plasma Sheet Access to Geosynchronous Orbit

---

values of 33 hours or greater, depending on the year analyzed. This time is long compared to a typical drift time of  $\sim 12$  hours. Thus the flux measurements can be considered correctly binned, and the dayside view is just a time-lagged view of the nightside. More likely, the absence of discernible dayside boundaries is due to the fact that the fluxes have been greatly diminished by the time they reach this region. This strong depletion at essentially all energies supplies clear evidence for the operation of loss processes such as ion charge exchange and electron precipitation mentioned in section 3.5.

A definite determination of the shielding exponent for the convection electric field cannot be made from the results presented here because I have compared the statistics for spin-averaged fluxes with the predictions for  $90^\circ$  pitch angle particles. Preliminary calculations for  $K \neq 0$  particles suggest that, especially for the higher-energy channels, the model boundaries are very sensitive to the pitch angle. This may explain why the preferred shielding exponent appears to be energy dependent (Figures 3.7 and 3.8). Nevertheless, a shielding exponent of  $\sim 2$  appears to provide a suitable match to the observed boundaries. More precise statements concerning the shielding exponent could potentially be made using the data set with pitch angle resolved, but this is beyond the scope of this thesis.

The low-energy proton channels (Figures 3.7c–3.7e) and the low-energy electron channels (Figures 3.8e and 3.8f) show particularly high fluxes in the prenoon sector for higher geomagnetic activity levels. These high fluxes are not related to spacecraft charging since my analysis procedure specifically rejects fluxes that may be affected by charging.

#### 3.6.2 Applications

Besides the differential fluxes, the MPA database also contains various plasma parameters that are obtained from the fluxes through the moments calculations described in section 2.5. As mentioned in section 3.2, these bulk properties are often used as boundary conditions in ring current simulations. The density and temperature are calculated separately for the lower-energy channels from 1 to 100 eV and for the higher-energy range from 100 eV to 40 keV. The density and temperature statistics for the higher-energy populations of each species at geosynchronous orbit are shown in Figures 3.9a–3.9d in the same format as the flux plots in Figures 3.7 and 3.8. Because these bulk moments represent weighted sums of the different energy channels, the statistical distributions shown in Figure 3.9 can be readily understood by reference to the distributions shown in Figures 3.7 and 3.8 for the individual energy levels.

#### Density

On the nightside the density profiles (Figures 3.9a and 3.9b) represent the average access of plasma sheet material to geosynchronous orbit. For  $Kp$  values  $\lesssim 3$ , electron and proton density profiles peak near local midnight and decrease toward dawn and dusk. The electron density (Figure 3.9b) shows a rapid density decrease from midnight to dusk caused by lack of electron access to geosynchronous orbit (see Figure 3.8). The resulting dark lane on

### 3 Plasma Sheet Access to Geosynchronous Orbit

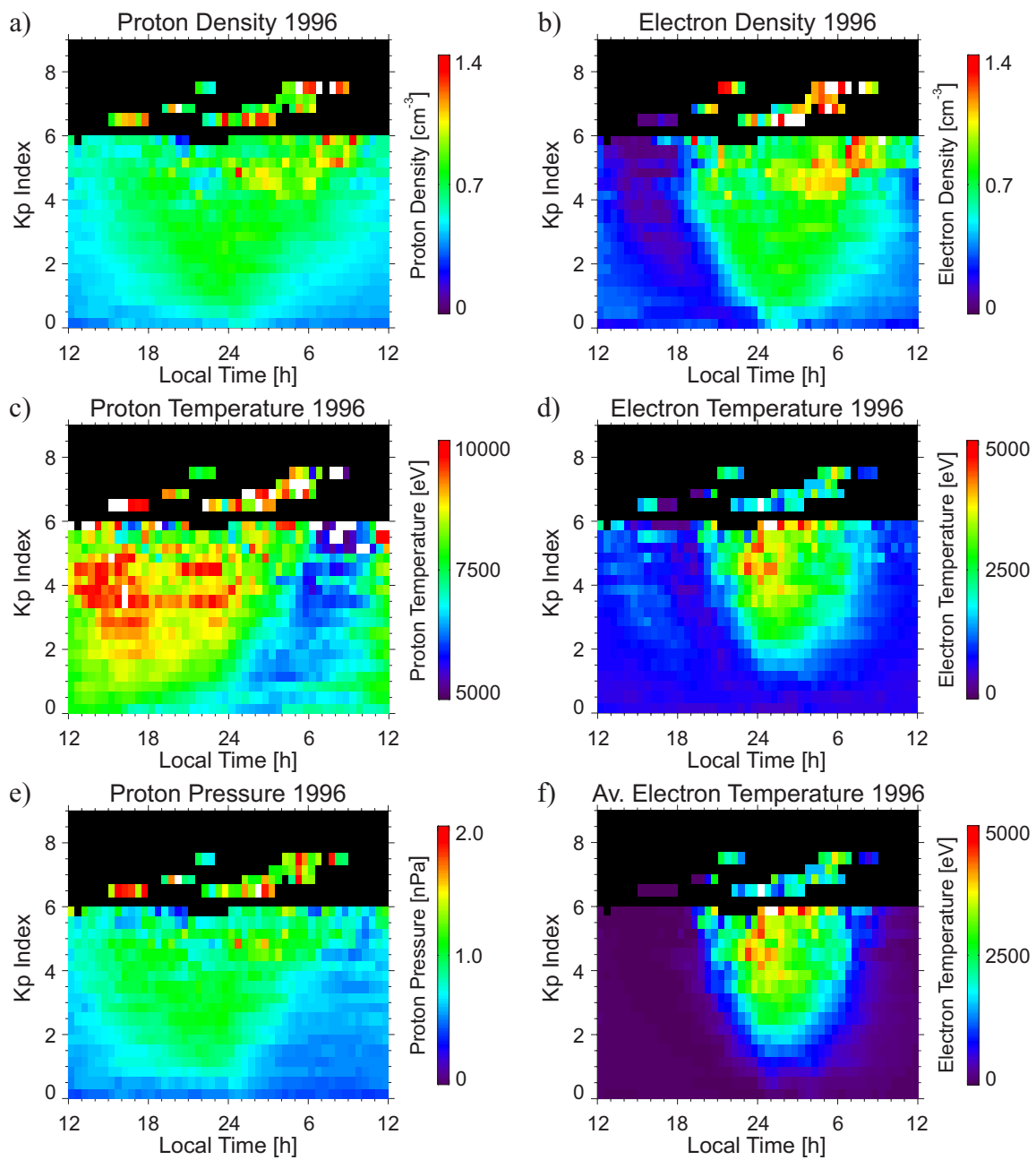


**Figure 3.9:** Geosynchronous bulk properties: (a) proton density, (b) electron density, (c) perpendicular proton temperature, (d) perpendicular electron temperature, (e) proton pressure, (f) average electron temperature.

### 3 Plasma Sheet Access to Geosynchronous Orbit

---

the evening side represents a region dominated by closed drift trajectories for electrons in the main plasma sheet energy range of a few hundred to a few thousand eV. The electron density decrease toward dawn can be explained by loss processes mainly due to electron precipitation.

For the protons the density distribution similarly reflects the flux distribution for the main plasma sheet ion energy range, approximately a few keV to a few tens of keV (compare Figures 3.7b and 3.7c). The decline in density from midnight toward dawn reflects the lack of dawnside access for plasma sheet ions of  $\sim 10$  keV, while the density decrease from midnight toward dusk is at least partly attributable to the exclusion of plasma sheet ions with energies  $\sim 1$  to a few keV. At higher values of  $Kp$  there is a persistent dawn-dusk asymmetry in the proton density that would not seem to be due to lack of access to plasma sheet trajectories. Rather, the asymmetry may be due to the fact that the ions take longer to drift to the duskside than the dawnside, with correspondingly greater losses. The further reductions in ion density toward noon are clearly evidence for such losses [Maurice *et al.*, 1998].

A further interesting aspect of the ion and electron density distributions in Figures 3.9a and 3.9b is the clear tendency to see higher densities at  $Kp \gtrsim 4$ , especially on the dawnside. These increases occur essentially across the entire primary plasma sheet energy range for both species (see Figures 3.7 and 3.8). I do not presently have an explanation for these enhanced densities. However, a study on the central plasma sheet by Wing and Newell [1998] reveals high proton densities along the dawnside low-latitude boundary layer. This high-density region moves closer to the Earth as the geomagnetic activity level increases. Drifting on the right trajectories, these particles could cause the geosynchronous density to be enhanced at dawn during these times, but the use of more sophisticated models for the magnetic and electric field will be necessary to pursue this question.

#### Temperature

While the density profiles show the average access of plasma sheet particles to geosynchronous orbit, the temperature profiles reflect primarily the accessibility of high-energy particles. The ion temperature profile shows a cool region at dawn, which is a region of trapped orbits for the higher-energy plasma sheet particles. Increasing  $Kp$  allows high-energy particles access to geosynchronous orbit over a broader local time range.

Similarly, in the electron temperature profile, the band of low temperatures in the dusk region identifies the LT range where only the lower-energy portion of the plasma sheet has access. The high-energy electrons can reach geosynchronous orbit only at  $Kp$  values  $\geq 2$ -, explaining the low electron temperatures over the entire orbit for small  $Kp$  values. At high  $Kp$  the high electron temperatures in the postmidnight region are due to the substorm injection and subsequent drift of energetic plasma sheet electrons.

The preceding discussion suggests that caution should be used in making comparisons of the geosynchronous density and temperature statistics with magnetotail values of these parameters: Since higher-energy plasma sheet particles cannot access geosynchronous orbit

### 3 Plasma Sheet Access to Geosynchronous Orbit

---

at low  $Kp$  values, the full plasma sheet population is not sampled there at such times. Furthermore, as noted above, the temperatures shown in Figure 3.9 have been calculated based on observed fluxes up to only  $\sim 40$  keV. They may thus underestimate the true temperature during times when particles at higher energies are present in abundance [e.g., *Birn et al.*, 1997]. This is primarily a problem for the ion population.

#### Proton pressure

Multiplication of the proton density and temperature measurements result in the proton pressure (Figure 3.9e). The pressure distribution is an indication of where currents are flowing, since the current density is related to the pressure gradient by  $j_{\perp} \approx (\underline{B} \times \nabla p)/B^2$ . Even though the proton density and temperature have significant azimuthal gradients on the nightside, the two quantities seem to balance each other, producing a more nearly uniform proton pressure across the nightside magnetosphere. This suggests that at geosynchronous orbit, radial currents in the equatorial plasma sheet are rather small.

#### Spacecraft charging

In a thick sheath approximation, where the Debye length is large compared to the spacecraft radius (which generally applies to geosynchronous satellites since for a typical plasma sheet density of  $n = 1 \text{ cm}^{-3}$  and an electron temperature of  $T_e \gtrsim 200 \text{ eV}$ , the Debye length is  $\lambda_D \gtrsim 100 \text{ m}$ ), the spacecraft surface potential relative to the ambient plasma is given by  $V \approx -\langle T_E \rangle$  [*Garrett and Rubin*, 1978; *Garrett*, 1981]. The average electron temperature  $\langle T_E \rangle$  can be calculated by combining the properties of low- and high-energy electrons:

$$\langle T_E \rangle = \frac{n_{le} T_{le} + n_{he} T_{he}}{n_{le} + n_{he}}, \quad (3.19)$$

where  $n_{le/he}$  and  $T_{le/he}$  are electron density and temperature for low energies (le) and high energies (he), respectively. As discussed by other authors [e.g., *McComas et al.*, 1993], the MPA instruments typically float somewhat negative relative to the ambient plasma. Hence low-energy ambient electrons are repelled from the spacecraft. Furthermore, because of differential surface charging effects, the low-energy electron measurements are also contaminated by trapped photoelectrons. Therefore, to estimate  $\langle T_E \rangle$ , the low-energy electron density  $n_{le}$  in (3.19) is replaced by the measured density of low-energy protons  $n_{lp}$ , under the assumption that the two densities are approximately equal. In addition, the temperature of the low-energy electrons  $T_{le}$  is estimated to be 5 eV. (The value chosen for  $T_{le}$  is of little importance for the outcome of the statistics.) The statistics of the resulting average electron temperature at geosynchronous orbit (Figure 3.9f) show high values on the nightside magnetosphere, especially between midnight and dawn, indicating the likelihood of significant surface charging for spacecraft moving through this region. A similar observation has been made by *McPherson et al.* [1975], who analyzed operational anomalies of several satellites, which occurred mainly between 2300 LT and 0600 LT. Those authors identified

### 3 Plasma Sheet Access to Geosynchronous Orbit

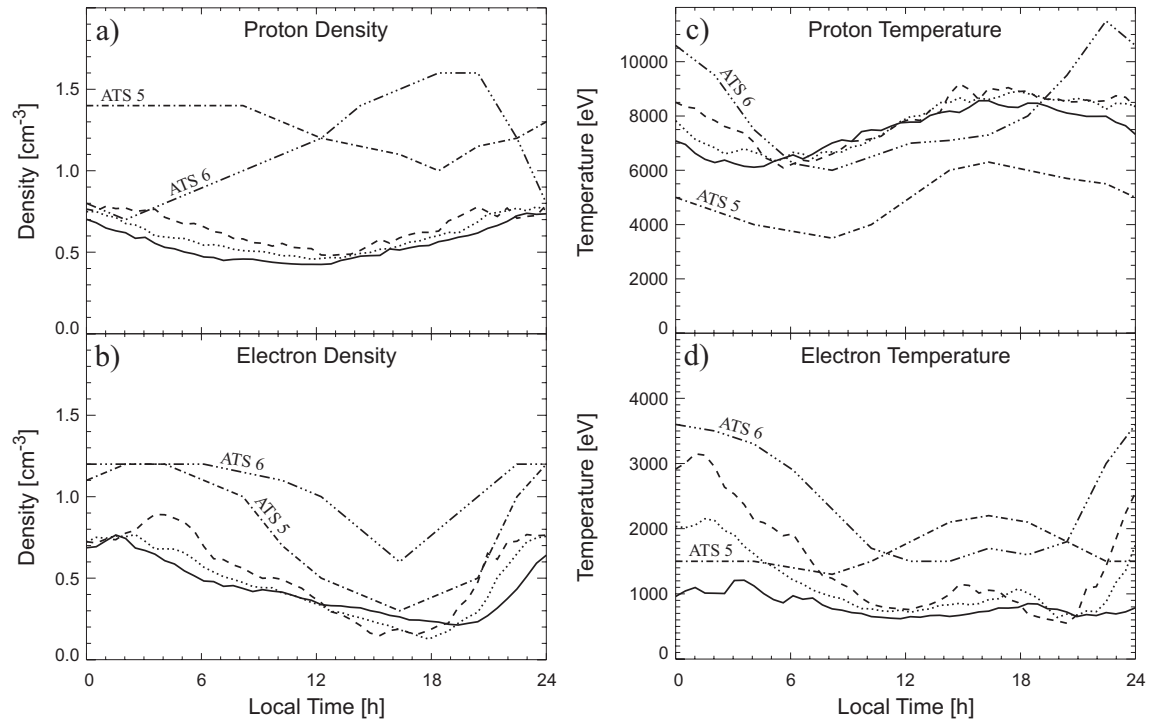


**Figure 3.10:** Comparison of (a) proton and (b) electron density and (c) proton and (d) electron temperature moments calculated from MPA with ATS 5 and 6 measurements. The MPA moments are shown for  $Kp$  values 1 (solid curve), 2 (dotted curve), and 3 (dashed curve). The ATS 5 and 6 measurements are plotted by dash-dotted curves and dash-dot-dot-dotted curves, respectively.

charge buildup through intense fluxes of energetic electrons associated with substorm injection events as the cause of the satellite operating anomalies. The statistics in Figure 3.9f also indicate a  $Kp$  dependence of the average electron temperature, as observed by *Garrett and Rubin* [1978]: the higher the geomagnetic activity level, the higher the average electron temperature found.

#### 3.6.3 Comparison With ATS Measurements

A previous analysis of the statistical properties of the geosynchronous plasma environment was reported by *Garrett et al.* [1981a,b] from ATS 5 and ATS 6 measurements. Among other things these authors examined the local time dependence of density and temperature at geosynchronous orbit. Their results are compared with the MPA statistics in Figure 3.10 for three  $Kp$  values approximately matching the most common values during the ATS measurements.

The local time dependence of the MPA and ATS 5 proton densities shows the same qualitative behavior, even though the absolute values differ about a factor of  $\sim 2$  (Figure 3.10a).



### 3 Plasma Sheet Access to Geosynchronous Orbit

---

This discrepancy may be due to differences in the energy ranges of the instruments and the method chosen for the moments calculation. The ATS 6 proton density curve differs vastly from the other measurements because it includes measurements that extend down to  $\sim 1$  eV, whereas ATS 5 extends down to 50 eV [Garrett *et al.*, 1981b] and the MPA (high-energy component) density includes only measurements above 100 eV. The MPA proton density shows only a very slight dependence on the geomagnetic activity level in the  $Kp$  range between 1 and 3, which is in agreement with analysis of the ATS data [cf. Garrett *et al.*, 1981b, Figure 3a].

The qualitative dependence of the MPA electron density on local time is in agreement with both the ATS 5 and ATS 6 measurements, although the absolute value is instrument dependent (Figure 3.10b). Furthermore, the independence of the MPA electron density on the  $Kp$  index in the range shown in the graph agrees with the results of the ATS study [cf. Garrett *et al.*, 1981a, Figure 4].

The ATS and MPA statistics also agree qualitatively with respect to the proton temperature (Figure 3.10c). The absolute values of the ATS 6 data seem to be closer to the MPA data, while the shape of the MPA proton temperature curve is closer to the ATS 5 data. The  $Kp$  dependence of the MPA data is negligible, just as shown by Garrett *et al.* [1981b].

The MPA curves for the electron temperature (Figure 3.10d) agree with the ATS 6 statistics, while the ATS 5 data contradict these results. The reason for this deviation suggested by Garrett *et al.* [1981a] is the more quiescent magnetosphere sampled by the ATS 5 satellite. However, my results do not show a dusk enhancement in  $T_e$  during quiet times, as indicated by the ATS 5 measurements. Rather, the primary  $Kp$  effect on the geosynchronous electron temperature distribution appears from my results to be an increase in the average nightside temperature with increasing activity.

## 3.7 Summary

Using one year's worth of Magnetospheric Plasma Analyzer data from three Los Alamos geosynchronous satellites, a statistical study has been made of the LT and  $Kp$  dependence of proton and electron fluxes at geosynchronous orbit. Displayed as a function of the two independent parameters LT and  $Kp$ , the fluxes show distinct boundaries that result from a global magnetospheric particle drift process combined with losses due to charge exchange of the ions and auroral precipitation of the electrons. The observational boundaries have been compared with theoretical positions of separatrices between open and closed drift trajectories calculated by a Hamiltonian energy conservation approach. Using a coordinate transformation from Cartesian space to the  $(U, B, K)$  space, the position of the Alfvén layers as a function of particle species, energy, local time, and geomagnetic activity level can be obtained easily. The result confirms the predictions of plasma sheet access to the geosynchronous region. The statistical distributions presented here have numerous potential practical applications, such as providing appropriate initial or boundary conditions for simulations of ring current evolution.

### 3 Plasma Sheet Access to Geosynchronous Orbit

---

Selected plasma bulk properties such as the density, temperature, proton pressure, and the average electron temperature, which are obtained from the fluxes, were also statistically evaluated. The shape of the resulting moments distributions can be explained by the access pattern combined with loss processes as discussed for the fluxes. The distribution of the average electron temperature, which is a proxy for spacecraft charging, shows high values in the postmidnight region. The average electron temperature also tends to increase with higher geomagnetic activity.

Furthermore, the statistics of the bulk properties have been compared to a previous statistical analysis of the geosynchronous plasma environment by *Garrett et al.* [1981a,b] from ATS 5 and ATS 6 measurements. Even though the absolute values of the plasma properties determined from the two data sets differ from each other because of the different energy ranges used in the ATS calculations, the qualitative dependences of MPA and ATS 5 and 6 measured plasma properties on local time are in agreement with each other.

# 4 Generalization to Numerical Global Field Models

## 4.1 Overview

The previous statistical analysis of the geosynchronous particle environment in chapter 3 showed that the particle fluxes are well organized by local time and the geomagnetic activity as measured by the  $Kp$  index. Regions of high and low fluxes at geosynchronous orbit are separated from each other by distinct boundaries, approximately matching the Alfvén boundary crossings of the geosynchronous satellites calculated analytically from a Volland-Stern electric potential and a dipole magnetic field. Expanding the analysis technique from the previous work to arbitrary, numerical electric and magnetic field models, I reevaluate the Alfvén boundary crossings using several available global electric potential models and considering external magnetic field contributions. The more sophisticated numerical models do not do a better job of explaining the observed average access of plasma sheet material to the geosynchronous region than does the simple analytical model.

## 4.2 Introduction

As discussed elaborately in the previous chapter, the distributions of electric and magnetic fields in the terrestrial magnetosphere organize the particle drift trajectories into two classes. Near the Earth where the corotation field dominates there is a class of closed drift trajectories. At larger distances from the Earth, drift trajectories are open, and fresh plasma sheet material may be transported from the geomagnetic tail toward and around the Earth. Thus, at a given location in the inner magnetosphere, high particle fluxes in the plasma sheet energy range are associated with open drift trajectories, while low fluxes are associated with closed trajectories. The open and closed regions are separated from each other by the Alfvén layer. The statistical survey of the geosynchronous particle fluxes in chapter 3 shows distinct boundaries, the location of which depends on the particle species and magnetic moment, as well as the geomagnetic activity level and local time. The statistical boundaries can be interpreted as Alfvén layer locations at geosynchronous orbit separating open and closed regions. Thus they ultimately give valuable information about the delivery of plasma sheet material from the magnetotail to the near-Earth region in a statistical sense,

## 4 Generalization to Numerical Global Field Models

---

an important aspect in predicting space weather. The previous work of chapter 3 compared the observed flux boundaries to geosynchronous Alfvén layer crossings, as predicted by a Volland-Stern electric potential and a dipole magnetic field. Even though time variability of the geomagnetic activity is believed to play a considerable role in the transport process, the study showed a surprisingly good match between observed and theoretical boundaries. The Volland-Stern and dipole models are very simple. Nowadays, much more sophisticated models exist, and the question arises of whether these models can improve the drift picture in the inner magnetosphere and do even better at reproducing the statistical boundaries. This issue will be addressed in this chapter.

### 4.3 Models

#### 4.3.1 Alfvén Layer Model

The Volland-Stern and dipole model used in chapter 3 are given in the form of analytical expressions, leading to a likewise analytical description of the Alfvén boundaries. Here I generalize to nonanalytical, semiempirical models, which requires a modified approach for obtaining the theoretical boundaries. Using the  $(U, B, K)$  formalism, the boundary locations can be easily obtained, as shown in section 3.3 and references therein. Describing particle locations in terms of the electric potential  $U$ , the magnitude of the magnetic field at the mirror point  $B$ , and the modified second adiabatic invariant  $K$  leads to drift trajectories and Alfvén layers that can be represented by straight lines. Assuming equatorially mirroring particles ( $K = 0$ ), the  $K$  coordinate may be omitted, and all particle locations can be described by  $(U, B)$  coordinate pairs. The space of valid combinations of  $U$  and  $B$  is limited by two separators, also called terminators in this thesis (see Figure 4.1). The Cartesian locus of the separators is given by the extrema of the magnetic field on the equipotentials of the electric field as illustrated by Figure 4.2. Figure 4.2 shows a two-dimensional projection of the  $\underline{B} \cdot \nabla B = 0$  surface, also referred to as the “bounce center surface” [cf. *Vogt and Glassmeier, 2000*], with schematic isocontours of  $B$  represented by dashed circles and a selected equipotential of the electric field drawn as a solid line. For a dipole magnetic field the bounce center surface coincides with the equatorial plane. A coordinate system is defined locally along the path of the electric equipotential contour with  $s$  pointing in the direction  $dU = 0$  and a  $\rho$  direction perpendicular to  $s$ . In this coordinate system the gradient of the electric potential of  $U$  can be written as

$$\nabla U = \frac{\partial U}{\partial s} \underline{\hat{s}} + \frac{\partial U}{\partial \rho} \underline{\hat{\rho}}, \quad (4.1)$$

where  $\partial U / \partial s = 0$  per definition. The gradient of the magnetic field along the contour of constant  $U$  can also be expressed in this coordinate system:

$$\nabla B = \frac{\partial B}{\partial s} \underline{\hat{s}} + \frac{\partial B}{\partial \rho} \underline{\hat{\rho}}. \quad (4.2)$$

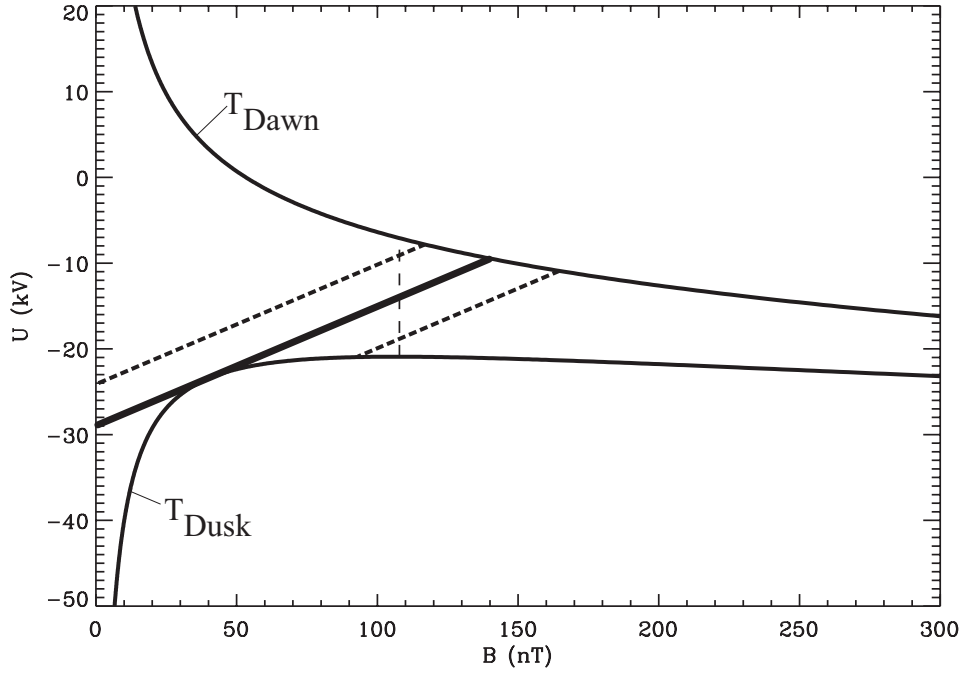


**Figure 4.1:** Example scenario for the  $(U, B)$  coordinate system. The separators, labeled  $T_{\text{Dawn}}$  and  $T_{\text{Dusk}}$ , are calculated for the Volland-Stern and dipole model combination using a shielding factor of  $\gamma=2$  and a geomagnetic activity level of  $Kp=3$ . Geosynchronous orbit is shown as a dashed vertical line at a magnetic field magnitude of  $\sim 100$  nT. The dotted lines show examples for open and closed drift trajectories of 15-keV electrons. Particle trajectories extending to low magnetic field values near the  $U$  axis have their origin in the far magnetotail and can be considered open. Drift trajectories connected to the terminators at both ends perform cyclic orbits between the separators and are thus closed. The Alfvén layer separating the two regions is shown as a thick solid line.

The term  $\partial B/\partial s$  in (4.2) becomes zero when the magnetic field reaches an extremum on the electric equipotential, causing  $\nabla B$  to point solely in the  $\rho$  direction. Since the gradients of  $U$  and  $B$ , which are oriented perpendicular to their respective isocontours, are parallel in this case, the  $U$  and  $B$  isocontours must be parallel as well. Thus the contours of constant  $U$  and  $B$  are tangent at the location of an extremum which can be written as

$$(\nabla U \times \nabla B) \cdot \hat{\underline{e}}_z = 0, \quad (4.3)$$

where  $\hat{\underline{e}}_z$  is the unit vector perpendicular to the bounce center surface. The equation used in this study to evaluate numerically the terminator location for arbitrary models for the electric potential and the magnetic field is given through (4.3) as

$$\frac{\partial U}{\partial r} \frac{\partial B}{\partial \phi} - \frac{\partial U}{\partial \phi} \frac{\partial B}{\partial r} = 0, \quad (4.4)$$

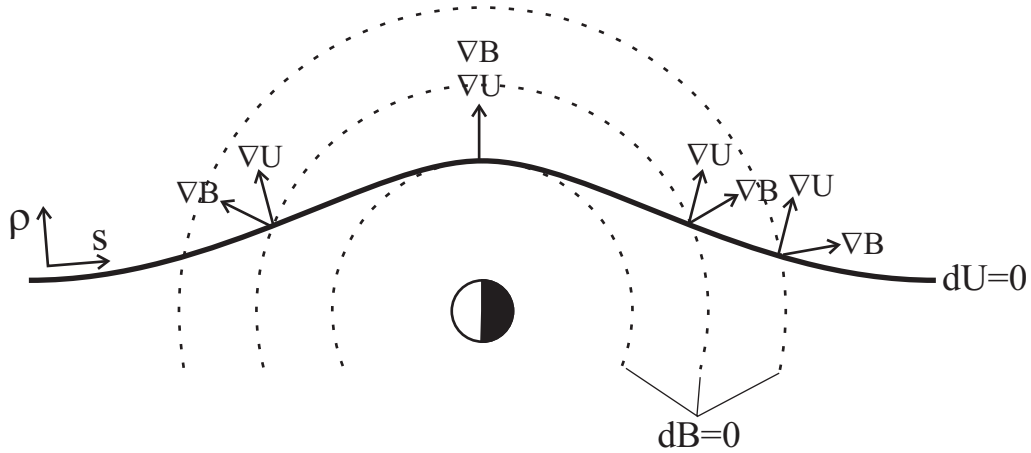


**Figure 4.2:** Relationship between gradients and isocontours in the bounce center surface. The dashed lines are isocontours of a dipolar magnetic field while the solid line represents an equipotential of the electric field. The terminators consist of loci where the magnetic field reaches an extremum on the isocontour of the electric potential. For these points the gradients of  $U$  and  $B$  are parallel.

where  $r$  and  $\varphi$  are geocentric distance and magnetic local time, respectively. Equation (4.4) is applied to two-dimensional grids of  $U$  and  $B$  with an extension of  $20 R_E$  from the Earth's center and a step size of  $0.1 R_E$ . The magnitude of the magnetic field assigned to each grid point is the minimum value on the field line containing the grid location. The corresponding electric potentials are also obtained through a field line mapping process to the surface (i.e., the ionosphere), where the potential structure is defined for a number of the convection models that will be considered. In this mapping, the field lines are assumed to be equipotentials of the electric field.

For a dipole magnetic field the bounce center surface coincides with the analysis plane. Furthermore, the Volland-Stern electric potential is directly defined for the grid, making the mapping process unnecessary. Because of the symmetry of  $U$  and  $B$ , the separator is simply given by the dawn-dusk meridian as shown in Figure 4.3. The field models by *McIlwain* [1972, 1986] described in section 4.3.2 are also defined in the equatorial plane. In this case the terminators are more complicated because of the models' asymmetry.

Using (4.4), the terminators for arbitrary models can be determined numerically. The Alfvén boundary can be interpreted as the last open drift trajectory, and, in principle, it is given by the straight-line trajectory that is tangent to the terminator curves (see Figure 4.1). However, numerical problems make this approach less successful for generalized electric and magnetic fields. Instead, for the present study, drifts are followed from numerous locations on geosynchronous orbit to see whether a location lies in the open or closed region. In this process each drift trajectory is traced in direction of decreasing  $B$  to the low magnetic field region. If a particle can escape to a threshold magnetic field of 10 nT without crossing a terminator, it is reasonable to assume the location to be in the open region. If, on the

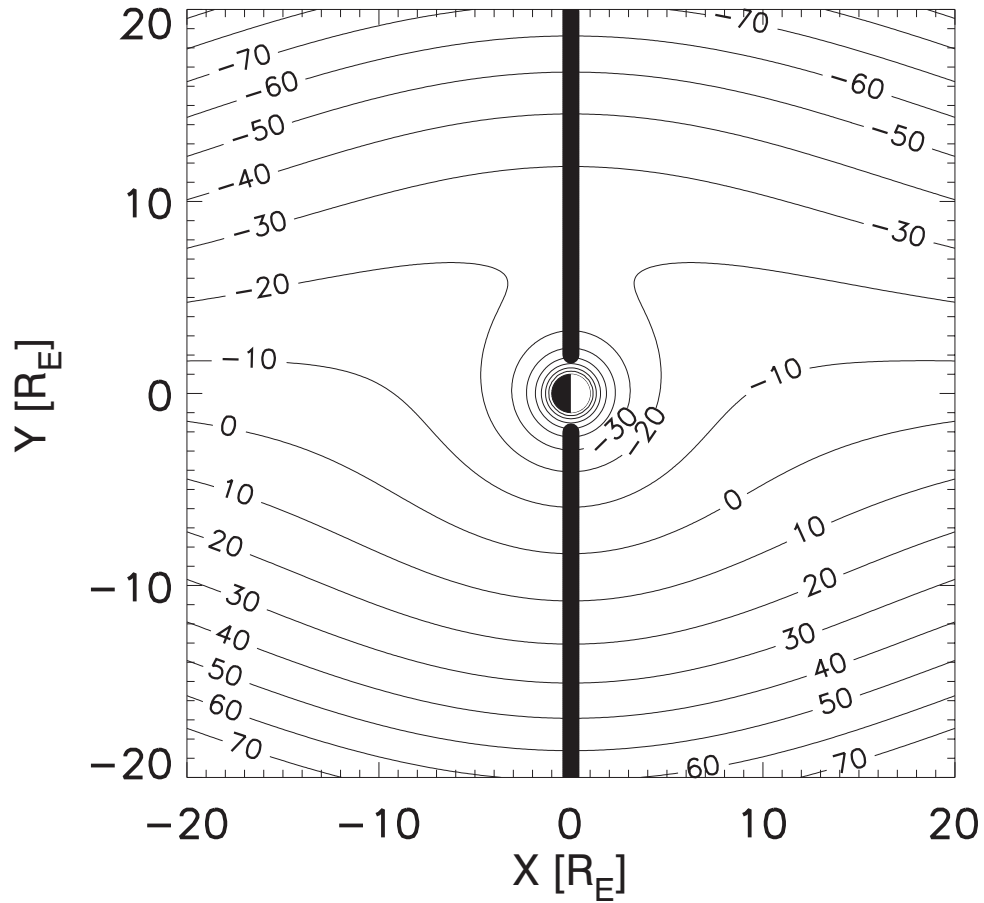


**Figure 4.3:** The separator calculated from a Volland-Stern electric potential and a dipole magnetic field in the bounce center surface is given by the dawn-dusk meridian, represented by a thick solid line. The electric potential contours, depicted by thin solid lines, are computed for a shielding factor of  $\gamma=2$  and  $Kp=3$ . The potential values are given in units of kV. The circular isocontours of the magnetic field are omitted.

## 4 Generalization to Numerical Global Field Models

---

other hand, a separator crossing exists, the corresponding location at geosynchronous orbit is located in the closed region. A numerical root finder is used to detect the crossings.

### 4.3.2 Field Models

The statistical flux observations in chapter 3 are organized by local time and  $Kp$ . In order to be able to test the field models, dependence on equal parameters is required. For some of the models, drivers other than  $Kp$  are used to vary the model. Thus relationships between those parameters and  $Kp$  need to be sought, so that  $Kp$  may be used as a proxy.

The magnetic field at geosynchronous orbit is dominated by the Earth's internal magnetic field. Hence the Alfvén layer calculations depend mainly on the choice for the internal field model rather than external contributions. Unless otherwise stated, a tilted dipole is chosen to represent the Earth's internal field component and the Tsyganenko 89c model for the field contributions from the ring current, the magnetotail current system, and the magnetopause currents [Tsyganenko, 1989]. Higher-order contributions of the Earth's internal field did not lead to significant differences in the boundary locations and are therefore ignored. The Tsyganenko 89c external magnetic field model is controlled by  $Kp$  and the Earth's tilt angle.

A variety of electric potential models have been developed in the past. In this study, selected models by McIlwain [1986], Heppner and Maynard [1987], Sojka *et al.* [1986], and Weimer [1995, 1996] are considered for comparison to results acquired from the analytical Volland-Stern model. The selection criterion for the models was primarily availability. Some of the models were originally developed to describe high-latitude ionospheric convection and may not accurately describe convection at lower latitudes corresponding to the near-Earth (i.e., geosynchronous) equatorial magnetosphere. Furthermore, the entire plasma sheet maps to a very narrow latitudinal band in the ionosphere [e.g., Pulkkinen *et al.*, 1992]. Hence only small parts of the ionospheric potential models are used in my study. Nevertheless, these models are often used for studies involving particle transport in the inner magnetosphere by various authors [e.g., Ober *et al.*, 1997; Toivanen, 1997; Whipple *et al.*, 1998; Quinn *et al.*, 1999; Hilmer and Ginet, 2000; Kistler and Larson, 2000], and an exploration of their utility in this region is warranted.

With the exception of the McIlwain E5D model, all the above mentioned (semi)empirical models provide the potential pattern in the ionosphere, requiring field line mapping to identify  $U$  on the grid. These models only consider the electric potential due to the convection electric field. The corotational contribution is not included and needs to be calculated separately. This is done by integrating the electric field induced by plasma corotating in an aligned magnetic dipole from the pole to the appropriate latitude. More accurate potential values could be obtained by taking the dipole tilt into consideration. In this study I neglect the inductive electric fields associated with the rocking of the dipole.

The global electric field model E5D was derived by McIlwain from drift-time dispersion of impulsively injected energetic particles measured by the ATS 5 satellite at geosynchronous orbit. The E5D model is more sophisticated than the one developed by Volland and



## 4 Generalization to Numerical Global Field Models

---

Stern, yet it is still analytical. It is also the only model considered in this work that provides the electric potential in the equatorial plane. The model will be used in combination with the M2 magnetic field model [McIlwain, 1972], which describes the magnetic field in the neutral sheet in reasonably good agreement with quiet-time geosynchronous observations [Cummings *et al.*, 1971].

The Heppner-Maynard-Rich model was developed from empirical patterns of the ionospheric convection electric field, hand-drawn by Heppner and Maynard [1987], which were subsequently digitized and fitted to spherical harmonics by Rich [Rich and Maynard, 1989]. Under southward IMF conditions a  $Kp$  parameterization for the model is given for three distinct states of the IMF  $B_y$  component, designated A, BC, and DE [Heppner and Maynard, 1987; Rich and Maynard, 1989]. Results shown in this chapter refer to mode A, but modes BC and DE provide similar results.

The ionospheric electric potential model of Sojka is a mathematical model that also includes previously found empirical observations. The input variables are  $Kp$  and the IMF components  $B_y$  and  $B_z$ . According to the authors of the model, the electric field has been found to correlate significantly with  $B_y$  only in the polar cap. Fortunately, the electric potential in this region is irrelevant for my application, because the field lines mapping from this part of the ionosphere are open and do not participate in the convection in the near-Earth equatorial region. The  $B_z$  component of the interplanetary magnetic field only influences the model under northward IMF conditions. Since the geomagnetic activity level is driven by the strength of the southward IMF,  $B_z$  only influences the Sojka electric convection patterns during geomagnetically quiet intervals which are concentrated at the lower end of the  $Kp$  scale. Thus, for the present analysis the overall model dependencies can be reduced to the geomagnetic activity level expressed by the  $Kp$  index.

The Weimer electric potential model is based on DE<sup>1</sup> 2 electric field measurements binned by IMF conditions as observed by ISEE<sup>2</sup> 3 or IMP<sup>3</sup> 8. Coverage for the entire high-latitude ionosphere is achieved by spherical harmonic least error fits of the satellite measurements. The model depends on the dipole tilt angle, the solar wind velocity, and the IMF components  $B_y$  and  $B_z$ . Unlike the Sojka model, the parameters of the Weimer model cannot be reduced to  $Kp$ . Instead, functional relations between  $Kp$  and the solar wind parameters were found by least squares fits from a large body of solar wind measurements retrieved from the National Space Science Data Center (NSSDC) OMNIWeb database<sup>4</sup>. Figures 4.4–4.6 show the correlations of the solar wind speed, IMF magnitude, and southward angle of the IMF with  $Kp$ . The functions obtained can only be understood as rough estimates since the spread of the measurements at each  $Kp$  level is rather large.

The linear correlation coefficients of the three dependencies are 0.24, 0.40, and 0.61, respectively. These values are fairly high, considering that the number of observations in the

---

<sup>1</sup>Dynamics Explorer.

<sup>2</sup>International Sun-Earth Explorer.

<sup>3</sup>Interplanetary Monitoring Platform.

<sup>4</sup>Database of near-Earth solar wind magnetic field and plasma data, energetic proton fluxes, and geomagnetic and solar activity indices. It is currently located on the Internet at <http://nssdc.gsfc.nasa.gov/omniweb/>.

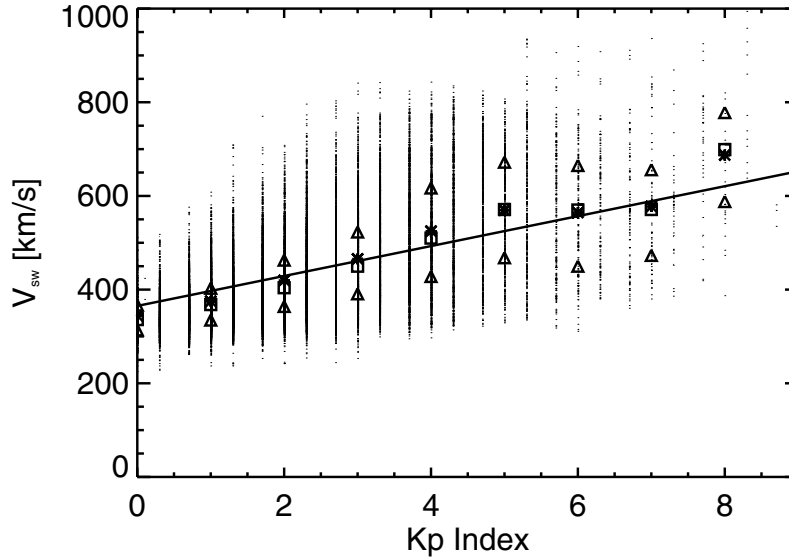


**Figure 4.4:** Relationship between hourly averaged solar wind flow speed, taken from the National Space Science Data Center (NSSDC) OMNIWeb database, and  $Kp$ . Average and median values for each  $Kp$  level are represented by asterisks and squares, respectively. The triangles reflect the 25th and 75th percentiles which are an indicator for the variation of the measurements. The solid line shows the least squares fit of the averaged values, which yields the approximate linear relation between flow speed and  $Kp$  of  $v_{sw} = 365 + 32 Kp$ .

OMNI data set used for this study is nearly 80,000. The probability of a random, uncorrelated data set showing correlation coefficients of this magnitude is virtually zero. However, the uncertainty of the functional dependence between the solar wind parameters and  $Kp$  is an additional source of error, and the results obtained with the Weimer model have to be evaluated with care.

### 4.4 Model Comparison

The results of the statistical analysis of spin-averaged electron and proton fluxes from chapter 3 are reproduced in Figures 4.7 and 4.8, respectively. Flux values are displayed color-coded as a function of local time and the  $Kp$  index, where black regions indicate data unavailability, and white bins contain flux values exceeding the maximum of the corresponding color bar. The energy channels selected correspond to  $\sim 30$ , 10, 3, and 1 keV, covering a broad spectrum of plasma sheet energies measured by the Los Alamos MPA instrument (see chapter 2). The white lines show the analytically determined geosynchronous Alfvén boundary crossings from the previous work, which correspond to a dipole magnetic field

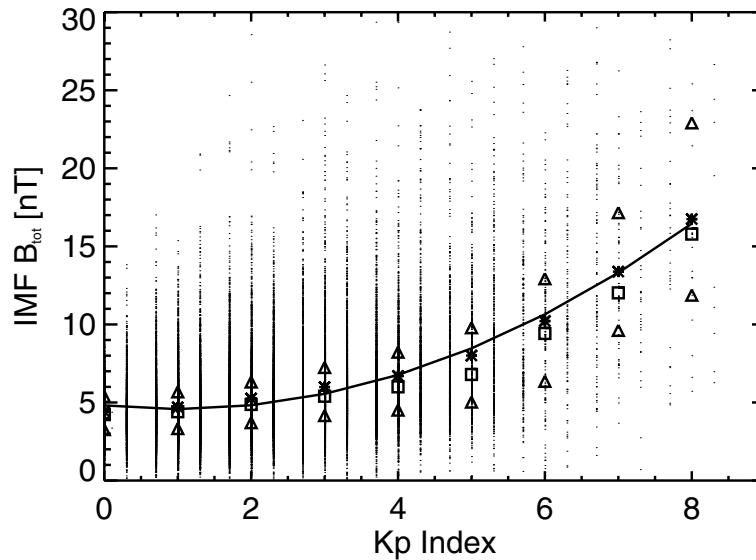


**Figure 4.5:** Relationship between the magnitude of the interplanetary magnetic field and  $Kp$ . The  $Kp$  dependence is approximated as  $B_{\text{tot}} = 4.81 - 0.48 Kp + 0.24 Kp^2$ . The plot symbols are described in the caption of Figure 4.4.

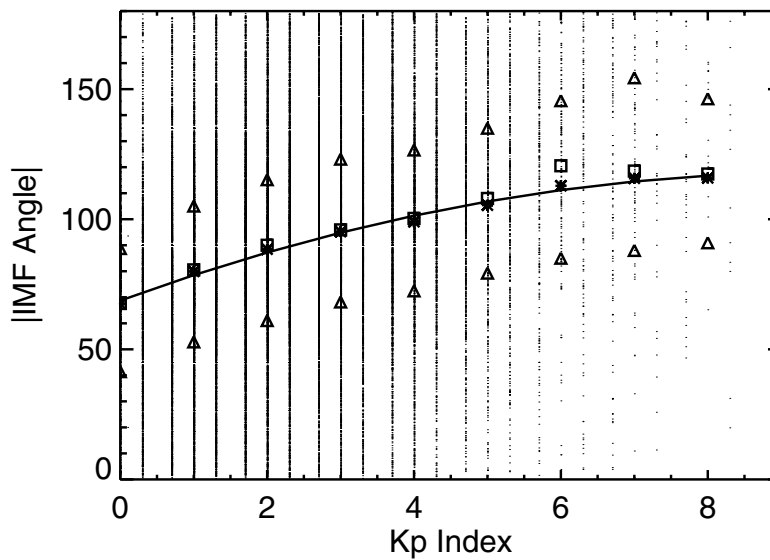


**Figure 4.6:** Relationship between the southward angle of the interplanetary magnetic field and  $Kp$ . The  $Kp$  dependence is approximated as  $\alpha_{\text{IMF}} = 68.7 + 10.3 Kp - 0.5 Kp^2$ . The plot symbols are described in the caption of Figure 4.4.

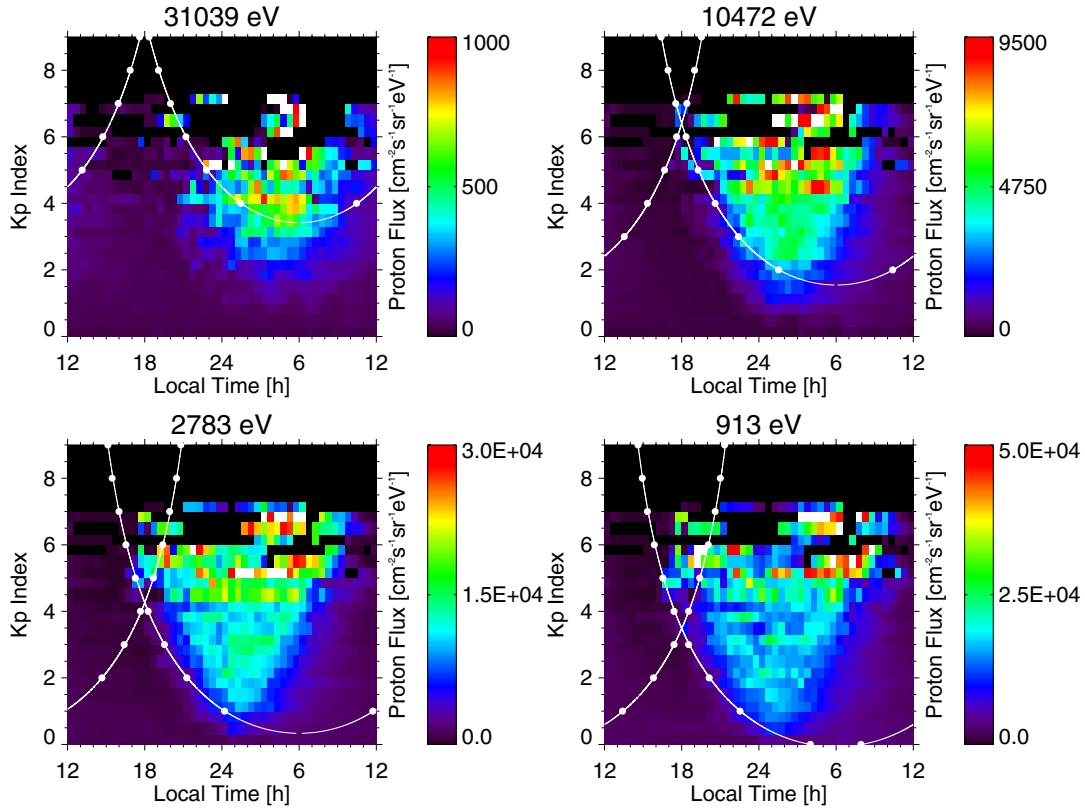


**Figure 4.7:** The 1997-averaged electron flux statistics for energy channels near 30, 10, 3, and 1 keV, binned according to LT and  $Kp$ . Black indicates no data available, and white bins contain fluxes that exceed the corresponding maximum of the color bar. The Alfvén boundary crossings at geosynchronous orbit, indicated by white dots, are numerically evaluated using a dipole magnetic field and a Volland-Stern electric potential with a shielding factor of  $\gamma=2$ . The solid curves show analytically calculated boundaries using the same parameters.

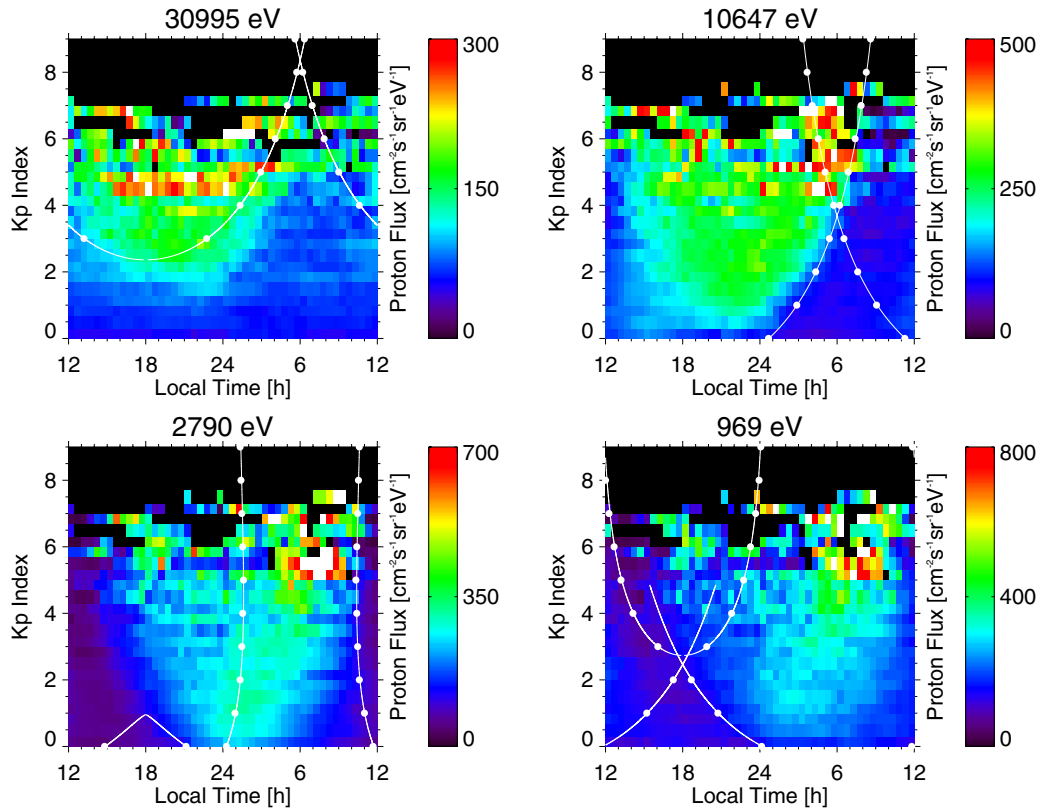


**Figure 4.8:** The 1997-averaged proton flux statistics for energy channels near 30, 10, 3, and 1 keV, binned according to LT and  $Kp$ . Black indicates no data available, and white bins contain fluxes that exceed the corresponding maximum of the color bar. The Alfvén boundary crossings at geosynchronous orbit, indicated by white dots, are numerically evaluated using a dipole magnetic field and a Volland-Stern electric potential with a shielding factor of  $\gamma=2$ . The solid curves show analytically calculated boundaries using the same parameters.

## 4 Generalization to Numerical Global Field Models

---

and a  $Kp$  dependent Volland-Stern electric potential pattern for a shielding factor of  $\gamma=2$ , while the white dots indicate boundary crossings calculated numerically as described above for the same model. The  $Kp$  parameterization of the Volland-Stern model is described in detail in section 3.3. The agreement of the numerically obtained boundary crossings with the analytical results from the previous work demonstrates the validity of the numerical algorithm.

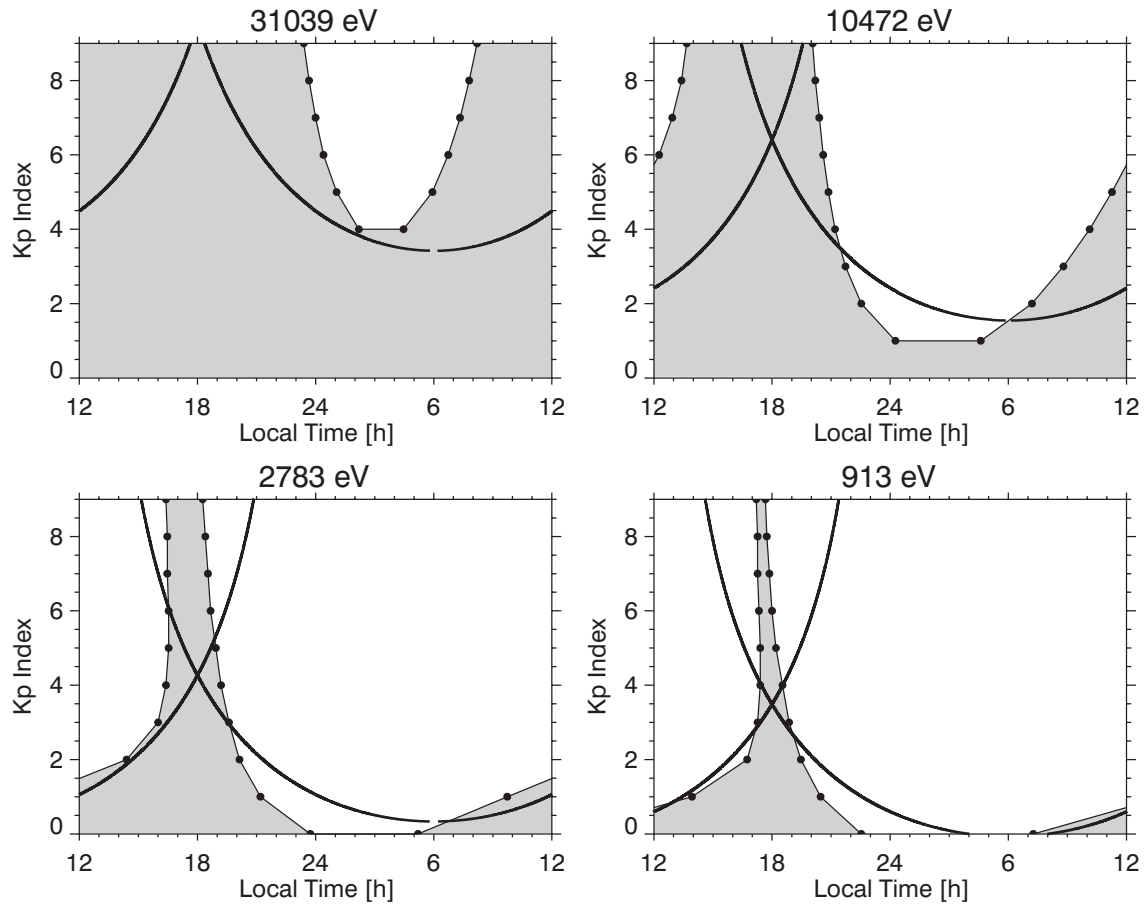
The comparisons between the analytical Volland-Stern and dipole model and the more sophisticated model combinations are shown in Figures 4.9–4.14. The plot format of Figures 4.9–4.14 is identical to that of Figures 4.7 and 4.8 except that the color-coded fluxes are omitted. Closed drift trajectory regions are grey-shaded in Figures 4.9–4.14. Where no grey-shading is indicated, the Alfvén boundaries separate particle paths passing the Earth on the dawnside from duskside trajectories. Figures 4.9 and 4.10 show the boundary crossings calculated with the McIlwain E5D/M2 model for electrons and protons, respectively. The boundaries obtained from the ionospheric electric potential models, all used in combination with a tilted dipole plus Tsyganenko 89c magnetic field, are presented in Figures 4.11–4.14. While both electron and proton boundaries are shown for the Sojka 86 electric potential (Figures 4.11 and 4.12, respectively), only electron boundaries are illustrated for the Heppner-Maynard-Rich and the Weimer 96 models (Figures 4.13 and 4.14, respectively).

For the most part, the Alfvén boundary crossings obtained from the E5D/M2 model for electrons and protons compare well with the observations, in some cases exceeding the quality of the Volland-Stern and dipole model. This is especially true for the energy channels 10 keV and below. Only the 30-keV channels, especially of the electrons, disagree with the observations and show an open trajectory region that is too small compared to the observed fluxes.

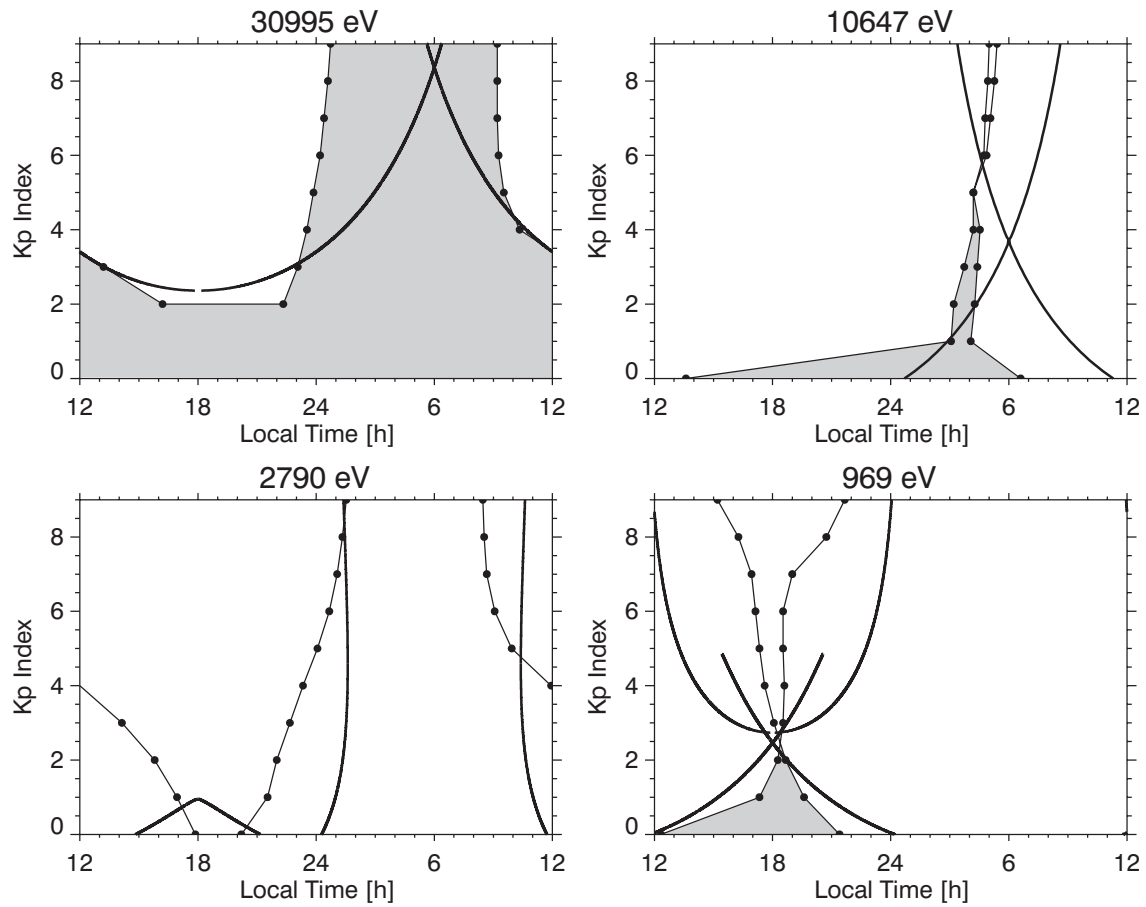
The electron Alfvén boundary crossings determined from the Sojka 86 model (Figure 4.11) are similar to the ones from the Volland-Stern and dipole model. However, comparison with Figure 4.7 shows that the shape of the numerically evaluated boundary curves does not provide a better interpretation for the observations than do the boundaries obtained from the analytical model. The proton boundaries (Figure 4.12) support this suggestion and even show that the Volland-Stern and dipole curves describe the observations appreciably better (cf. Figure 4.8).

Figure 4.13 shows that like the Sojka model, the Heppner-Maynard-Rich model does not reproduce the observed electron flux boundaries better than the Volland-Stern model. On the other hand, electron flux boundaries determined from the Weimer model (Figure 4.14) are at least as good as, if not better, than the Volland-Stern boundaries. However, the proton boundaries for these models (not shown) prove to be inferior to the Volland-Stern and dipole proton boundaries.

All graphs shown here are computed for the equinox period. However, the results turn out to be essentially the same for other seasons.



**Figure 4.9:** Comparison of electron Alfvén boundary crossings obtained with McIlwain E5D/M2 (dotted line) and Volland-Stern and dipole model (solid line). The plot format is identical to that of Figures 4.7 and 4.8 except for the omission of the color-coded fluxes. Regions associated with closed drift trajectories are grey-shaded.



**Figure 4.10:** Comparison of proton Alfvén boundary crossings obtained with McIlwain E5D/M2 (dotted line) and Volland-Stern and dipole model (solid line). The plot format is identical to that of Figures 4.7 and 4.8 except for the omission of the color-coded fluxes. Regions associated with closed drift trajectories are grey-shaded.



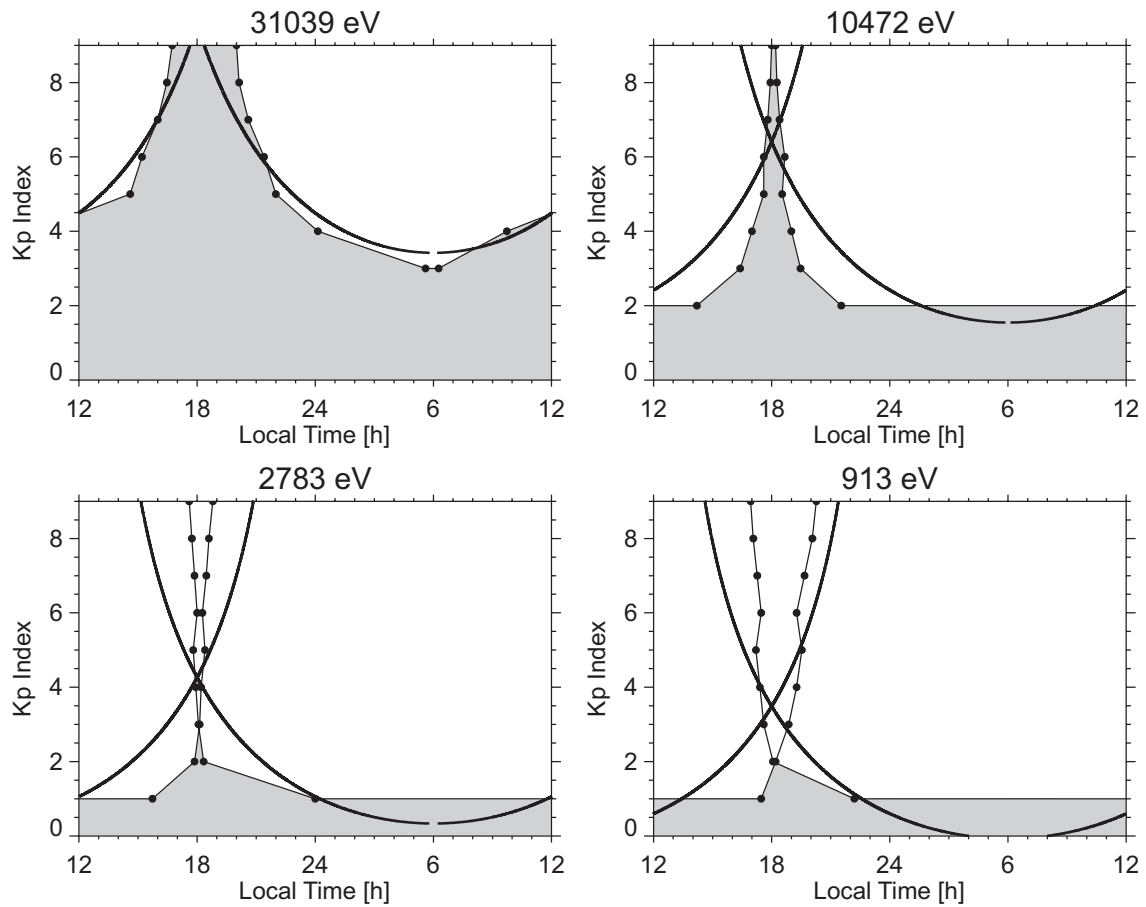


**Figure 4.11:** Comparison of electron Alfvén boundary crossings obtained with Sojka 86 and dipole+T89c model (dotted line) and Volland-Stern and dipole model (solid line). The plot format is identical to that of Figures 4.7 and 4.8 except for the omission of the color-coded fluxes. Regions associated with closed drift trajectories are grey-shaded.

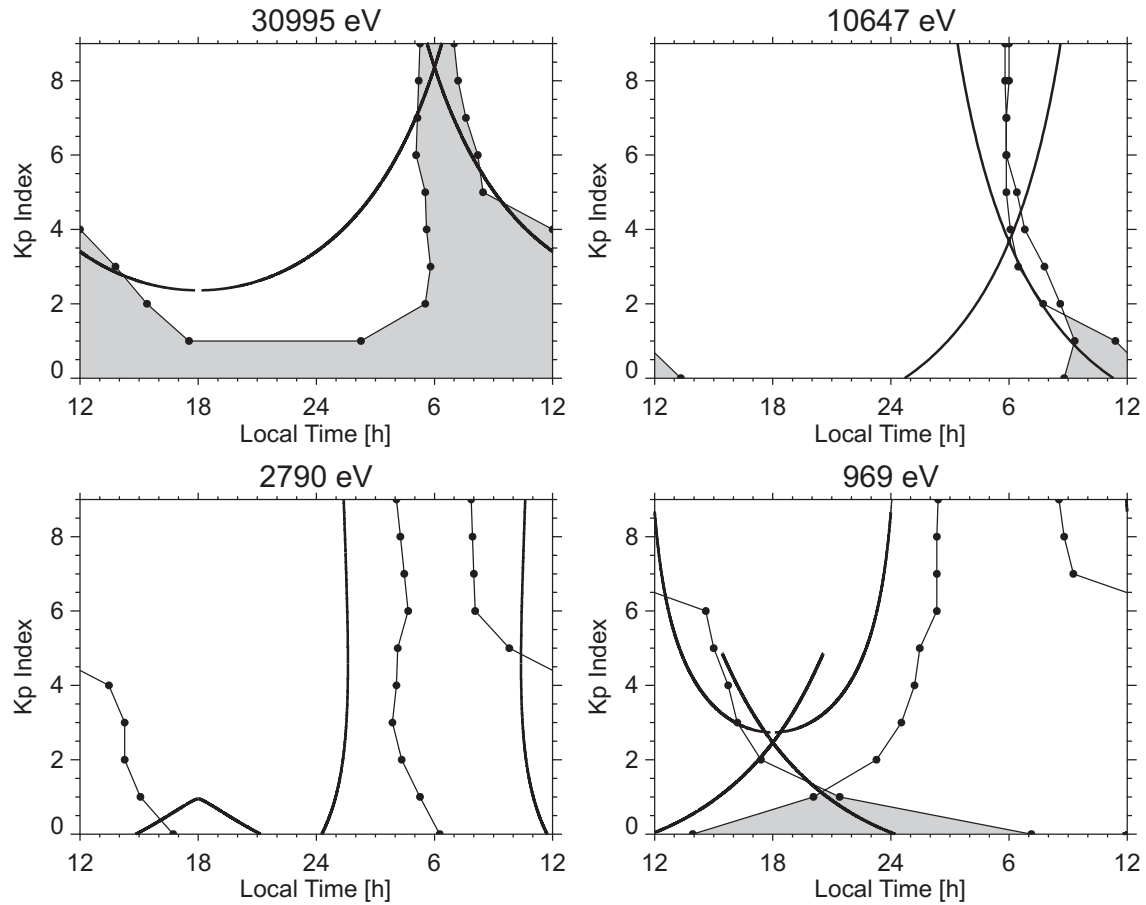


**Figure 4.12:** Comparison of proton Alfvén boundary crossings obtained with Sojka 86 and dipole+T89c model (dotted line) and Volland-Stern and dipole model (solid line). The plot format is identical to that of Figures 4.7 and 4.8 except for the omission of the color-coded fluxes. Regions associated with closed drift trajectories are grey-shaded.

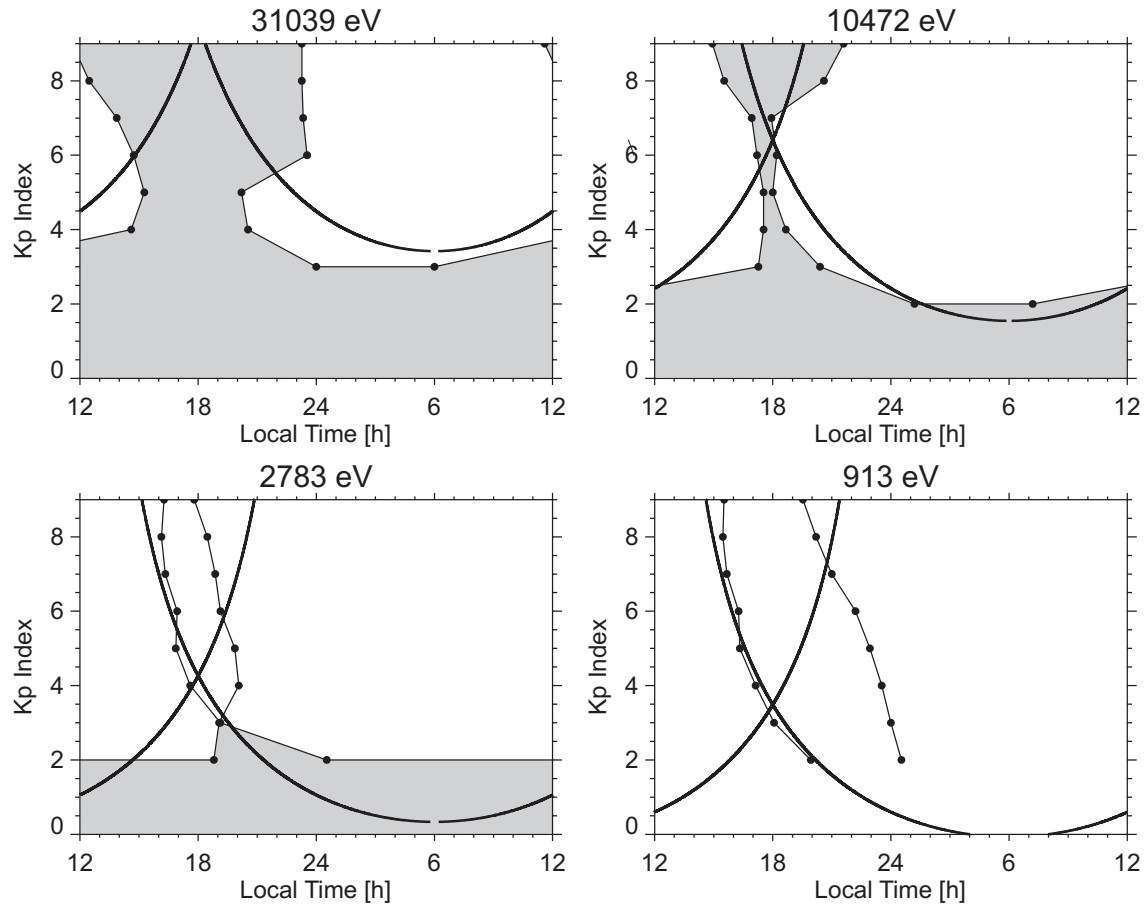


**Figure 4.13:** Comparison of electron Alfvén boundary crossings obtained with Heppner-Maynard-Rich and dipole+T89c model (dotted line) and Volland-Stern and dipole model (solid line). The plot format is identical to that of Figures 4.7 and 4.8 except for the omission of the color-coded fluxes. Regions associated with closed drift trajectories are grey-shaded.

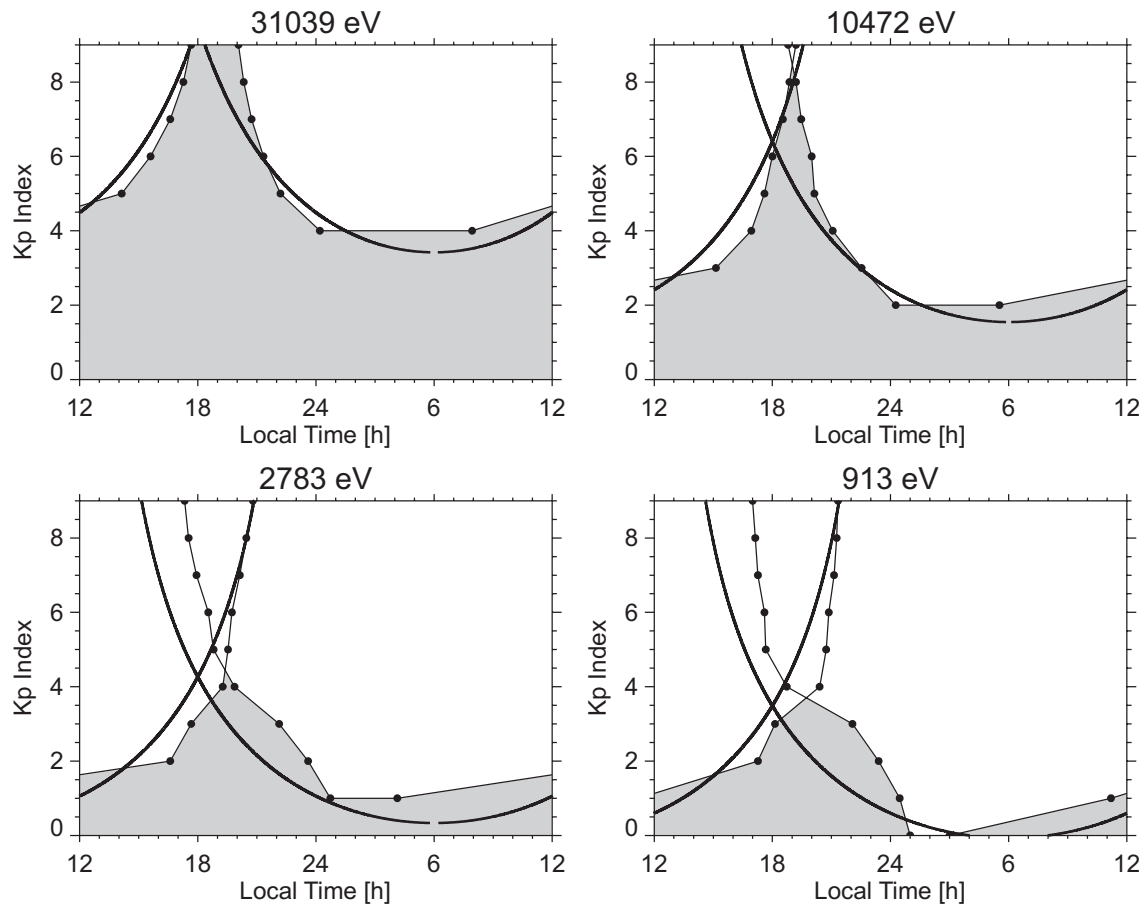


**Figure 4.14:** Comparison of electron Alfvén boundary crossings obtained with Weimer 96 and dipole+T89c model (dotted line) and Volland-Stern and dipole model (solid line). The plot format is identical to that of Figures 4.7 and 4.8 except for the omission of the color-coded fluxes. Regions associated with closed drift trajectories are grey-shaded.

### 4.5 Discussion

The observed geosynchronous particle fluxes presented in this and the previous study are statistical averages over a whole year's worth of data. Consequently, comparison with any field model can only be done in a statistical sense that averages over the influence of any dynamic effects. However, the magnetic field and electric potential models used in this work similarly average over the detailed temporal variability of the geomagnetic activity, thus eliminating the dynamic effects as a reason for major discrepancies between the models and the observations.

The Alfvén boundary crossings calculated from the analytical Volland-Stern and dipole model fit the observations remarkably well on the nightside, considering the simplicity of this model. On the dayside the observed boundaries are not solely access-related. Loss processes such as auroral precipitation of the electrons and charge exchange of the protons with exospheric neutrals diminish the fluxes significantly on their drift around the Earth. This is particularly true for lower-energy particles that not only have slower drift speeds but also execute their drifts closer to the Earth than do higher-energy particles. The loss processes are described in more detail in section 3.5 and references therein.

The E5D electric potential model and the M2 magnetic field model were especially designed for use in the inner magnetosphere. Both models are fits to geosynchronous observations made by ATS satellites, which explains the good match of the boundary crossings calculated from this model with the statistical observations of the MPA instrument. However, the convection electric field strength of the E5D model, which is linearly scaled with  $Kp$ , seems to be underestimated during active periods (see the upper portion of the various panels in Figures 4.9 and 4.10). This conclusion is supported by *Maynard and Chen* [1975] where a nonlinear growth of the convection electric field with  $Kp$  was proposed. Another reason for differences between the model and observational boundaries is the use of the M2 magnetic field model for a wide range of  $Kp$ . The M2 model was originally derived for geomagnetically quiet periods and may not be valid during active times.

The relatively less satisfactory results obtained from the ionospheric electric potential models used in combination with the Tsyganenko 89c magnetic field model are a surprise that needs to be investigated in more detail. One question to be addressed is whether it is primarily the different convection model or the different magnetic model that most affects the boundary location. The impact of the electric and magnetic field models on the crossing locations can be examined separately by substituting only one numerical model at a time. Choosing the analytical Volland-Stern and dipole model as a base, I compare the well-fit boundary crossings of this model with the Volland-Stern and dipole+T89c and the Sojka and dipole combinations. The electron boundary crossings obtained from the Volland-Stern and dipole+T89c and the Sojka and dipole models are shown in Figures 4.15 and 4.16, respectively. The Sojka model is merely an example; other potential models give qualitatively similar results.

The graphs in Figure 4.15 show that the inclusion of an external magnetic field model in addition to the dipole leads to significant deviations from the base model. Comparison

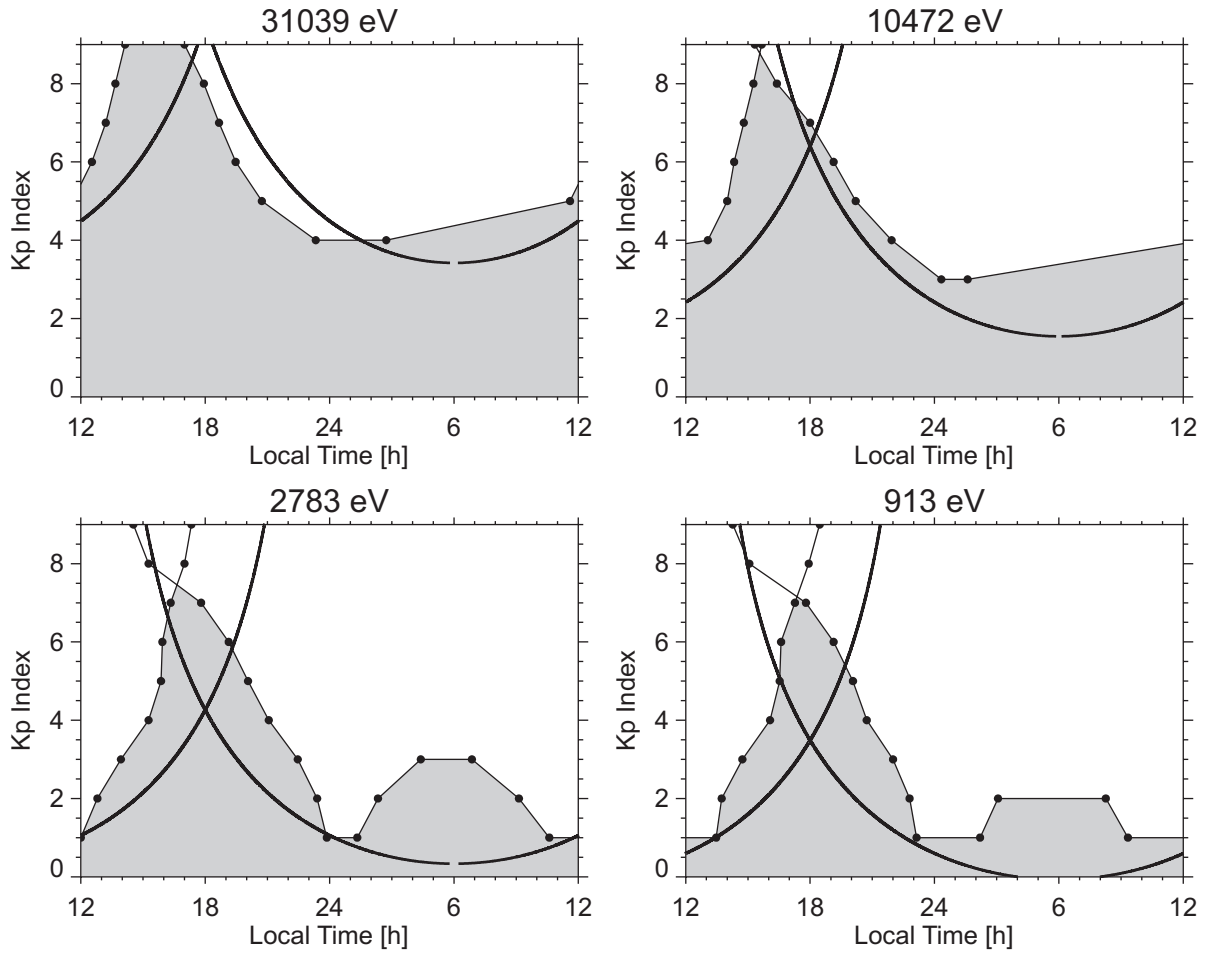


**Figure 4.15:** Comparison of electron Alfvén boundary crossings obtained with Volland-Stern and dipole+T89c model (dotted line) and Volland-Stern and dipole model (solid line). The plot format is identical to that of Figures 4.7 and 4.8 except for the omission of the color-coded fluxes. Regions associated with closed drift trajectories are grey-shaded.

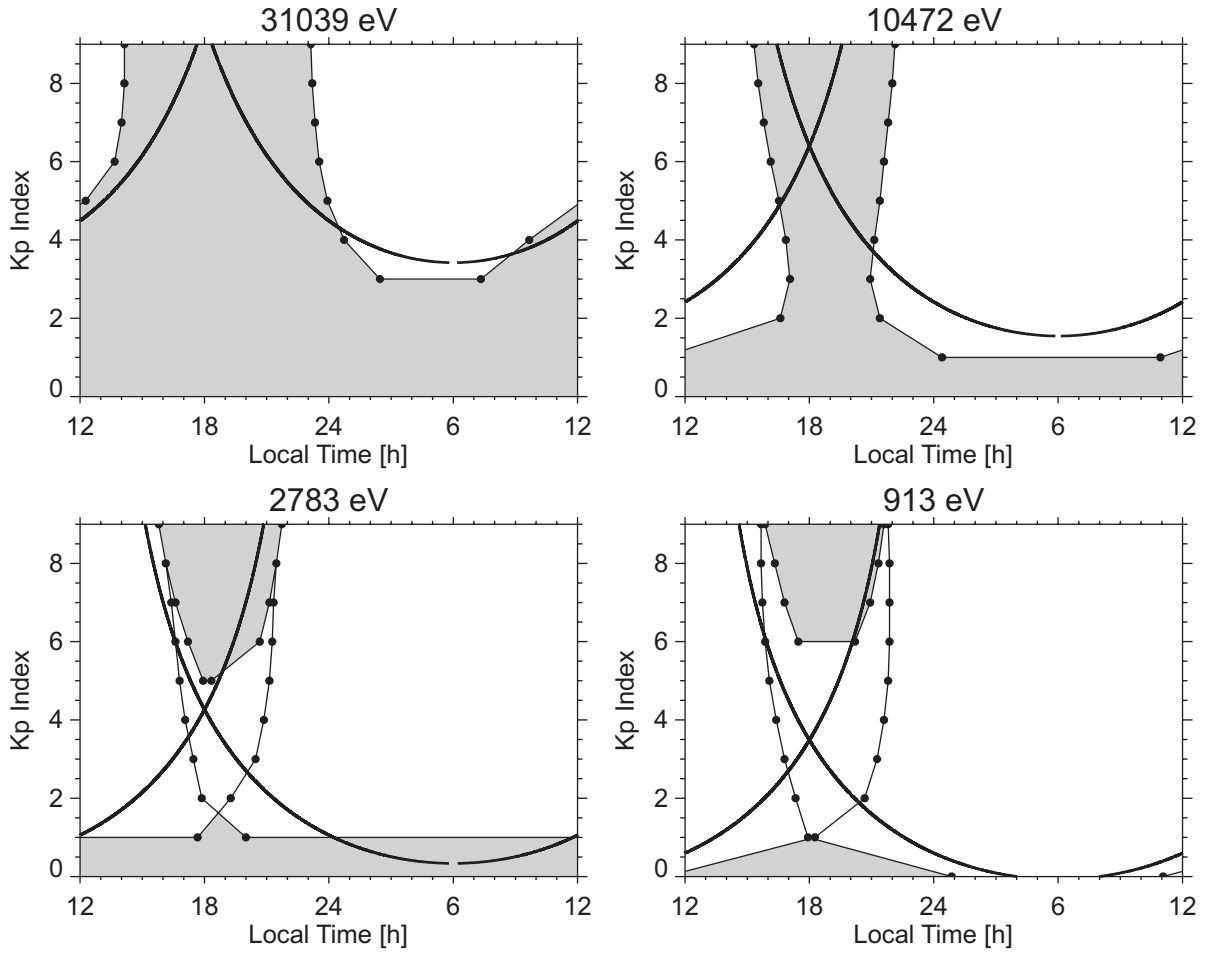


**Figure 4.16:** Comparison of electron Alfvén boundary crossings obtained with Sojka and dipole model (dotted line) and Volland-Stern and dipole model (solid line). The plot format is identical to that of Figures 4.7 and 4.8 except for the omission of the color-coded fluxes. Regions associated with closed drift trajectories are grey-shaded.

## 4 Generalization to Numerical Global Field Models

---

to Figure 4.7 shows that the resulting boundary curves still compare reasonably well to the observations but with no dramatic improvements relative to the dipole results. The most distinctive difference seen in Figure 4.15 is an enhanced closed region at dawn in the lower-energy channels. This region is likely to be an artifact of the analysis technique. The open/closed region type is resolved far down the tail at low magnitudes of the magnetic field. At these distances the terminators are located very close to the magnetopause, where the validity of the magnetic field model and the mapping of the ionospheric potential models are questionable. However, the observations do not definitively rule out the existence of such a region. Low fluxes are indeed observed in this region, but I suspect that they are more likely to be caused by flux decay due to auroral electron precipitation as suggested in the previous chapter rather than a closed orbit region.

The boundary crossings in Figure 4.16, showing the Sojka and dipole model, provide a significantly worse match to the observed flux boundaries compared to the analytical model. The most obvious difference from the simple model is a larger closed region at high  $Kp$  for higher energies. Moreover, closed drift orbits that do not encircle the Earth form in the dusk sector during high activity. These drift paths are the banana orbits discussed in section 3.3. These high- $Kp$  effects can not be compared to observations, owing to a lack of sufficient statistical coverage of high-activity intervals.

The best correspondence between the observed flux boundaries and the theoretical Alfvén boundaries calculated from the Sojka model is achieved by substitution of both electric and magnetic field models simultaneously, as shown in Figure 4.11.

Of all models examined, only the lower-energy boundaries of the McIlwain E5D/M2 combination and the electron boundaries obtained from the Weimer and dipole+T89c model reproduce the observed boundaries as well as or better than the Volland-Stern and dipole analytical model. All other models lead to less satisfactory boundary representations. However, since the high-energy boundaries of the McIlwain E5D/M2 model and the proton boundaries of the Weimer and dipole+T89c model are very questionable, I conclude that in spite of its lack of sophistication, the Volland-Stern and dipole model combination still provides the best description of the statistical access of the plasma sheet to geosynchronous orbit. I emphasize again that I may be pushing the high-latitude models beyond their appropriate limits. Thus a disagreement between these models and the geosynchronous observations does not imply the general invalidity of the models but rather emphasizes the need for better convection models in the region examined in this study.

### 4.6 Summary

In this study I expanded on the previous work of chapter 3, developing a numerical technique to determine the Alfvén boundary crossings of geosynchronous orbit, using the  $(U, B, K)$  technique. Numerical analysis as opposed to analytic expressions has the advantage of allowing the use of arbitrary, empirical electric potential and magnetic field models that may be more accurate than simple analytical models. However, my calculations show that



## 4 Generalization to Numerical Global Field Models

---

not only is the use of more sophisticated models more complicated and time-consuming, but the models examined here do not provide a better representation of the observed, statistical flux boundaries than does the Volland-Stern and dipole model. This result emphasizes the need for caution in extrapolating high-latitude convection models into the near-Earth region.

An additional problem I encountered in this work is that artificial boundary crossings can at times be produced by numerical difficulties of the Hamiltonian approach. Problems occur especially whenever the open/closed determination is done at low magnitudes of the magnetic field ( $\lesssim 30$  nT). Considering the numerical complications, computation time, and the fact that the sophisticated models do not provide better insight into the average plasma sheet delivery to geosynchronous orbit than does the Volland-Stern and dipole model, I find the analytical model to be more satisfactory for describing the average statistical picture. Nevertheless, since the problems in applying the numerical algorithm to the various convection and magnetic field models were primarily encountered at low  $B$  (large distances from the Earth), the  $(U, B, K)$  approach described in this study can still be very effectively used to examine drift paths closer to the Earth (e.g., near and inside of geosynchronous orbit), preferably with convection models tailored to near-Earth conditions.

# 5 Particle Tomography of the Inner Magnetosphere

## 5.1 Overview

In the previous statistical analysis the mean spin-averaged particle fluxes were determined as a function of local time and Kp index, averaged over an entire year of observations. Particles on open drift trajectories should cross geosynchronous orbit twice during their drift from the nightside plasma sheet, through the inner magnetosphere, and out to the dayside magnetopause. The ratio of incoming plasma sheet phase space density and outgoing dayside phase space density of every drift path thus contains information about particle losses during the drift through the near-Earth region. For ions, the losses are largely caused by charge exchange reactions with hydrogen atoms. Applying tomographic inversion techniques, I use the observed statistical losses inside the geosynchronous orbit region to infer the spatial distribution of exospheric neutral hydrogen. The particle drift paths from the nightside of geosynchronous orbit to the dayside are calculated from electric and magnetic field models. To test the sensitivity of the tomography to the convection model, I invert the geosynchronous particle observations using various field model combinations and compare the results. The neutral hydrogen densities obtained from the inversion are found to disagree with existing models of the exosphere, mainly in the near-Earth region. These differences are due to lower-than-expected losses of lower-energy particles that nominally drift through the inner region and/or particle sources not considered in the study.

## 5.2 Introduction

The chapters 3 and 4 provided comprehensive insight into particle drifts in the terrestrial magnetosphere and the two classes of particle trajectories that these drifts take place on. The application presented in this chapter focuses on the region of open drift paths. Particles on these trajectories should cross geosynchronous orbit twice during their drift from the nightside plasma sheet, through the inner magnetosphere, and out to the dayside magnetopause. In the absence of any sources or losses, Liouville's theorem states that the phase space density remains constant along the drift path. Thus the phase space density at the two

## 5 Particle Tomography of the Inner Magnetosphere

---

geosynchronous crossing locations of a drift trajectory would be equal under these conditions ( $f_{\text{in}} = f_{\text{out}}$ ). However, if losses occur or sources exist earthward of geosynchronous orbit, they should be reflected in the ratios of the incoming and outgoing phase space density  $f_{\text{in}}/f_{\text{out}}$ . With many such two-point measurements (in/out) one could utilize tomographic inversion techniques to infer physical quantities related to the sources and losses in the inner magnetosphere. While I do not have a set of such two-point measurements, I do have the statistical equivalent from the study in chapter 3. In this chapter a tomographic algorithm is developed to determine the exospheric neutral hydrogen density distribution inside geosynchronous orbit from these statistical observations. Knowledge of the distribution of neutrals in the exosphere is particularly important for deducing ion distributions from measurements of energetic neutral atoms [e.g., *Roelof*, 1987, 1997; *Henderson et al.*, 1999].

The Earth's geocorona is created by escaping hydrogen atoms produced by photodissociation of water vapor and methane in the lower thermosphere. The hydrogen escape is mainly caused by thermal evaporation and charge exchange with plasmaspheric protons. Thermal evaporation, also referred to as Jeans escape [*Jeans*, 1954, p. 342], can be explained using the classical view of a collisionless planetary exosphere where atoms leaving the exobase have a Maxwellian distribution of velocities. Those on the high-energy tail of the distribution may attain speeds exceeding the escape velocity for the gravitational field, which at the surface of the Earth is  $v_{\text{esc}} = \sqrt{2GM_{\text{E}}/r} \approx 11$  km/s, where  $G$  is the gravitational constant,  $M_{\text{E}}$  is the mass of the Earth, and  $r$  is the radial distance. Such fast atoms, moving outward in the tenuous outer atmosphere where collisions are rare, will escape into space [*Chamberlain*, 1963]. The hydrogen escape is supplemented by charge exchange with plasmaspheric protons having velocities that exceed the escape velocity of thermal hydrogen [e.g., *Cole*, 1966; *Tinsley*, 1973; *Chamberlain*, 1977]. Several models for the distribution of exospheric hydrogen with a wide range in complexity have been developed in the past. The early *Chamberlain* [1963] model, analytically derived from kinetic theory, described only the radial profile of the hydrogen distribution. More recent models utilize computationally intensive Monte Carlo simulations of the exosphere [*Tinsley et al.*, 1986; *Anderson et al.*, 1987; *Hodges*, 1994]. Tracing a large number of test particles, these models also consider diurnal and solar cycle dependence in determining the neutral distributions.

In this chapter I will explore the possibility of determining the mean (or time averaged) equatorial neutral hydrogen density distribution earthward of geosynchronous orbit from statistics of the proton phase space density compiled from measurements taken by the MPA instruments. Knowing the path of a particle that crosses geosynchronous orbit twice (i.e., entering the inner magnetosphere on the nightside and exiting on the dayside) and assuming charge exchange of the protons with exospheric neutral hydrogen to be the only loss process, the particle losses suffered along the trajectory can be used to infer the neutral density inside geosynchronous orbit. In this study losses due to Coulomb collisions are neglected since charge exchange outweighs this mechanism by far in the plasma sheet energy range [*Fok et al.*, 1991; *Jordanova et al.*, 1996]. I calculate the bounce-averaged particle trajectories from a model electric potential distribution in a dipolar magnetic field. I then

invert the observed statistical in/out ratios to derive the distribution of neutral hydrogen in the inner magnetosphere. Finally, the inversion results for several different models of the convection electric field are compared.

To evaluate the performance of the tomography algorithm developed in this study, the results are compared with the Chamberlain model of the exosphere. The Chamberlain model has the advantage that it is not only well established in the literature but its variables can also be reduced to the radial distance from the surface of the Earth using the *Rairden et al.* [1986] parameterization.

### 5.3 MPA Particle Flux Statistics

The flux statistics used in the particle tomography are obtained through the data analysis technique described in chapter 3. However, the year 1997 is chosen for the study since the occurrence of elevated  $Kp$  intervals is higher than during the year 1996, which was considered in the previous work. By this means the statistics at these  $Kp$  levels are improved. Figure 5.1 shows the statistical differential proton fluxes for the year 1997. Like in the previous statistical analysis of chapter 3 the geosynchronous data are binned by local time and the geomagnetic activity given by the  $Kp$  index. The flux values are displayed color-coded, whereas black regions indicate data unavailability, and white bins contain flux values exceeding the maximum of the corresponding color bar. At any given  $Kp$ , higher fluxes in the statistics indicate regions where plasma sheet particles have access to geosynchronous orbit along open drift paths from the tail. The closed drift trajectories can be identified by low fluxes since the plasma sheet does not have access to this region. The geosynchronous Alfvén layer crossings are shown as white lines in the plots. They are calculated from a dipolar magnetic field and a  $Kp$  dependent Volland-Stern electric potential with a shielding factor of  $\gamma=2$  (cf. chapter 3).

Figure 5.1 shows that like for the year 1996 the nightside Alfvén layers obtained from the model fit the observed boundaries in general remarkably well, demonstrating again the statistical suitability of the simple convection model. Nightside boundaries between two regions of open drift trajectories, shown as dashed lines in Figure 5.1, do not correspond to any flux discontinuities and merely separate particles passing the Earth on the dawnside from duskward traveling ones. On the dayside the diminished fluxes are not access-related, but rather suggest that plasma sheet protons experience significant losses as they drift around the Earth.

### 5.4 Global Drift Pattern

For tomographic applications it is essential to know the path along which the decay of a physical property occurs. The drift velocity equation was previously discussed in section 1.2.1. If all particles mirror equatorially (pitch angle  $\alpha=90^\circ$ ), the curvature drift term

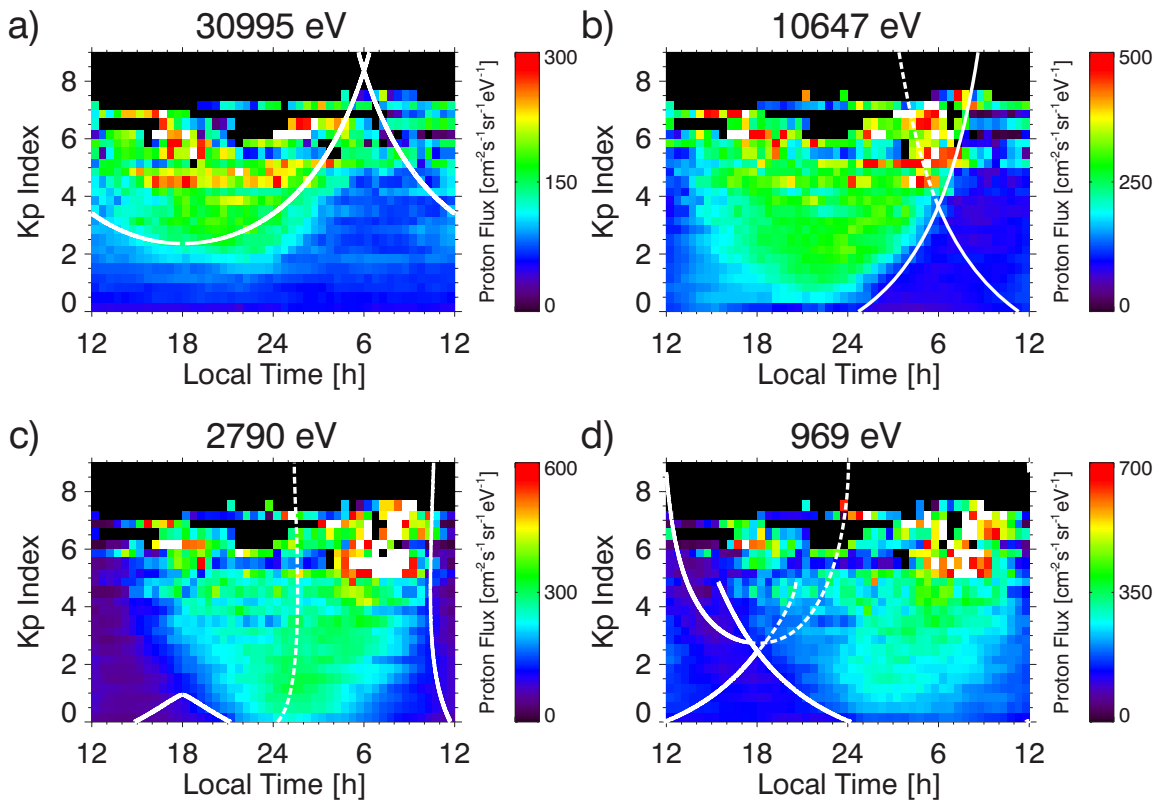


**Figure 5.1:** The 1997-averaged proton flux statistics for energy channels near (a) 30 keV, (b) 10 keV, (c) 3 keV, and (d) 1 keV, binned according to LT and  $Kp$ . Black indicates no data available, and white bins contain fluxes that exceed the maximum of the corresponding color bar. The Alfvén boundary crossings at geosynchronous orbit, indicated by white lines, are evaluated using a dipolar magnetic field and a Volland-Stern electric potential with a shielding factor of  $\gamma=2$ . The dashed lines represent nightside boundaries between two regions of open drift paths and do not correspond to any flux discontinuities.

## 5 Particle Tomography of the Inner Magnetosphere

---

in (1.13) may be omitted. The guiding center drift velocity of a particle within the Earth's magnetosphere can then be expressed as

$$v_D = \frac{\underline{E} \times \underline{B}}{B^2} + \frac{\mu \underline{B} \times \nabla B}{qB^2}, \quad (5.1)$$

where  $\underline{E}$  is the macroscopic electric field,  $\underline{B}$  is the magnetic field, and  $\mu = mv_{\perp}^2/2B$  is the magnetic moment. Applying models for the electric and magnetic field, the drift trajectories can be calculated from (5.1) using a fourth-order Runge-Kutta integration algorithm [Press *et al.*, 1994, p. 704]. In this study I consider electric potential models by Volland and Stern [Volland, 1973, 1975, 1978; Stern, 1975], McIlwain [1986], and Weimer [1995, 1996], which were previously discussed in sections 1.2.2 and 4.3.2. The selection criterion for these models was their suitability for the inner magnetosphere. The magnetic field is represented by a dipole.

With any one of these convection models, equation (5.1) allows the tracing of particle drift trajectories for different local times of the entry point, geomagnetic activity levels, and particle energies. The multitude of feasible drift paths that are obtained by varying these parameters is essential for the tomography. In order to obtain spatial resolution of the loss region, many intersecting drift paths are needed, forming a fine mesh as shown in Figure 5.2. The figure shows the magnetic equatorial plane, with the Earth in the center and distances given in  $R_E$ . The solid curves are drift paths for 1, 3, and 10-keV protons at  $Kp=4$  calculated with the Volland-Stern electric potential in a dipolar magnetic field. The dotted lines show the grid on which the neutral densities will be determined. Figure 5.2 shows only a very small subset of trajectories used in the actual calculation. The complete mesh consists of drift paths originating at 21 distinct local times (every half hour between 1800 LT and 0600 LT), at 12  $Kp$  levels ranging from 0 to 4, and with 14 energy values with center energies spaced logarithmically between 1 keV and 40 keV (corresponding to the MPA energy channels 1–15). Closed drift paths are excluded from the mesh since only the attenuation of fresh plasma sheet plasma, arriving on open trajectories at the nightside geosynchronous region and making a single pass through the inner magnetosphere, can be modeled in this way. Likewise eliminated are paths with drift times greater than five days, which are unlikely to exist due to dynamic effects.

### 5.5 Charge Exchange Process

The loss of protons in the inner magnetosphere is mainly caused by charge exchange with exospheric neutrals and Coulomb collisions with thermal plasma. However, Fok *et al.* [1991] demonstrated that in the plasma sheet, where the number densities are small ( $\sim 0.5 \text{ cm}^{-3}$ ), Coulomb decay is an insignificant loss process in the MPA energy range between 1 keV and 40 keV. Therefore I will neglect Coulomb interactions in this chapter. Furthermore, only charge exchange between protons and exospheric hydrogen atoms will

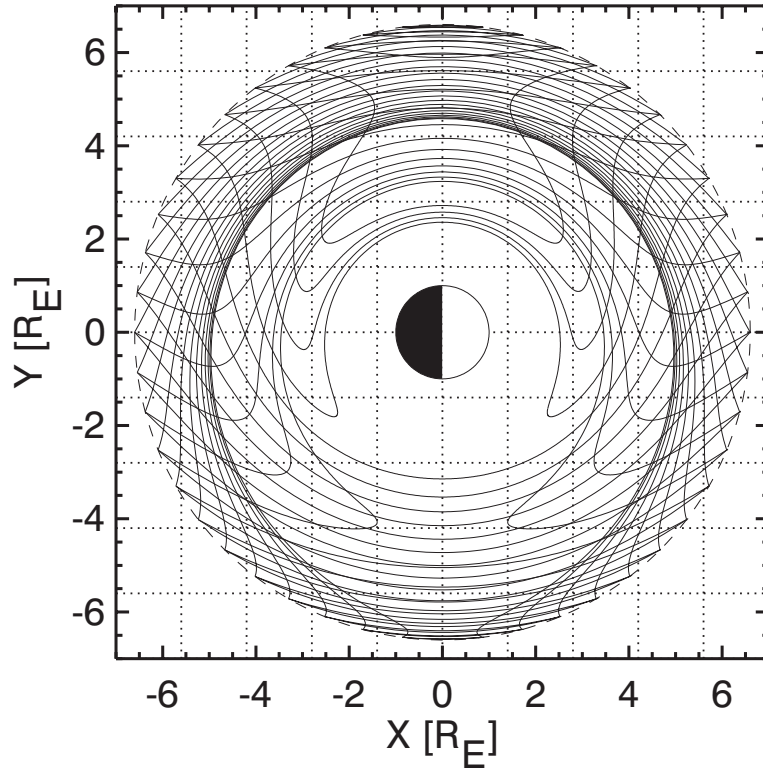
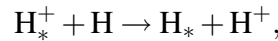


**Figure 5.2:** Drift paths for 1, 3, and 10-keV protons in the equatorial magnetosphere calculated from a magnetic dipole and a Volland-Stern electric potential at  $Kp = 4$ . The dotted lines show the grid for determining the neutral density.

be considered since protons are typically the most abundant ions in the magnetosphere except under extremely disturbed conditions, and hydrogen dominates the neutral population [Hodges and Breig, 1991].

In the charge exchange reaction considered in this study, plasma sheet protons are neutralized by picking up the orbital electron from the thermal hydrogen atom, which then becomes a low-energy proton:



where the asterisk denotes energetic particles. The probability that a charge exchange occurs is expressed as a reaction cross section, which is energy dependent [Barnett, 1990; Funsten, 2000]:

$$\sigma[\text{cm}^2] = 10^A, \quad (5.2)$$

$$A = -2.384 \cdot 10^{-6} E^3 + 3.121 \cdot 10^{-4} E^2 - 0.03507 E - 14.77,$$

where  $E$  is the energy in units of keV. The function (5.2), shown in Figure 5.3, is an approximation of an eighth-order Chebyshev polynomial, valid for energies between 0.7 keV and 60 keV.

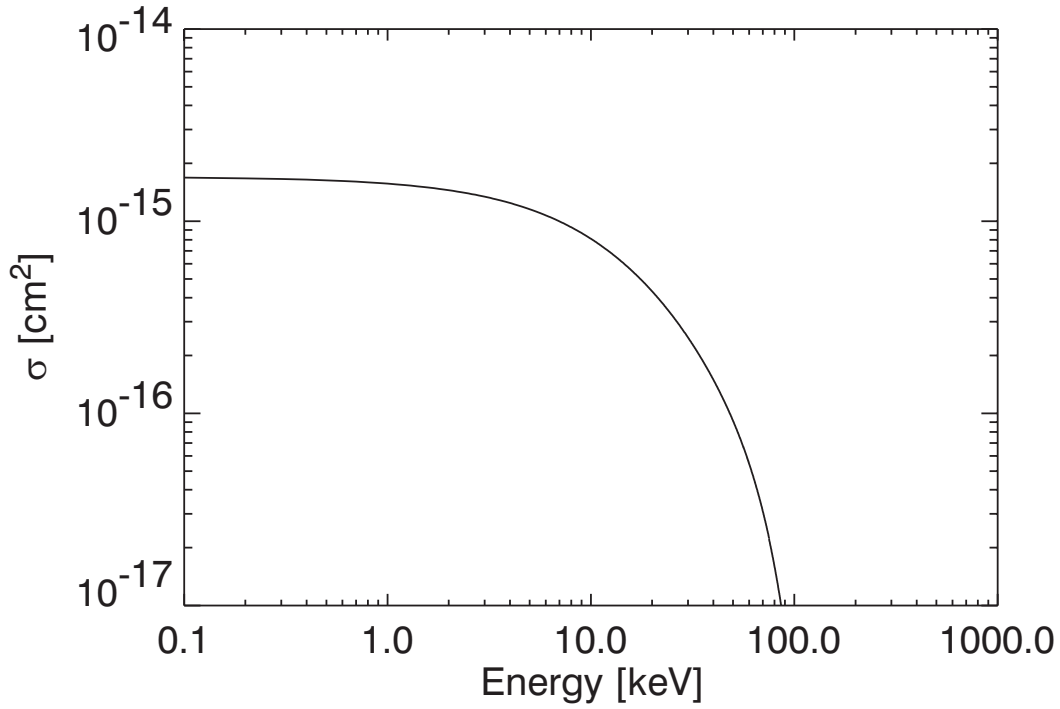


**Figure 5.3:** Approximation of the charge exchange cross section as a function of the particle energy.

With charge exchange assumed to be the only loss process, the change in phase space density along a drift path is described by the continuity equation:

$$\frac{\partial f}{\partial t} + \nabla \cdot (f \underline{v}_D) = -\sigma v_{th} n_H f, \quad (5.3)$$

where on the left-hand side of the equation  $f$  is the phase space density and  $\underline{v}_D$  the drift speed. The right-hand side of (5.3) is the loss term, which is proportional to the charge exchange cross section  $\sigma$ , the thermal speed of the plasma sheet particle  $v_{th}$ , the neutral hydrogen density  $n_H$ , and the phase space density  $f$ . Under stationary conditions (5.3) is reduced to

$$\underline{v}_D \cdot \nabla f = v_D \frac{\partial f}{\partial s} = -\sigma v_{th} n_H f \quad (5.4)$$

since  $\nabla \cdot \underline{v}_D = 0$  holds for the incompressible phase-space fluid (Liouville's theorem) [cf. *Baumjohann and Treumann, 1997, p. 111*]. The differential equation (5.4) has the solution

$$f = f_0 \exp \left( - \int_0^t \sigma v_{th} n_H dt' \right). \quad (5.5)$$

Equation (5.5) describes the evolution of the phase space density  $f$  at time  $t$  from an initial



## 5 Particle Tomography of the Inner Magnetosphere

---

value  $f_0$  at the starting point, suffering charge exchange losses along the drift path. Discretizing the integral, this result may be rewritten as

$$\sum_i \sigma_i v_{\text{th},i} \Delta t_i n_{\text{H},i} = \ln \left( \frac{f_0}{f} \right). \quad (5.6)$$

In (5.6) the index  $i$  represents a cell along the drift path, in which the phase space density decreases by a fraction. The sum of the partial losses in all cells yields the total loss, which is the measured ratio of the phase space density at the entry and exit points at geosynchronous orbit of the specific path. An equation of the form of (5.6) exists for each drift trajectory included in the tomographic mesh. Denoting the drift trajectory with the index  $j$ , one obtains

$$\sum_i \sigma_{ji} v_{\text{th},ji} \Delta t_{ji} n_{\text{H},i} = \ln \left( \frac{f_0}{f} \right)_j. \quad (5.7)$$

The phase space density  $f$  is derived from the differential flux  $F$  as

$$f = \frac{m^2}{2E} F, \quad (5.8)$$

where  $m$  is the mass of the particles, and  $E$  is their energy (cf. section 2.5). In an aligned dipole magnetic field, geosynchronous orbit is assigned a constant magnetic field value. In such a field, particles that conserve their first adiabatic invariant,  $\mu = E_{\perp}/B$ , during their drift motion through the inner magnetosphere will have the same energy as they cross geosynchronous orbit on their inbound and outbound legs. Therefore the total loss rate of phase space density and differential fluxes are interchangeable under these conditions. In the analysis described below, I use the ratio of dayside to nightside fluxes, evaluated along each specific drift trajectory.

### 5.6 Tomography Algorithm

In sections 5.3 to 5.5 all necessary information was acquired to derive the neutral hydrogen density in the inner magnetosphere from the geosynchronous statistics. The drift pattern provides a multitude of trajectories, the data supply the phase space densities for the night- and dayside ends of each trajectory, and the decay equation (5.5) represents a functional relationship between the observed depletions and the neutral hydrogen density.

For the development of the tomography algorithm I use a neutral density model consisting of a regular array of homogeneous square blocks indicated in Figure 5.2 by the dotted lines. Consequently the model's geometry is completely specified by setting the number of blocks along the  $x$  axis ( $N_x = 10$ ) and the number of blocks along the  $y$  axis ( $N_y = 10$ ). Subsequently the cells in the model are mapped onto the set of integers  $\{1, \dots, N_x N_y\}$ : Let  $(1, 1)$  be the upper-left corner,  $(N_x, 1)$  the upper-right corner, and  $(N_x, N_y)$  the lower-right corner.

## 5 Particle Tomography of the Inner Magnetosphere

---

The matrix of neutral densities  $n_H$  in each of the cells is similarly mapped onto the vector  $\underline{m}$  a row at a time, starting with the first row:

$$\underline{m} = \{n_H(1, 1) \dots n_H(N_x, 1), n_H(1, 2) \dots n_H(N_x, 2), \dots, n_H(1, N_y) \dots n_H(N_x, N_y)\}.$$

The generalization of (5.6) given in (5.7) is thus a matrix equation

$$\underline{\underline{A}} \underline{m} = \underline{d}, \quad (5.9)$$

in which the elements of the matrix  $\underline{\underline{A}}$  represent the drift loss term  $A_{ji} = \sigma(E_{ji}) v_{th}(E_{ji}) \Delta t_{ji}$  if the  $j^{\text{th}}$  trajectory passes through cell  $i$ , and  $A_{ji} = 0$  if the  $j^{\text{th}}$  trajectory does not pass through the  $i^{\text{th}}$  cell. Note that the cross section and particle speed need to be evaluated at the local energy corresponding to the magnetic moment of the  $j^{\text{th}}$  trajectory. The elements of the vector  $\underline{d}$  contain the logarithms of the phase space density ratios (or, as discussed above, the flux ratios) corresponding to each drift path (cf. equation (5.7)). The neutral densities in the inner magnetosphere are thus found by solving the matrix equation (5.9).

The invertibility of a matrix is subject to the conditions that it be square and regular (i.e., nonsingular, with rows that are linearly independent) [Strang, 1988, p. 46]. These conditions are not in general met for the matrix  $\underline{\underline{A}}$  defined above. Therefore steps have to be taken to insure compliance with these conditions: The matrix  $\underline{\underline{A}}$  given above is often nonsquare since the number of observations usually exceeds by far the total parameters to be resolved. In the above example the matrix has 100 columns using a grid of  $10 \times 10$  cells. By comparison, the row span, given by the number of available drift paths, is greater than 2000. However, multiplication of (5.9) with the transpose of  $\underline{\underline{A}}$  from the left side

$$\underline{\underline{A}}^T \underline{\underline{A}} \underline{m} = \underline{\underline{A}}^T \underline{d} \quad (5.10)$$

produces a square matrix on the left side of the equation. Assuming  $\underline{\underline{A}}^T \underline{\underline{A}}$  to be regular, the model solution  $\underline{m}$  is thus found to be

$$\underline{m} = (\underline{\underline{A}}^T \underline{\underline{A}})^{-1} \underline{\underline{A}}^T \underline{d} = \underline{\underline{A}}^+ \underline{d}, \quad (5.11)$$

where the matrix  $\underline{\underline{A}}^+ = (\underline{\underline{A}}^T \underline{\underline{A}})^{-1} \underline{\underline{A}}^T$  is referred to as the *pseudoinverse*. Since the system of linear equations (5.9) is over-determined, it is unlikely that the solution vector  $\underline{m}$  will fit the data perfectly. Instead the procedure described in (5.11) is equivalent to minimizing the error term  $E = \|\underline{\underline{A}} \underline{m} - \underline{d}\|$  [Strang, 1988, p. 154] and is thus called the least-square solution.

In obtaining (5.11)  $\underline{\underline{A}}^T \underline{\underline{A}}$  was assumed to be nonsingular. In tomographic applications this characteristic is not necessarily met but there are several techniques to insure regularity. The simplest method is to add to  $\underline{\underline{A}}^T \underline{\underline{A}}$  an identity matrix with a small weighting factor since the rows of such a matrix are always linearly independent. However, this method puts no constraint on the similarity of adjacent elements of the solution. Therefore, tomographic images tend to be rough when the data are noisy or inconsistent [Phillips and Fehler, 1991].

## 5 Particle Tomography of the Inner Magnetosphere

---

A more physical approach is to require a smooth solution, which is accomplished by using a first difference operator for the constraints [Shaw and Orcutt, 1985; Scales *et al.*, 1990]. Under this condition the solution to the system of linear equations is found to be

$$\underline{m} = (\underline{A}^T \underline{A} + \lambda \underline{D}^T \underline{D})^{-1} \underline{A}^T \underline{d}, \quad (5.12)$$

where  $\underline{D}$  represents the first difference operator, and the weighting factor  $\lambda$  regulates the smoothness of the solution. For  $\underline{D}$ , differences are taken for all possible adjacent pairs, forcing the correlation between model parameters in the solution, e.g.:

$$\underline{D} = \begin{pmatrix} -1 & 1 & 0 & \dots & \dots & 0 \\ 0 & -1 & 1 & 0 & \dots & 0 \\ 0 & 0 & -1 & 1 & 0 & \dots & 0 \\ \dots & \dots & \dots & \dots & \dots & \dots & \dots \\ 0 & \dots & \dots & 0 & -1 & 1 \end{pmatrix}. \quad (5.13)$$

The exact structure of (5.13) depends on the model order.

In order to test the capability of the above technique to determine the neutral hydrogen density in the inner magnetosphere, equation (5.12) is tested using a synthetic data set generated by modeling particle drifts through a Chamberlain exosphere with the *Rairden et al.* [1986] parameterization. The radial profile of the local time independent model is illustrated in Figure 5.4. The hydrogen densities inverted from the simulated densities are shown in Figures 5.5a and 5.6 on two different color scales. These inversion results were obtained with the Volland-Stern convection model, but other electric field models provide similar inversion results. The plots show the equatorial region near and inside geosynchronous orbit, as previously introduced in Figure 5.2. The inverted neutral hydrogen densities in each cell are color coded according to the color bars next to the graphs. The numbers in the cells of Figure 5.5a represent the inverted densities. In Figure 5.6 the numbers in the cells are the ratios between the inverted hydrogen densities and the densities given by the Chamberlain model. The ratios illustrate that the Chamberlain densities are not exactly reproduced. This mismatch is due to the weight of the smoothing operator, which is comparable to the ones used below for inversion of the observed data. In this simulation smoothing is not required for obtaining a valid solution, and selecting  $\lambda$  very small would more accurately reproduce the Chamberlain model. The correct choice for the weighting factor is of great importance since it has substantial influence on the solution. Larger values of  $\lambda$  put more emphasis on smoothing and less on the data. In an extreme case of over-smoothing the inversion simply returns the same average value of the magnetospheric neutral density at every cell of the model.

One measure of the significance of a solution is indicated by the model's resolution matrix, which characterizes to what extent the model parameters are independently predicted by the data. Assuming that there is a true, but unknown set of model parameters  $\underline{m}_{\text{true}}$  that solves  $\underline{A} \underline{m}_{\text{true}} = \underline{d}$ , I inquire how closely a particular estimate of the model parameters  $\underline{m}_{\text{est}}$

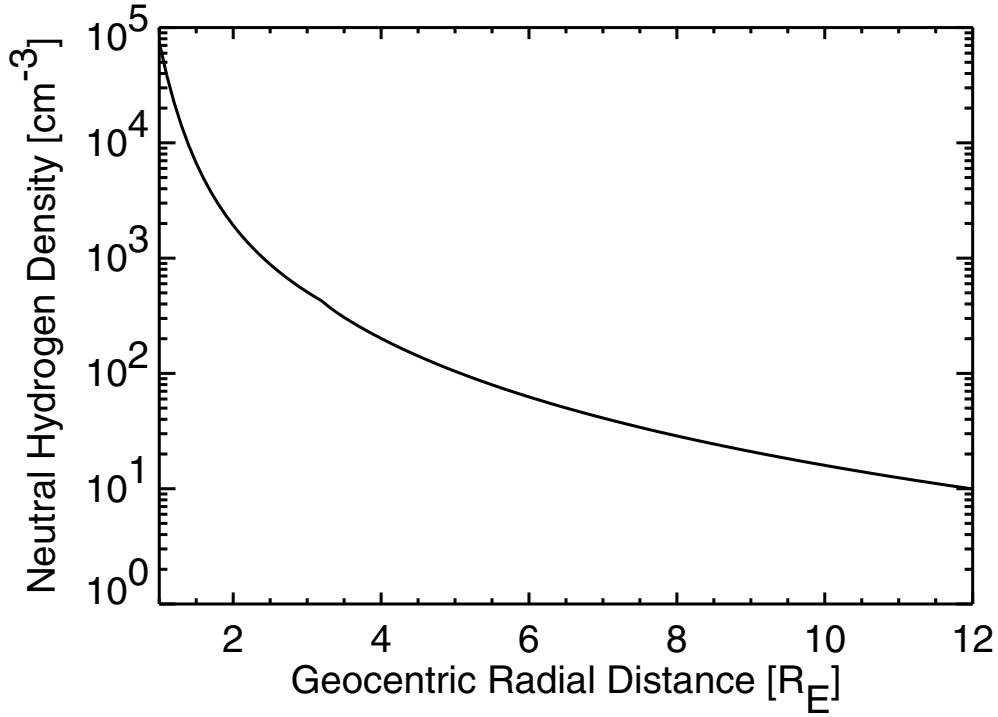


**Figure 5.4:** Radial profile of the exospheric neutral hydrogen density obtained with the Chamberlain model using *Rairden et al.* [1986] parameterization.

is to this true solution. Using the expression for the true model in the expression for the estimated model  $\underline{m}_{\text{est}} = \underline{A}^+ \underline{d}$  gives

$$\underline{m}_{\text{est}} = \underline{A}^+ \underline{A} \underline{m}_{\text{true}} = \underline{R} \underline{m}_{\text{true}}, \quad (5.14)$$

where  $\underline{R} = \underline{A}^+ \underline{A}$  is the resolution matrix. Replacing  $\underline{A}^+$  with the pseudoinverse of (5.12) one finds

$$\underline{R} = (\underline{A}^T \underline{A} + \lambda \underline{D}^T \underline{D})^{-1} \underline{A}^T \underline{A}. \quad (5.15)$$

The resolution matrix has the dimensions  $N_x N_y \times N_x N_y$  and every row of  $\underline{R}$  describes how well a model parameter in one cell can be predicted independently from its neighbors. If  $\lambda = 0$ , the resolution matrix becomes an identity matrix (assuming the data coverage is adequate, i.e.,  $\underline{A}^T \underline{A}$  is nonsingular), and the model is perfectly resolved. For values of  $\lambda$  other than zero  $\underline{R}$  has off-diagonal elements indicating that neighboring regions influence the model prediction in a cell. Of all elements in the resolution matrix, the diagonal elements are most significant because the diagonal elements indicate how much weight a datum has on its own prediction [*Menke*, 1984, p. 64]. Therefore I consider the diagonal elements as a proxy of the resolution.

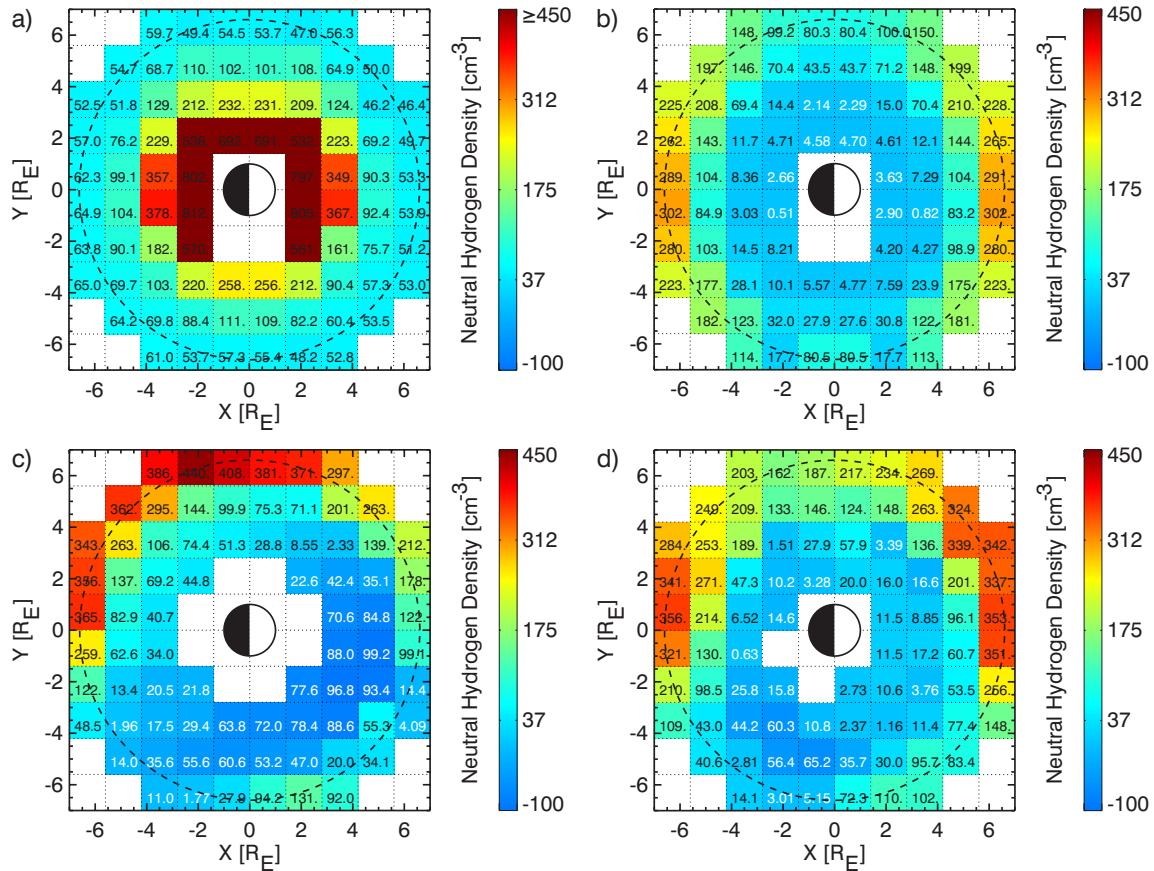


**Figure 5.5:** Neutral hydrogen densities obtained from inversion of the synthetic and measured data sets using various convection models. The densities are color coded according to the color bar next to the figure. The numbers in the cells indicate the inverted densities, with the colors black and white representing positive and negative values, respectively. (a) Synthetic data inverted with the Volland-Stern drift pattern. The other graphs show the densities derived by inverting the MPA data, using convection models by (b) Volland-Stern, (c) McIlwain E5D, and (d) Weimer 96.

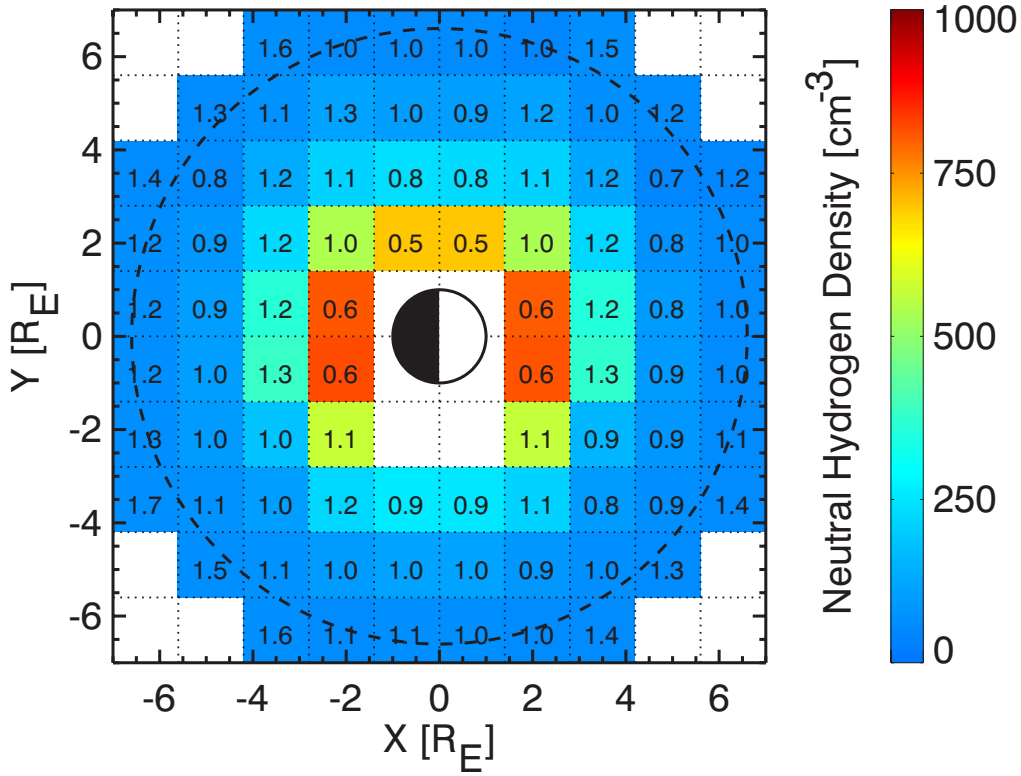


**Figure 5.6:** Neutral hydrogen densities from inversion of synthetic data obtained by forward modeling drifts through a Chamberlain exosphere with *Rairden et al.* parameters. The densities in the equatorial plane are color coded according to the color bar next to the figure. The numbers in the cells indicate the ratios between the inverted densities and the densities of the Chamberlain model. The smoothing operator is weighted with  $\lambda = 10^{-2}$ .

Expression (5.15) implies a trade-off between resolution and variance of the solution. For small values of  $\lambda$  the resolution is good but the variance large. On the other hand, a higher weight on the constraints produces a smoother model at the expense of the resolution. A good choice for the weight factor can be established by analyzing the variance over a large range of  $\lambda$ . The variance is given by

$$\sigma^2 = \frac{\|\underline{A}\underline{m} - \underline{d}\|^2}{N_d - N_m}, \quad (5.16)$$

where  $N_d$  is the number of data points, and  $N_m$  is the number of model parameters resolved, which is given by the trace of the resolution matrix [Tarantola, 1987, p. 201]. If the model is completely resolved,  $N_m$  is the number of model parameters itself, otherwise it is less. Figure 5.7a demonstrates the dependence of the variance on the weight factor using the synthetic data set. The lower segment of the curve is formed by relatively unconstrained solutions. But even though the variance is small, data noise strongly affects the solution,

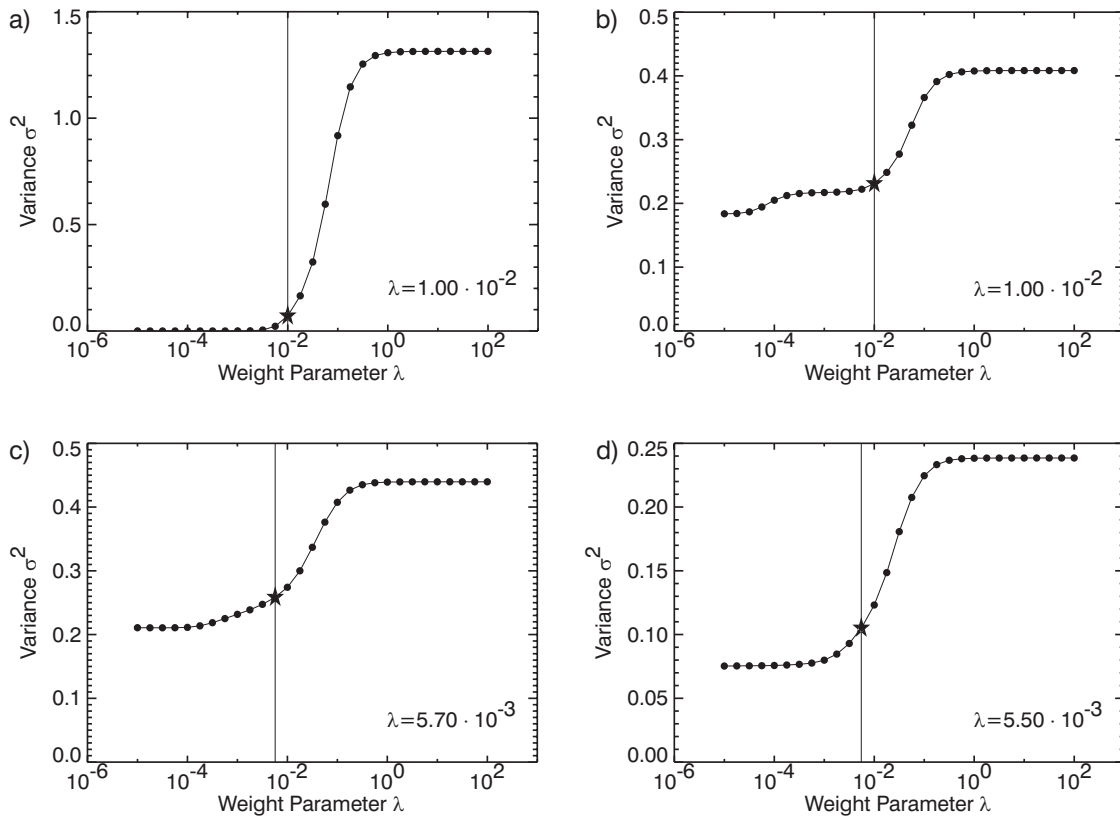


**Figure 5.7:** The dependence of the variance of the solution on the weight factor for each of the model/data combinations utilized in Figure 5.5. (a) Synthetic data inverted with the Volland-Stern drift pattern. The other graphs demonstrate the dependence of the variance on the weight factor obtained by inverting the MPA data, using convection models by (b) Volland-Stern, (c) McIlwain E5D, and (d) Weimer 96. The actual weight factors used for the inversions shown in Figure 5.5 are marked with a star in each plot.

rendering it unreliable [Phillips and Fehler, 1991; Bernabini and Cardarelli, 1997]. On the other hand the upper segment lies well above the noise level but the solution takes little account of the data. A steep increase in variance separates the segments. The range of most appropriate weight factors is found in the lower segment of this increase, where the data have a large impact on the inversion result, and the effect of the noise on the solution is reduced to a minimum. A reasonable value of  $\lambda = 10^{-2}$  is marked with a star in Figure 5.7a. The resolution of each cell, obtained from the corresponding diagonal element in the resolution matrix  $\underline{R}$  is shown in Figure 5.8a. Cells with a resolution higher than 0.2, representing regions of better confidence, are grey-shaded. The resolution of the Volland-Stern inversion for the chosen smoothing operator is reasonable at all local times over a wide radial distance range. Exceptions are the region very near the Earth and a narrow belt around geosynchronous orbit.

### 5.7 Application and Discussion

In this section the technique developed above is applied to the MPA statistics of the phase space density for the year 1997. The resulting inverted hydrogen densities for the three different convection models are shown in Figures 5.5b–5.5d. The choice for the weight factor and the resolution are presented in Figures 5.7b–5.7d and 5.8b–5.8d, respectively. The formats of these panels are the same as those described above for the inversion of the synthetic data set (Figures 5.5a, 5.6, 5.7a, and 5.8a). The interpretation of the inversion results below focuses on the regions of good confidence shown in Figure 5.9 (resolution  $\geq 0.2$ ), which have been extracted from Figure 5.5 using the resolution values of Figure 5.8.

The neutral hydrogen densities obtained with the Volland-Stern electric potential (Figure 5.9b) agree reasonably well with the Chamberlain model near geosynchronous orbit between approximately  $4 R_E$  and  $6 R_E$  where drift paths from a wide range of proton energies contribute to the solution. The inverted densities earthward of this region are considerably less than predicted by the Chamberlain model. In some cells even negative values (white numbers) are obtained. Since no positivity constraints are applied, negative densities are allowed in the mathematical solution even though they are unphysical. However, the innermost densities as well as some of the densities at geosynchronous orbit are not very well determined since their resolution is substantially lower (cf. Figure 5.8b). The low resolution in these regions is the consequence of very few trajectories sampling them. Cells near Earth and at geosynchronous orbit are only partially probed, leading to low resolution numbers.

The interpretation of the model solution shown in Figure 5.9b can be difficult since it emerged from a multitude of drift paths. Nevertheless, the results can be qualitatively explained by focusing on some single trajectories probing the regions of interest. The particle paths through the inner magnetosphere depend strongly on their energy. The region near geosynchronous orbit is sampled predominantly by higher-energy trajectories that drift from the night- to the dayside within a few hours, as illustrated by the example in Figure 5.10a. The particle losses simulated by modeling these rapid drifts through a Cham-



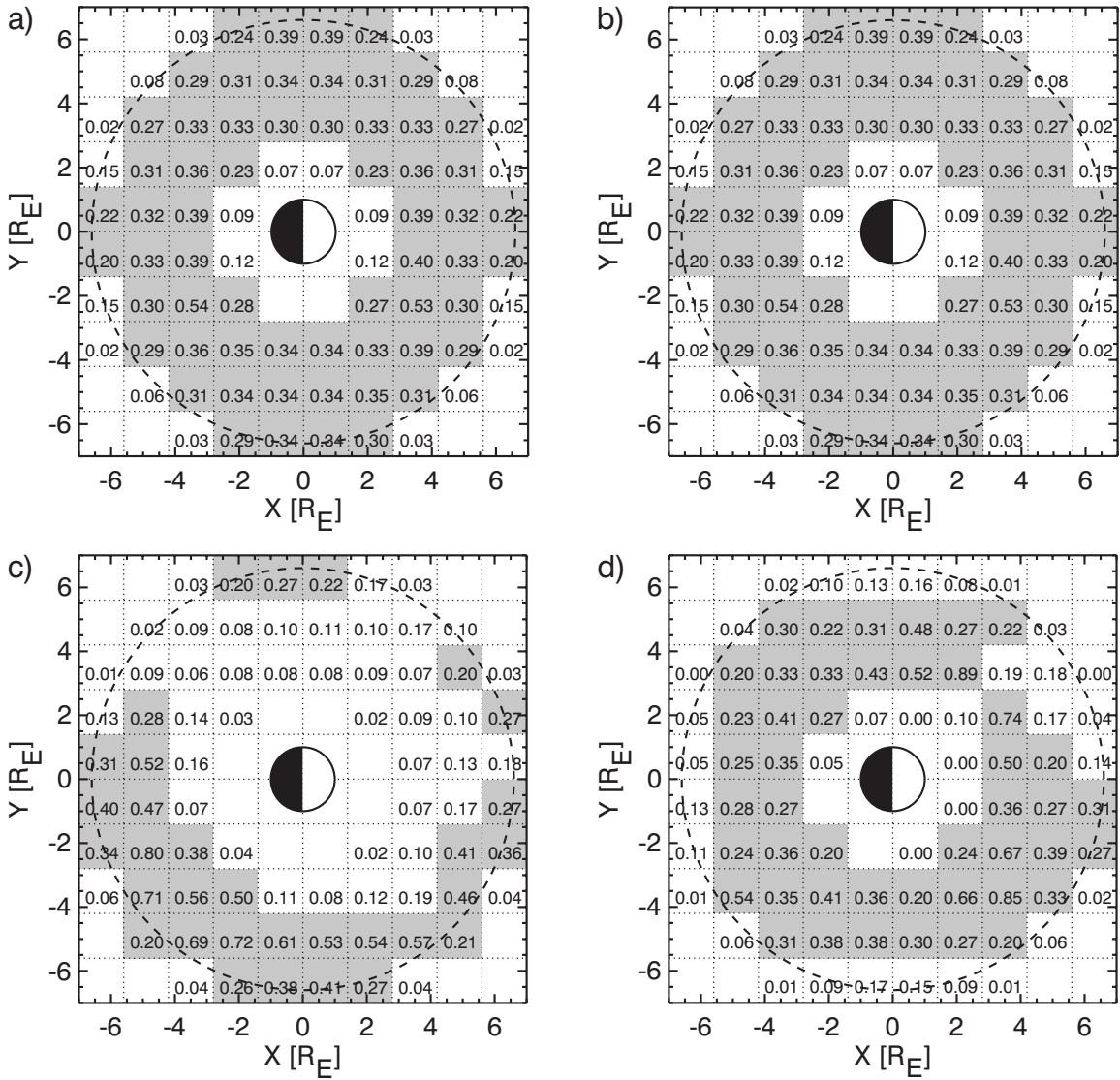


**Figure 5.8:** The resolution matrix measures how well the inverted cell densities are determined independently from their neighbors. It depends on the drift pattern as well as the weight of the smoothing operator. Corresponding to Figure 5.5 the resolutions shown are for (a) the synthetic data set with the Volland-Stern convection model ( $\lambda = 1.0 \cdot 10^{-2}$ ), (b) statistical MPA data set with the Volland-Stern convection model ( $\lambda = 1.0 \cdot 10^{-2}$ ), (c) MPA data with McIlwain E5D convection ( $\lambda = 5.7 \cdot 10^{-3}$ ), and (d) MPA data with Weimer 96 convection ( $\lambda = 5.5 \cdot 10^{-3}$ ). Resolutions of higher confidence ( $\geq 0.2$ ) are grey-shaded.

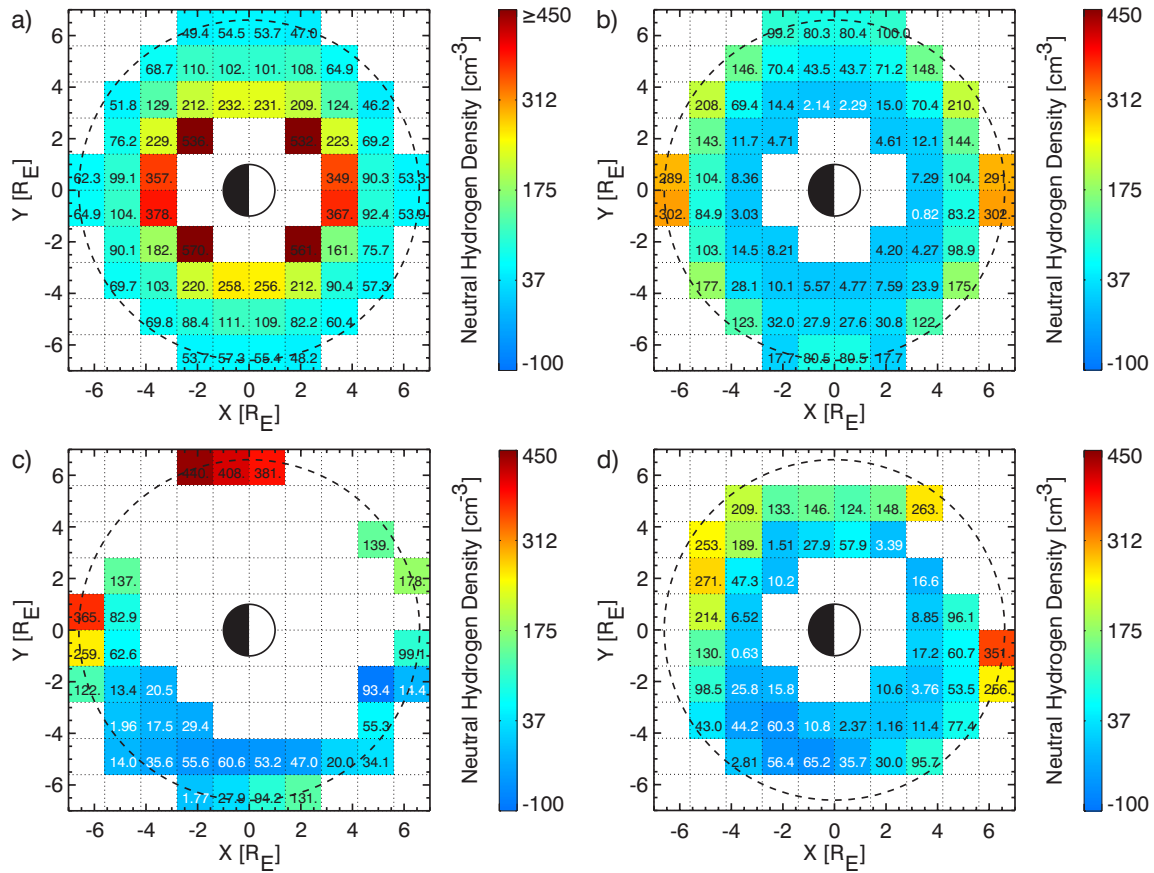


**Figure 5.9:** Neutral hydrogen densities of good confidence (resolution  $\geq 0.2$ ) extracted from Figure 5.5 using the resolution values of Figure 5.8. The graphs are shown by analogy to Figure 5.5: (a) Synthetic data inverted with the Volland-Stern drift pattern. The other graphs show the densities derived by inverting the MPA data, using convection models by (b) Volland-Stern, (c) McIlwain E5D, and (d) Weimer 96.

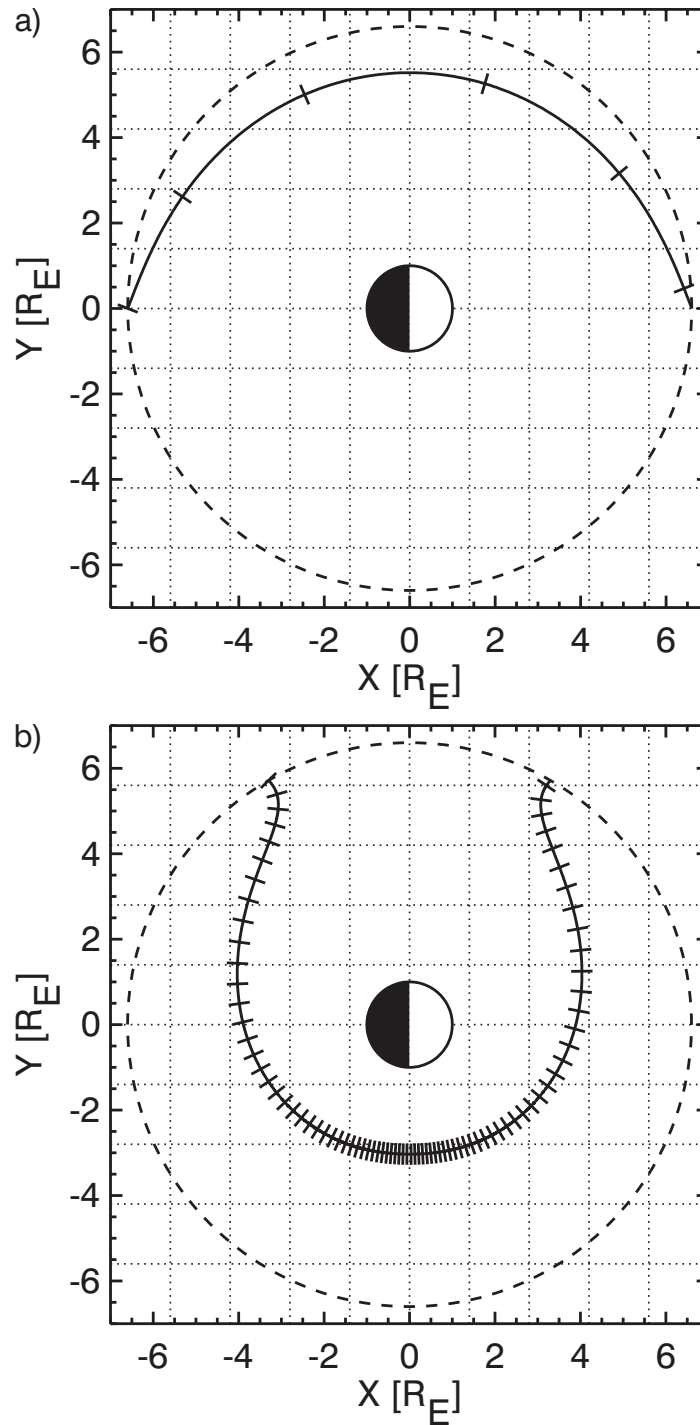


**Figure 5.10:** Sample drift paths calculated from a Volland-Stern electric potential and a magnetic dipole for  $Kp=3$  and a shielding factor of  $\gamma=2$ . The tick marks along the trajectories are spaced in one hour intervals. (a) 10,647 eV proton trajectory entering the geosynchronous region at local midnight. The drift time to local noon is approximately five hours. (b) 969 eV protons injected at 2000 LT. The drift to the dayside takes more than 80 hours.

## 5 Particle Tomography of the Inner Magnetosphere

---

berlain exosphere are small and comparable to the geosynchronous observations. In contrast, lower-energy particles drift more slowly and tend to penetrate more deeply toward the Earth, resulting in drift times inside the geosynchronous region of up to several days (cf. Figure 5.10b). In a Chamberlain exosphere, particles on these trajectories experience high losses since they reside for long periods of time in a dense neutral region near the Earth where charge exchange reactions occur more frequently. However, the MPA observations do not reflect such large reductions of the phase space density. In fact, the simulated particle losses are more than three orders of magnitude larger than the measured ones. This discrepancy explains the low hydrogen densities of the model solution in the near-Earth region: In order for the model to reproduce the observed small decreases in phase space density, the charge exchange rates close to the Earth where the particles spend most of their time have to be fairly small, implying low hydrogen densities in the inner region. The negative density values (white numbers in Figure 5.9b) imply the presence of particle sources as can be seen from (5.5). Since the charge exchange cross section and the thermal speed are positive quantities, negative values of the density will cause the phase space density in a cell to increase. This can only be accomplished if particles are added at the particular location. In the model solution particle sources are needed to balance excessive charge exchange losses encountered in other regions.

The hydrogen density distributions calculated using more sophisticated electric potential models do not exhibit a better correspondence to the Chamberlain model. The good confidence region of the McIlwain E5D inversion, shown in Figure 5.9c, stretches along the dawnside magnetosphere from about local midnight to noon. The most prominent differences between the model solutions obtained from the Volland-Stern and the McIlwain electric potentials are the strongly negative hydrogen densities in the morning sector obtained with the McIlwain model which can also be interpreted as evidence for the presence of particle sources. Figure 5.11 shows a sample proton drift path with an energy of 969 eV at  $Kp=2$ . The trajectory intersects geosynchronous orbit at 2300 LT and 0730 LT. Comparing the average flux levels at these two locations (cf. Figure 5.1d) it is evident that a flux increase would need to occur during the drift, indicating a source population along the path, as the inversion finds.

The high densities at geosynchronous orbit near dusk in Figure 5.9c can be disregarded since only fractions of these cells are probed by trajectories, leading to inaccurate determination of the neutral distribution in this region. Furthermore, most of the densities in the afternoon and evening sector are poorly resolved due to parallel orientation of the majority of the trajectories, a characteristic that adds little information to the system.

The hydrogen density distribution derived with the Weimer convection electric field model is shown in Figure 5.9d and shows features similar to those obtained with the other convection models. A fair agreement with the Chamberlain model is found between 4 and 6  $R_E$  in a region stretching along the duskside from the afternoon sector to a few hours past local midnight. The negative densities in the morning sector are again evidence for sources as described above. Similar to the Volland-Stern inversion, the resolution in the near-Earth region and at geosynchronous orbit is typically unsatisfactory for the above men-

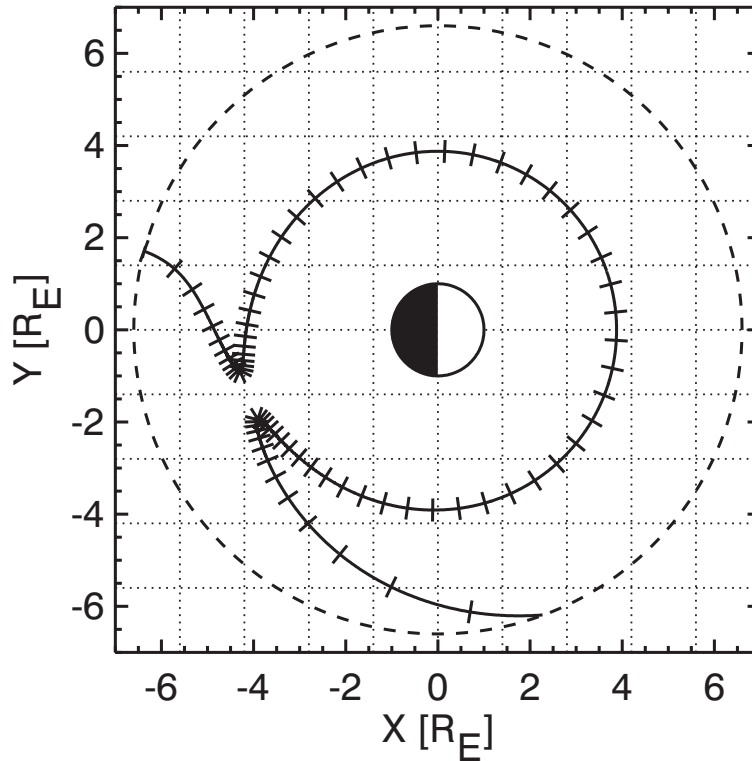


**Figure 5.11:** 969 eV proton drift path calculated from the McIlwain E5D electric potential and a magnetic dipole for  $Kp=2$ . The particle enters the geosynchronous region at 2300 LT, and the local time of the exit point is 0730 LT. The tick marks along the trajectory are spaced in one hour intervals.

tioned reasons (cf. Figure 5.8d).

A recurring feature in the model solutions is the low-density region close to the Earth. These findings are contradictory to the Chamberlain model which predicts large hydrogen densities in the near-Earth region. Several factors may contribute to this discrepancy. For one, the hydrogen geocorona is not as stationary as treated by the Chamberlain model but rather known to have a local time [e.g., *Hodges, 1994*] and a solar cycle dependency [e.g., *Breig et al., 1985*], which are not considered by the model. Furthermore, the *Rairden et al.* parameterization of the Chamberlain model utilizes four years of Ly  $\alpha$  photon data measured by three imaging photometers aboard the DE 1 spacecraft. The instrument calibration was assumed to be constant over time. The variability of the hydrogen density profile due to model assumptions and degradation of the instrument sensitivity was estimated by *Rairden et al.* between  $\pm 20\%$  and  $\pm 30\%$ . The uncertainty of the Chamberlain model may thus allow for lower neutral densities in the inner region. However, the discrepancies in the tomographic inversions are typically larger than this margin.

A more likely explanation of the low densities inferred from the inversions is that the assumed convection models do not well describe the drift trajectories probing the near-Earth

region. Since the observed losses along the respective drift paths are far less than expected, it is quite possible that the particles do not actually penetrate as deeply toward the Earth as calculated from these models. For example, a stronger shielding would cause particles to pass the Earth at greater distances. Furthermore, the convection pattern and resulting drift trajectories were determined under the premise of steady-state convection, which is unlikely to hold for drift durations of several days. In fact, there is good evidence that the convection is often bursty, on timescales of hours and even minutes. The strongly negative density values obtained with the McIlwain E5D and the Weimer 96 convection models point to considerable particle sources in the dawn region, questioning the validity of the steady-state convection patterns obtained with these models. Moreover, using the electric field models in the near-Earth region, I may be using these models beyond their appropriate limits. In order to obtain more accurate results in this region, a better description of the transport in the vicinity of the Earth is needed. Besides the deficiencies of the convection models, the statistics also contain a source of error since the sorting parameter  $Kp$  is a rather coarse description of the convection. Over a full year period, flux data from a wide range of actual convection strengths are averaged in each LT- $Kp$  bin.

### 5.8 Summary and Conclusions

A tomographic inversion technique has been developed to determine the neutral exospheric hydrogen distribution in the inner magnetosphere from geosynchronous particle data. Calculating the proton drift trajectories inside the geosynchronous region from various electric potential models and a dipolar magnetic field, the particle losses along the trajectories can be estimated, for comparison with yearly-averaged phase space density statistics compiled at geosynchronous orbit. Assuming that there are no sources and that the only losses are due to charge exchange reactions between protons and neutral hydrogen atoms, the neutral atom distribution inside the geosynchronous region can be tomographically inverted from the observed losses.

For all convection models examined, the tomography of the MPA data yields very different results from previously established models of the geocorona, e.g. the Chamberlain model. The differences are primarily due to the deeply penetrating trajectories of low-energy protons. Assuming the trend of the Chamberlain model to be correct, I am left with the conclusion that at least one of my model assumptions is incorrect. I believe that the most likely possibility is that the drift models used do not describe the trajectories well enough. The parameterization of the Weimer model shows that the electric potential and thus the drift paths are determined by more than just  $Kp$ . Moreover, the transport may not be well described by the averaged picture, especially during times of high geomagnetic activity when the particle motion is more impulsive. In such a case it may also be that the use of statistical data is not entirely appropriate. Finally, charge exchange reactions with atoms other than hydrogen, additional loss processes such as Coulomb collisions and pitch angle scattering, as well as particle sources such as ionospheric outflow may need to be included

## *5 Particle Tomography of the Inner Magnetosphere*

---

in the algorithm to obtain more accurate results.

In this chapter, tomographic inversion has been introduced as a new data analysis tool in space physics. Although it is unlikely that the neutral densities I have derived are an accurate description of the hydrogen exosphere, the technique provides interesting results with respect to the physics of plasma convection in the inner magnetosphere. With the advent of better observational constraints on the neutral density, this technique offers a potential capability for probing the charged particle transport into and through the inner magnetosphere. The remote-sensing ability of this technique represents a useful tool for multi-spacecraft missions such as CLUSTER and CONSTELLATION.

# 6 Expansion of the Geosynchronous Studies

The work presented in chapters 3 through 5 has inspired many other studies that have been carried out by myself or in close collaboration with others. The purpose of this chapter is to summarize these efforts.

## 6.1 Plasma Sheet Access to the Inner Magnetosphere

The statistical test of the drift paradigm in chapter 3 explored the access conditions applied only to geosynchronous orbit. By mapping flux measurements of a polar orbiting spacecraft along the magnetic field lines to the equatorial plane, it is possible to expand this test to the whole of the inner magnetosphere. Using data from the POLAR satellite, *Friedel et al.* [2001] not only demonstrated an excellent agreement of the POLAR electron observations with the geosynchronous studies of this thesis but also showed the validity of the Alfvén layer paradigm throughout much of the inner magnetosphere.

The POLAR spacecraft has an elliptical orbit  $\sim 1.8$  to  $9R_E$  at  $86^\circ$  inclination. The spacecraft traverses the inner-region field lines four times each orbit, at different magnetic local times (MLT) and at different magnetic latitudes. All MLT are covered within half a year, and the field lines threading POLAR's orbit cover virtually the whole of the magnetosphere. Figure 6.1 shows the equatorial crossing points of the field lines threading the position of POLAR for one whole year (1997). For the field line mapping process the Tsyganenko 87  $Kp$  dependent magnetic field [Tsyganenko, 1987] is used as the external magnetic field and the internal field is represented by a tilted dipole.

Particle data from the HYDRA plasma instrument [Scudder et al., 1995] for the period March 1996 through December 1998 are used for the study. HYDRA measures the full ion and electron distribution functions at sub-spin resolution ( $< 6$  s) for the energy range of 20–20,000 eV. Furthermore, data from the magnetic field instrument MFE [Russell et al., 1995] are used to calculate in-situ values for the first adiabatic invariant  $\mu$  for the locally mirroring population:

$$\mu = \frac{E_k}{B}, \quad (6.1)$$

where  $E_k$  is the energy of the locally mirroring particle population, and  $B$  is the in-situ



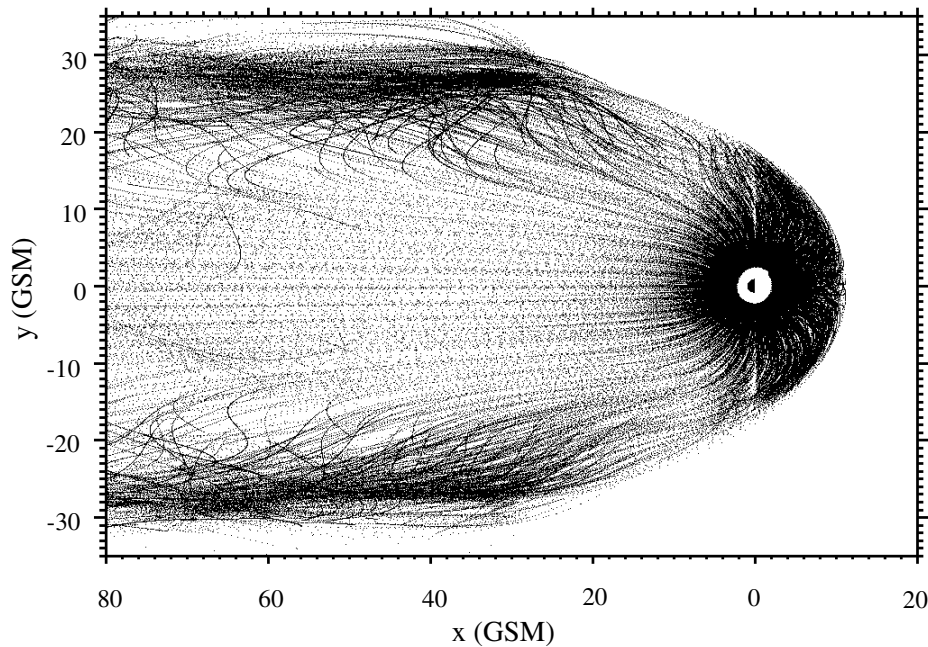


**Figure 6.1:** Equatorial crossings in GSM coordinates of the field lines threading POLAR's orbit during 1997 (from *Friedel et al.* [2001]).

magnitude of the magnetic field strength. Since  $\mu$  is conserved along the field line (and anywhere else), this also represents the equatorial  $\mu$  of the particle.

All particles with a given value for the magnetic moment  $\mu$  drift together and should thus be organized by the Alfvén layers. The results for electrons with  $\mu = 1.0$  eV/nT and  $\mu = 10.0$  eV/nT are shown in Figures 6.2 and 6.3, respectively. A brief glance at these two figures reveals a remarkable agreement between the populated regions and the Alfvén boundaries. As  $\mu$  decreases, electrons can penetrate deeper into the magnetosphere. As  $Kp$  increases, the Alfvén boundaries move closer to the Earth, also allowing deeper access. All  $\mu$  show increasing losses as the particles drift toward the dayside. The ion data, not shown here, in general do not organize as well by the Alfvén boundaries as the electron data. This is most likely related to the more complex nature of the ion drift trajectories.

A “slice” of the HYDRA data taken at geosynchronous orbit is illustrated in Figure 6.4. It shows excellent agreement with the previous statistics of the MPA data in chapter 3. However, the statistics of the HYDRA data are poorer due to the smaller database. A complete discussion of these results can be found in *Friedel et al.* [2001].

### 6.2 Solar Cycle Dependence of the MPA Observations

While the first statistical analysis of the year 1996 was performed, some of the data products were in the process of being regenerated. The Unix ASCII files, which are used throughout

## 6 Expansion of the Geosynchronous Studies

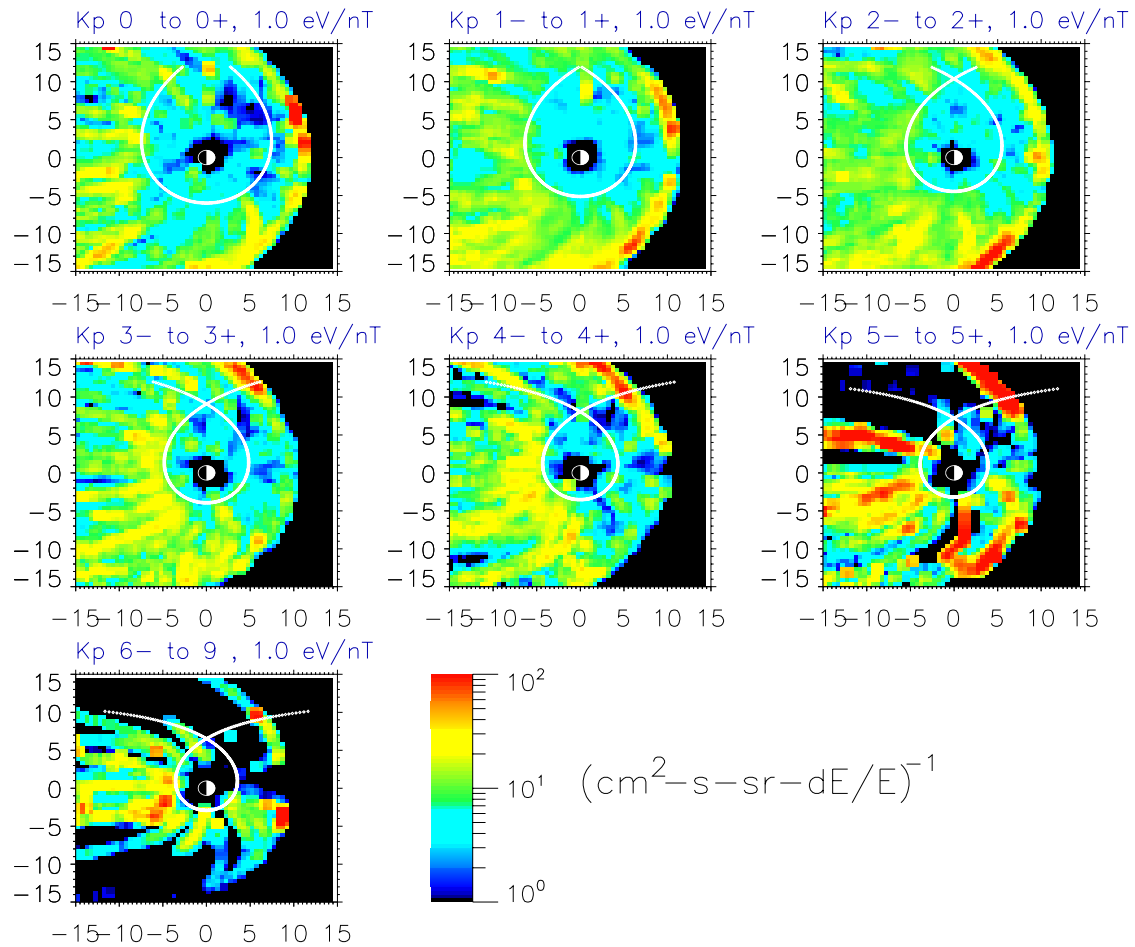


**Figure 6.2:** Average flux for electrons with  $\mu = 1.0$  eV/nT. The  $\mu$  value corresponds to an energy of about 125 eV at geosynchronous orbit (from *Friedel et al.* [2001]).

this thesis, were also affected by this procedure. Consequently, data were only available for a few years at that time. The reprocessing of the database has recently been completed, and the full data set consisting of over 30 satellite years spread over an eleven year period is now accessible. This extended time span is ideal for evaluating the statistical behavior of fluxes and moments during a complete solar cycle. The interpretation of the results of this analysis is still part of my ongoing research. However, selected results are presented here to demonstrate potential future research opportunities of the MPA data set.

Figure 6.5 shows the yearly averaged electron density as a function of local time and  $Kp$  from 1990 to 2000. The statistics are shown in the same format as previously introduced in chapter 3. A brief glance at the figure illustrates that the electron densities during times of solar maximum ( $\sim 1990, 2000$ ) are at least 50% higher than during solar minimum years ( $\sim 1995, 1996$ ). On the other hand, the proton densities, displayed in Figure 6.6 for the years 1995 through 2000, do not exhibit the same solar cycle variations. The proton densities

## 6 Expansion of the Geosynchronous Studies

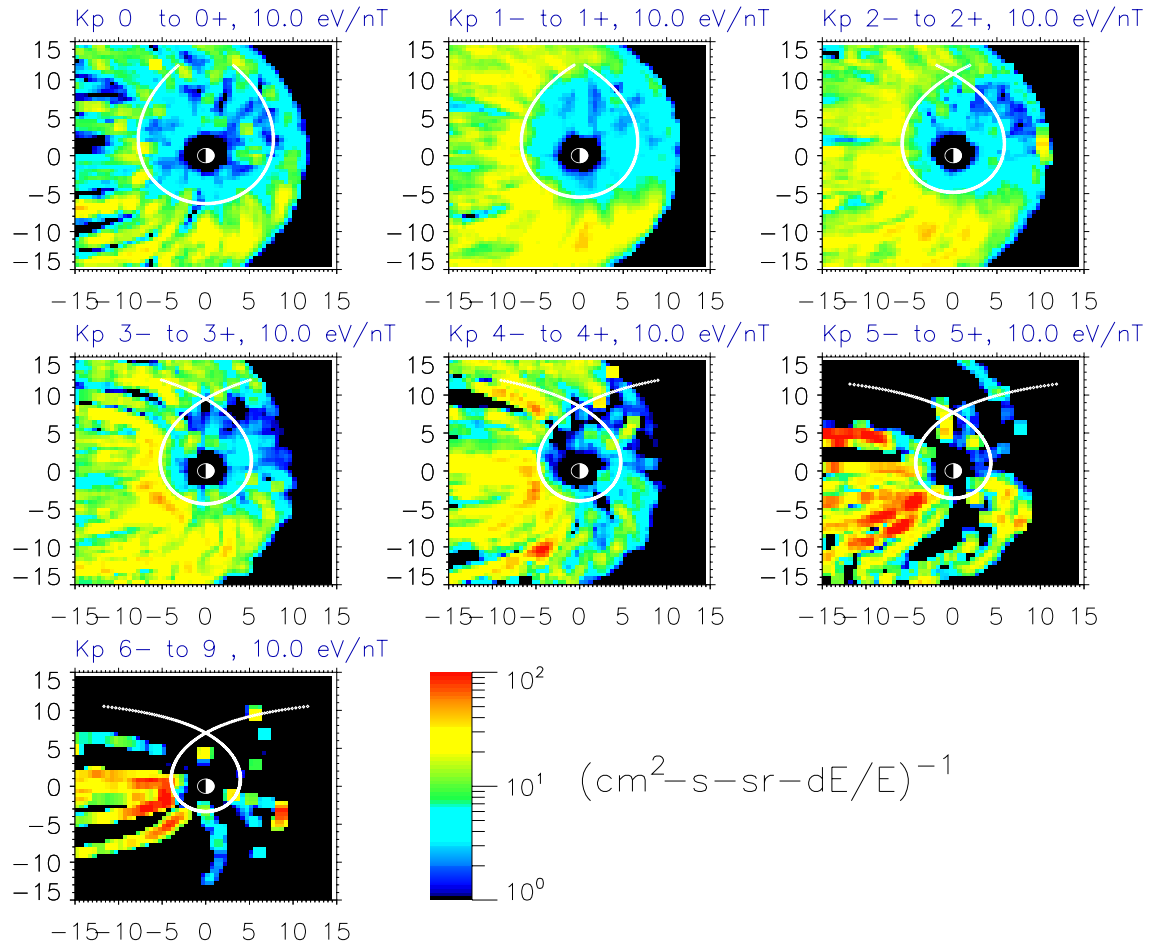


**Figure 6.3:** Average flux for electrons with  $\mu = 10.0$  eV/nT. The  $\mu$  value corresponds to an energy of about 1 keV at geosynchronous orbit (from *Friedel et al.* [2001]).

shown cover only the second half of the most recent solar cycle for the following reason: A degradation of the high-voltage power supplies in the MPAs launched during the first half of the solar cycle reduced the energy range of these instruments to  $\lesssim 20$  keV. Consequently, the high-energy tail of the charged particle populations of both ions and electrons cannot be measured by these instruments. For electrons, the reduced number of available energy channels usually does not affect the calculation of moments in the plasma sheet since the bulk of the electron population can be found in the energy range of up to a few hundred eV. By comparison, the ion population of the plasma sheet generally exhibits temperatures of several thousand eV and are thus much hotter than the electrons. Therefore, the count rates of the upper energy channels of the MPA instrument form an essential contribution in the calculation of proton moments. The proton densities computed without the high-energy component are thus meaningless and therefore not included in this study.

At this time, there is no explanation for the apparent differences in the solar cycle vari-

## 6 Expansion of the Geosynchronous Studies

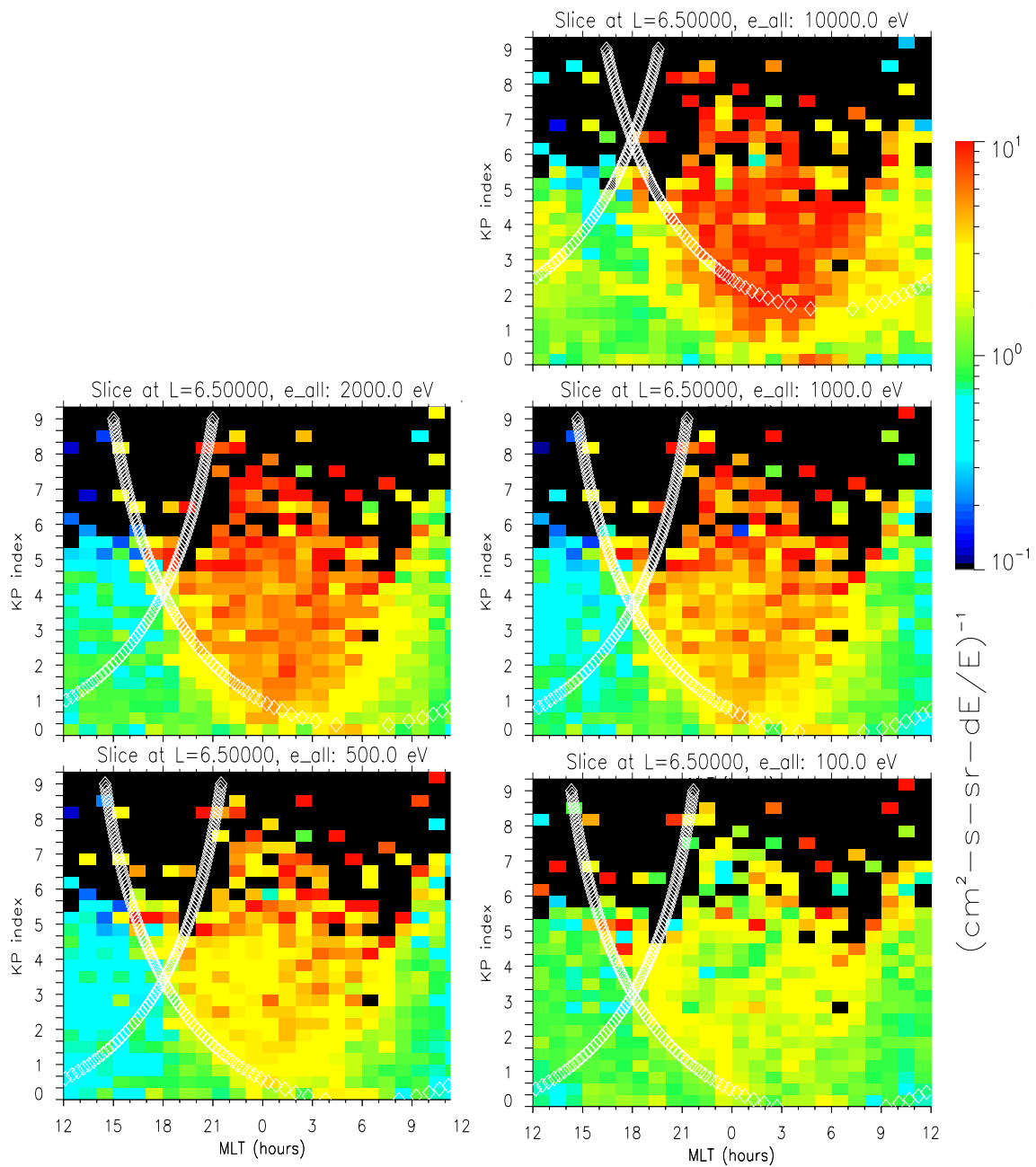


**Figure 6.4:** Geosynchronous slice of the electron fluxes from the POLAR HYDRA instrument (from *Friedel et al. [2001]*).

## 6 Expansion of the Geosynchronous Studies

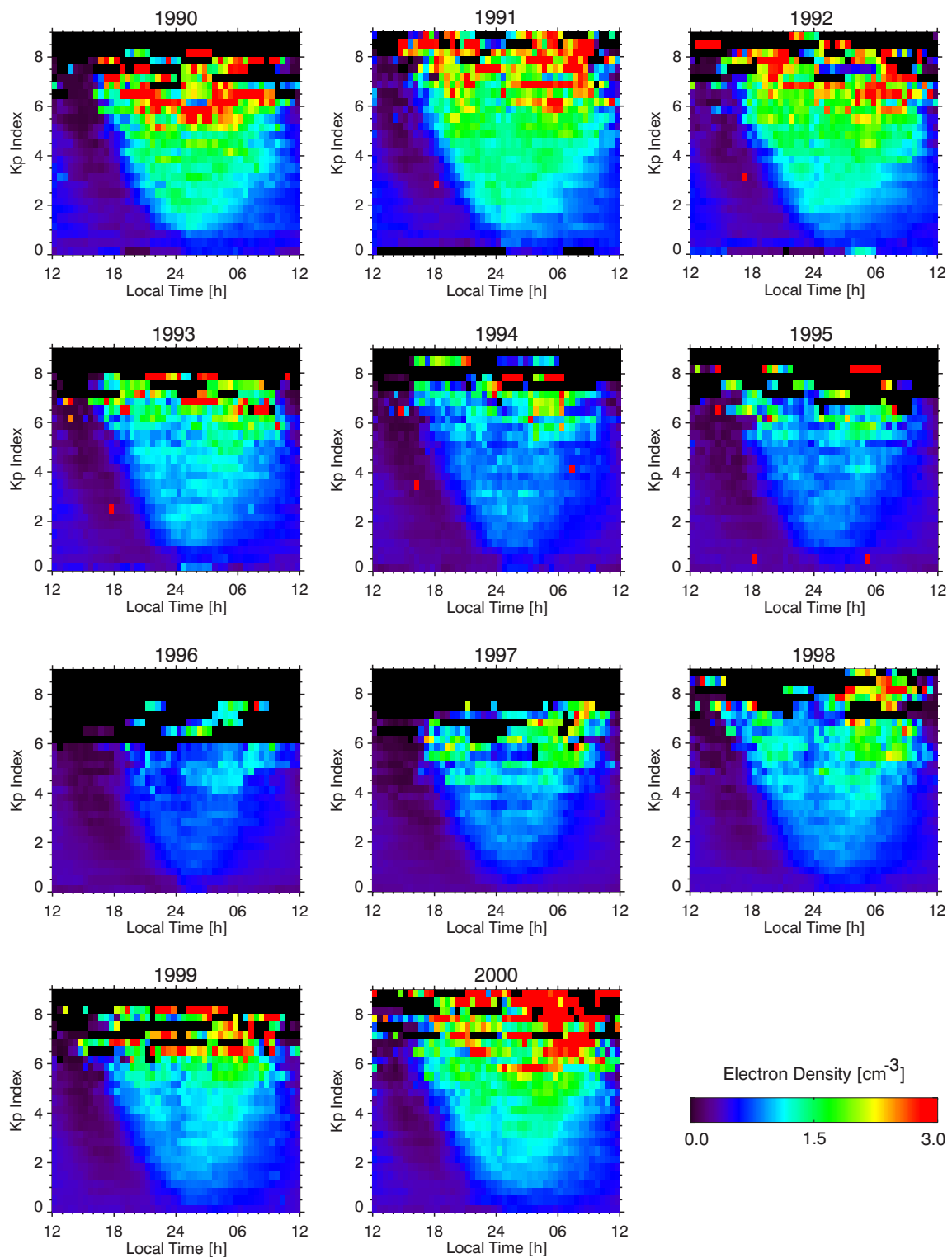


**Figure 6.5:** Geosynchronous electron density from 1990 to 2000, presented as a function of local time and  $Kp$  (cf. Figure 3.9b).

## 6 Expansion of the Geosynchronous Studies

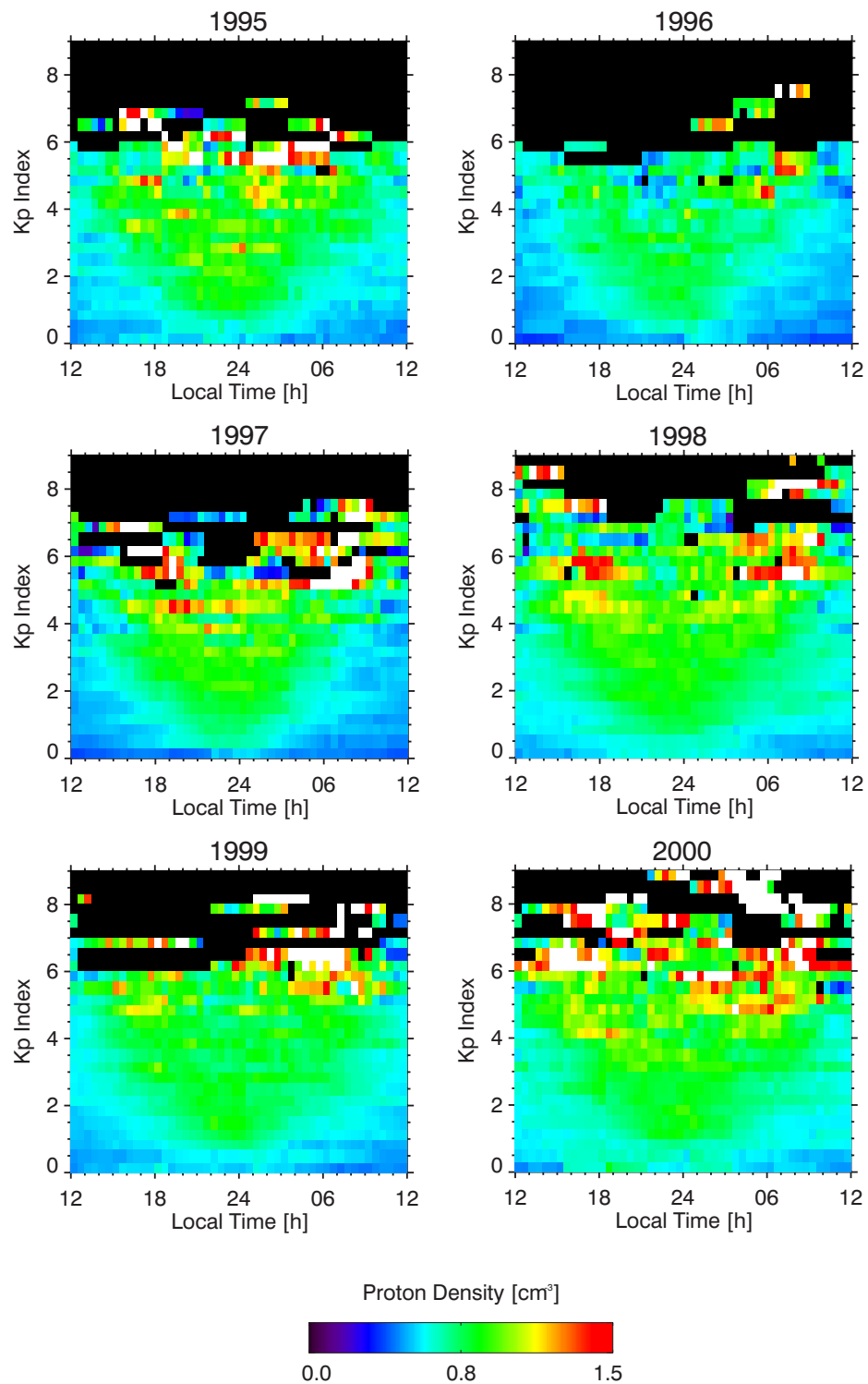


**Figure 6.6:** Geosynchronous proton density from 1995 to 2000, presented as a function of local time and  $K_p$  (cf. Figure 3.9a).

ations of electron and proton densities in the plasma sheet. Since the charge neutrality of the plasma has to be conserved, false assumptions in the moments calculations may be the origin of these differences. As mentioned in section 2.5, the phase space density, which is integrated to obtain the number density, is derived from the differential fluxes under the premise that all ions are protons. In reality, the plasma composition in the inner magnetosphere also includes ions of other species such as, for example, oxygen and helium. Singly ionized oxygen from ionospheric sources contributes significantly to the total number density in the inner magnetosphere [e.g., *Hamilton et al.*, 1988], especially during solar and geomagnetic activity [e.g., *Young et al.*, 1982; *Daglis et al.*, 1993]. Since the atomic mass of species other than protons are not taken into consideration, the MPA densities are only lower estimates of the true densities. For the same reason, a relative change in the composition of the plasma may conceal the existence of a solar cycle dependent proton density. This composition effect and the implications of the solar cycle variations of the plasma sheet particles will be addressed in a future study.

### 6.3 The Upper Cutoff Energy of the Electron Plasma Sheet as a Measure of Magnetospheric Convection Strength

The  $Kp$  dependent Alfvén layer model was introduced in chapter 3 to predict the access of plasma sheet material to geosynchronous orbit. In a study by *Thomsen et al.* [2001] this procedure is reversed to predict the strength of magnetospheric convection from the access of the plasma sheet to geosynchronous orbit.

Under fairly steady magnetospheric conditions, a satellite in geosynchronous orbit moving from the afternoon sector into the evening sector typically encounters the lower-energy plasma sheet electrons first, followed by successively higher energies at later local times. This behavior is not only true in a statistically averaged sense as illustrated in Figure 6.7, but in many individual orbits as well. In the quasi-steady drift model used in this thesis,

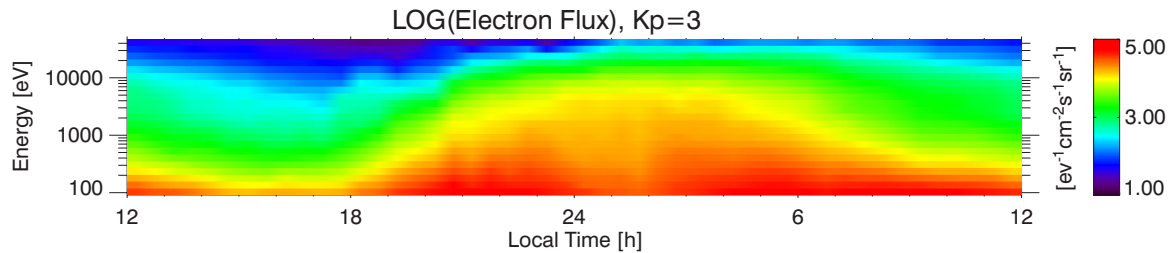


**Figure 6.7:** Average differential electron flux spectrogram for  $Kp = 3$  obtained from the statistical analysis described in chapter 3.

the sharp upper edge of the electron plasma sheet energy distribution represents the local separatrix between open and closed drift paths. In other words, this cutoff energy is the energy above which no fresh plasma sheet electrons have access to the satellite location from

drift paths open to the tail. Since, as shown in Figure 3.4, the locations of the Alfvén layers for different energies depend on the strength of the convection electric field, the value of the plasma sheet cutoff energy at a given local time must also depend on the strength of the convection. Therefore the upper cutoff in the electron spectrum measured at each point in geosynchronous orbit (at least for evening locations) can be used to infer the strength of the convection in near-real-time. A detailed description of this technique can be found in *Thomsen et al.* [2001].

### 6.4 Interpretation of Observations of Magnetic Storms by the Alfvén Layer Paradigm

The application of the near-real-time monitor for the convection strength described in the previous section demonstrates the usefulness of the  $Kp$  dependent drift model not only in a statistical sense but also with limitations on a single event basis. A study by *Korth et al.* [2000] further applied the model to observations of magnetic storms by the CRRES<sup>1</sup> satellite to infer information on the source of ring current ions.

The CRRES satellite had an elliptical,  $18.1^\circ$  inclination orbit with a period of 9 hours and 52 minutes. CRRES covered the regions up to  $L=8$ , giving an  $L$  profile twice an orbit, at magnetic latitudes mostly within  $20^\circ$  of the magnetic equator. The orbit apogee precessed from the prenoon sector at launch (August 1990) to the early dusk sector at the end of the mission (October 1991).

*Korth et al.* [2000] examined three magnetic storms observed by CRRES in the dawn, midnight, and dusk sector of the magnetosphere. They found that the Alfvén boundaries consistently match the observed access of ions from the magnetotail to the inner magnetosphere and thus identified the plasma sheet as the source of the ring current ions. Furthermore, due to the unique configuration of drift paths and Alfvén layers at the dawnside it was possible to identify an inner magnetospheric source of ionospheric ions during the main phase of the storm, and it was shown that this source represents only a minor contribution to the ring current.

---

<sup>1</sup>Combined Release and Radiation Effects Satellite.



## 7 Summary and Outlook

This thesis represents a comprehensive analysis of the geosynchronous plasma environment. It is based on plasma data measured by the Magnetospheric Plasma Analyzer (MPA) instruments that are fielded on five of the Los Alamos geosynchronous satellites. The MPA instruments are electrostatic analyzers measuring energy per charge distributions of electrons and ions in the energy range between about 1 eV/ $q$  and approximately 40 keV/ $q$ . The MPA energy range covers the bulk of the particle populations in the terrestrial magnetosphere including the plasma sheet population that this thesis focuses on.

In a statistical study, a whole year's worth of plasma data from three spacecraft have been analyzed to determine the dependence of proton and electron fluxes at geosynchronous altitudes on local time and the geomagnetic activity as given by  $Kp$ . When displayed as a function of LT and  $Kp$ , the fluxes exhibit distinct boundaries, which on the nightside are consistent with a global pattern of particle drift through the magnetosphere. A Hamiltonian energy conservation approach combined with the  $(U, B, K)$  coordinate transformation has been used to obtain the Alfvén layers, which are the boundaries between open and closed drift trajectories in the magnetosphere. On the nightside, the theoretical boundaries and the observations are in remarkably good agreement with each other, demonstrating the statistical suitability of the simple convection model, which consisted of a Volland-Stern electric potential and a dipolar magnetic field. The diminished fluxes on the dayside are not solely access-related, but rather suggest that the plasma sheet particles experience significant losses as they drift around the Earth. For electrons, these losses are most likely due to auroral precipitation while charge exchange with exospheric neutrals is the most important loss process for the ions.

A consecutive study generalized the analysis of the Alfvén boundaries to numerical global convection models. Numerical techniques as opposed to analytic expressions have the advantage of allowing the use of arbitrary, empirical electric potential and magnetic field models that may be more accurate than simple analytical models. The models surveyed included electric potential models by McIlwain, Sojka, Heppner-Maynard, and Weimer as well as magnetic field models by McIlwain and Tsyganenko. However, the calculations in this thesis have shown that the models examined do not provide a better representation of the observed statistical flux boundaries than does the simple Volland-Stern and dipole model.

In the last part of this thesis, a tomographic inversion technique was developed to determine the exospheric neutral hydrogen distribution in the inner magnetosphere from geosynchronous particle data. Proton drift trajectories in the inner magnetosphere were calculated

## 7 Summary and Outlook

---

from various electric potential models and a dipole magnetic field. The losses along the trajectories were then estimated by comparison with the yearly-averaged differential flux statistics that were previously compiled at geosynchronous orbit. Afterwards the atomic hydrogen distribution inside the geosynchronous region was inverted from the observed losses on the assumption that there are no sources and that charge exchange reactions between protons and exospheric neutral hydrogen are the only loss process. For all convection models examined, the tomography of the MPA data yields very different results from previously established models of the geocorona. Deeply penetrating trajectories of low-energy protons, which may not be well-described by the drift models, were identified as the primary cause for these differences. Furthermore, the neglect of possible particle sources may also have contributed to the discrepancies. Such sources would reduce the derived loss rate, causing the neutral densities to be underestimated. Future work includes an evaluation of the source regions. The tomography algorithm may be further improved by incorporating loss processes other than charge exchange, such as Coulomb collisions and pitch angle scattering into the loss cone. However, including these processes would further decrease the losses that can be attributed to charge exchange and is thus unlikely to improve the comparison with the expected neutral atom densities.

In the meantime others have followed up on the research of this thesis and expanded the geosynchronous studies in close collaboration. Using the POLAR HYDRA data we have shown that the drift paradigm is valid throughout much of the inner magnetosphere, and the similarity of single orbit data with the statistical averages allows us to use the Los Alamos satellites as near-real-time monitors for the strength of magnetospheric convection. The variation of the plasma sheet characteristics with the solar cycle has not been fully evaluated yet and will be addressed in the future.

# Bibliography

- Alfvén, H., Some properties of magnetospheric neutral surfaces, *J. Geophys. Res.*, *73*, 4379–4381, 1968.
- Alfvén, H., and C.-G. Fälthammar, *Cosmical Electrodynamics*, Oxford University Press, New York, 1963.
- Anderson, D. E., R. R. Meier, R. R. Hodges, and B. A. Tinsley, Hydrogen Balmer alpha intensity distributions and line profiles from multiple scattering theory using realistic geocoronal models, *J. Geophys. Res.*, *92*, 7619–7642, 1987.
- Bame, S. J., D. J. McComas, M. F. Thomsen, B. L. Barraclough, R. C. Elphic, and J. P. Glore, Magnetospheric plasma analyzer for spacecraft with constrained resources, *Rev. Sci. Instrum.*, *64*, 1026–1033, 1993.
- Barnett, C. F., Atomic data for fusion. Volume 1: Collisions of H, H<sub>2</sub>, He, and Li atoms and ions with atoms and molecules, *Tech. Rep. ORNL-6086/V1*, Oak Ridge National Laboratory, Oak Ridge, TN 37831, 1990.
- Bartels, J., The standardized index, *K<sub>s</sub>*, and the planetary index, *K<sub>p</sub>*, *IATME Bull. 12b*, p. 97, IUGG Pub. Office, Paris, 1949.
- Baumjohann, W., and R. A. Treumann, *Basic Space Plasma Physics*, Imperial College Press, London, 1997.
- Bernabini, M., and E. Cardarelli, Variable damping factors in travel time tomography, *J. Appl. Geophys.*, *38*, 131–141, 1997.
- Birkeland, K., Expédition Norvégienne 1899–1900 pour l'étude des aurores boréales, *Skr. Nor. Vidensk. Akad. Kl. I Mat. Naturvidensk. Kl., No. 1*, 1901.
- Birn, J., M. F. Thomsen, J. E. Borovsky, G. D. Reeves, D. J. McComas, and R. D. Belian, Characteristic plasma properties during dispersionless substorm injections at geosynchronous orbit, *J. Geophys. Res.*, *102*, 2309–2324, 1997.
- Borovsky, J. E., M. F. Thomsen, D. J. McComas, T. E. Cayton, and D. J. Knipp, Magnetospheric dynamics and mass flow during the November 1993 storm, *J. Geophys. Res.*, *103*, 26,373–26,394, 1998.

## *Bibliography*

---

- Breig, E. L., S. Sanatani, and W. B. Hanson, Thermospheric hydrogen: The long-term solar influence, *J. Geophys. Res.*, *90*, 5247–5260, 1985.
- Burke, W. J., A. G. Rubin, and D. A. Hardy, Banded electron structures in the plasmasphere, *J. Geophys. Res.*, *100*, 7759–7769, 1995.
- Carpenter, D. L., Whistler studies of the plasmopause in the magnetosphere, 1, Temporal variations in the position of the knee and some evidence for plasma motions near the knee, *J. Geophys. Res.*, *71*, 693–709, 1966.
- Carpenter, D. L., and C. G. Park, On what ionospheric workers should know about the plasmopause-plasmasphere, *Rev. Geophys. Space Phys.*, *11(1)*, 133–154, 1973.
- Carrington, R. C., Description of a singular appearance seen in the Sun on September 1, 1859, *Mon. Not. R. Astron. Soc.*, *20*, 13–15, 1860.
- Chamberlain, J. W., Planetary coronae and atmospheric evaporation, *Planet. Space Sci.*, *11*, 901–960, 1963.
- Chamberlain, J. W., Charge exchange in a planetary corona: Its effect on the distribution and escape of hydrogen, *J. Geophys. Res.*, *82*, 1–9, 1977.
- Chapman, S., and J. Bartels, *Geomagnetism*, vol. II, Oxford University Press, New York, 1940.
- Chapman, S., and V. C. A. Ferraro, A new theory of magnetic storms, *Nature*, *126*, 129–130, 1930.
- Chapman, S., and V. C. A. Ferraro, A new theory of magnetic storms, I, The initial phase, *J. Geophys. Res.*, *36*, 77–97, 171–186, 1931.
- Chapman, S., and V. C. A. Ferraro, A new theory of magnetic storms, I, The initial phase (continued), *J. Geophys. Res.*, *37*, 147–156, 421–429, 1932.
- Chappell, C. R., Recent satellite measurements of the morphology and dynamics of the plasmasphere, *Rev. Geophys.*, *10*, 951–979, 1972.
- Chappell, C. R., K. K. Harris, and G. W. Sharp, The morphology of the bulge region of the plasmasphere, *J. Geophys. Res.*, *75*, 3848–3861, 1970.
- Chen, A. J., and J. M. Grebowsky, Plasma tail interpretations of pronounced detached plasma regions measured by OGO 5, *J. Geophys. Res.*, *79*, 3851–3855, 1974.
- Chen, M. W., L. R. Lyons, and M. Schulz, Simulations of phase space distributions of storm time proton ring current, *J. Geophys. Res.*, *99*, 5745–5759, 1994.

## *Bibliography*

---

- Cole, K. D., Theory of some quiet magnetospheric phenomena related to the geomagnetic tail, *Nature*, *211*, 1385–1387, 1966.
- Cowley, S. W. H., Magnetosphere-ionosphere interactions: A tutorial review, in *Magnetospheric Current Systems*, *Geophys. Monogr. Ser.*, vol. 118, edited by S. Ohtani, R. Fujii, M. Hesse, and R. L. Lysak, pp. 91–106, AGU, Washington, 2000.
- Cummings, W. D., P. J. Coleman, and G. L. Siscoe, Quiet day magnetic field at ATS-1, *J. Geophys. Res.*, *76*, 926–932, 1971.
- Daglis, I. A., E. T. Sarris, and B. Wilken, AMPTE/CCE CHEM observations of the ion population at geosynchronous altitudes, *Ann. Geophys.*, *11*, 685–696, 1993.
- Davis, T. N., and M. Sugiura, Auroral electrojet activity index *AE* and its universal time variations, *J. Geophys. Res.*, *71*, 785, 1966.
- DeForest, S. E., and C. E. McIlwain, Plasma clouds in the magnetosphere, *J. Geophys. Res.*, *76*, 3587–3611, 1971.
- Eastman, T. E., B. Popielawska, and L. A. Frank, Three-dimensional plasma observations near the outer magnetospheric boundary, *J. Geophys. Res.*, *90*, 9519–9539, 1985.
- Ejiri, M., Trajectory traces of charged particles in the magnetosphere, *J. Geophys. Res.*, *83*, 4798–4810, 1978.
- Ejiri, M., R. A. Hoffman, and P. H. Smith, The convection electric field model for the magnetosphere based on EXPLORER 45 observations, *J. Geophys. Res.*, *83*, 4811–4815, 1978.
- Elphic, R. C., L. A. Weiss, M. F. Thomsen, and D. J. McComas, Evolution of plasmaspheric ions at geosynchronous orbit during times of high geomagnetic activity, *Geophys. Res. Lett.*, *23*, 2189–2192, 1996.
- Elphic, R. C., M. F. Thomsen, and J. E. Borovsky, The fate of the outer plasmasphere, *Geophys. Res. Lett.*, *24*, 365–368, 1997.
- Elphic, R. C., M. F. Thomsen, J. E. Borovsky, and D. J. McComas, The inner edge of the electron plasma sheet: Empirical models of boundary location, *J. Geophys. Res.*, *104*, 22,679–22,693, 1999.
- Fok, M.-C., J. U. Kozyra, and A. F. Nagy, Lifetime of ring current particles due to Coulomb collisions in the plasmasphere, *J. Geophys. Res.*, *96*, 7861–7867, 1991.
- Fok, M.-C., T. E. Moore, and M. E. Greenspan, Ring current development during storm main phase, *J. Geophys. Res.*, *101*, 15,311–15,322, 1996.

## *Bibliography*

---

- Friedel, R. H. W., H. Korth, M. G. Henderson, M. F. Thomsen, and J. D. Scudder, Plasma sheet access to the inner magnetosphere, *J. Geophys. Res.*, *106*, 5845–5858, 2001.
- Funsten, H. O., Private communication, 2000.
- Garner, T. W., R. A. Wolf, R. W. Spiro, and M. F. Thomsen, First attempt at assimilating data to constrain a magnetospheric model, *J. Geophys. Res.*, *104*, 25,145–25,152, 1999.
- Garrett, H. B., The charging of spacecraft surfaces, *Rev. Geophys.*, *19*, 577–616, 1981.
- Garrett, H. B., and A. G. Rubin, Spacecraft charging at geosynchronous orbit – Generalized solution for eclipse passage, *Geophys. Res. Lett.*, *5*, 865–868, 1978.
- Garrett, H. B., D. C. Schwank, and S. E. Deforest, A statistical analysis of the low-energy geosynchronous plasma environment, I, Electrons, *Planet. Space Sci.*, *29*, 1021–1044, 1981a.
- Garrett, H. B., D. C. Schwank, and S. E. Deforest, A statistical analysis of the low-energy geosynchronous plasma environment, II, Ions, *Planet. Space Sci.*, *29*, 1045–1060, 1981b.
- Gauß, C. F., *Werke*, vol. 5, 2 ed., Königliche Gesellschaft der Wissenschaften, Göttingen, 1877.
- Gilbert, W., *De Magnete*, translated by P. F. Mottelay, Dover Publications, New York, 1958.
- Gold, T., Motions in the magnetosphere of the Earth, *J. Geophys. Res.*, *64*, 1219–1224, 1959.
- Goldstein, H., *Classical Mechanics*, 2nd ed. ed., Addison-Wesley Publishing Company, Reading, Mass., 1980.
- Gosling, J. T., J. R. Asbridge, S. J. Bame, and W. C. Feldman, Effects of a long entrance aperture upon the azimuthal response of spherical section electrostatic analyzers, *Rev. Sci. Inst.*, *49*, 1260–1268, 1978.
- Gosling, J. T., M. F. Thomsen, and R. C. Anderson, A cookbook for determining essential transmission characteristics of spherical section electrostatic analyzers, *Tech. Rep. LA-10147-M*, Los Alamos National Laboratory, Los Alamos, NM 87545, 1984.
- Graham, G., *Philos. Trans. R. Soc. London*, No. 383, 96, 1724.
- Gussenhoven, M. S., D. A. Hardy, and W. J. Burke, DMSP/F2 electron observations of equatorward auroral boundaries and their relationship to magnetospheric electric fields, *J. Geophys. Res.*, *86*, 768–778, 1981.
- Gussenhoven, M. S., D. A. Hardy, and N. Heinemann, Systematics of the equatorward diffuse auroral boundary, *J. Geophys. Res.*, *88*, 5692–5708, 1983.

## Bibliography

---

- Hamilton, D. C., G. Gloeckler, F. M. Ipavich, W. Stüdemann, B. Wilken, and G. Kremser, Ring current development during the great geomagnetic storm of February 1986, *J. Geophys. Res.*, *93*, 14,343–14,355, 1988.
- Henderson, M. G., G. D. Reeves, K. R. Moore, H. E. Spence, A. M. Jorgensen, J. F. Fennell, J. B. Blake, and E. C. Roelof, Energetic neutral atom imaging with the POLAR CEPPAD/IPS instrument: Initial forward modeling results, *Phys. Chem. Earth (C)*, *24*, 203–208, 1999.
- Heppner, J. P., and N. C. Maynard, Empirical high-latitude electric field models, *J. Geophys. Res.*, *92*, 4467–4489, 1987.
- Hilmer, R. V., and G. P. Ginet, A magnetospheric specification model validation study: Geosynchronous electrons, *J. Atmos. Terr. Phys.*, *62*, 1275–1294, 2000.
- Hodges, R. R., Monte Carlo simulation of the terrestrial hydrogen exosphere, *J. Geophys. Res.*, *99*, 23,229–23,247, 1994.
- Hodges, R. R., and E. L. Breig, Ionosphere – exosphere coupling through charge exchange and momentum transfer in hydrogen-proton collisions, *J. Geophys. Res.*, *96*, 7697–7708, 1991.
- Hughes, W. J., The magnetopause, magnetotail, and magnetic reconnection, in *Introduction to Space Physics*, edited by M. G. Kivelson and C. T. Russell, pp. 227–287, Cambridge University Press, New York, 1995.
- Iijima, T., and T. A. Potemra, The amplitude distribution of field-aligned currents at northern high latitudes observed by Triad, *J. Geophys. Res.*, *81*, 2165–2174, 1976a.
- Iijima, T., and T. A. Potemra, Large-scale characteristics of field-aligned currents associated with substorms, *J. Geophys. Res.*, *81*, 5971–5979, 1976b.
- J Jeans, J. H., *The Dynamical Theory of Gases*, 4th ed. ed., Dover Publications Inc., New York, 1954.
- Jordanova, V. K., L. M. Kistler, J. U. Kozyra, G. V. Khazanov, and A. F. Nagy, Collisional losses of ring current ions, *J. Geophys. Res.*, *101*, 111–126, 1996.
- Jordanova, V. K., C. J. Farrugia, L. Janoo, J. M. Quinn, R. B. Tobert, K. W. Ogilvie, R. P. Lepping, J. T. Steinberg, D. J. McComas, and R. D. Belian, October 1995 magnetic cloud and accompanying storm activity: Ring current evolution, *J. Geophys. Res.*, *103*, 79–92, 1998.
- Kerns, K. J., D. A. Hardy, and M. S. Gussenhoven, Modeling of convection boundaries seen by CRRES in 120-eV to 28-keV particles, *J. Geophys. Res.*, *99*, 2403–2414, 1994.

## Bibliography

---

- Kertz, W., *Einführung in die Geophysik*, vol. 1, BI Wissenschaftsverlag, Mannheim, 1992.
- Kistler, L. M., and D. J. Larson, Testing electric and magnetic field models of the storm-time inner magnetosphere, *J. Geophys. Res.*, *105*, 25,221–25,231, 2000.
- Kistler, L. M., F. M. Ipavich, D. C. Hamilton, G. Gloeckler, B. Wilken, G. Kremser, and W. Stüdemann, Energy spectra of the major ion species in the ring current during geomagnetic storms, *J. Geophys. Res.*, *94*, 3579–3599, 1989.
- Kivelson, M. G., Physics of space plasmas, in *Introduction to Space Physics*, edited by M. G. Kivelson and C. T. Russell, pp. 27–57, Cambridge University Press, New York, 1995.
- Korth, A., R. H. W. Friedel, C. G. Mouikis, J. F. Fennell, J. R. Wygant, and H. Korth, Comprehensive particle and field observations of magnetic storms at different local times from the CRRES spacecraft, *J. Geophys. Res.*, *105*, 18,729–18,740, 2000.
- Kozyra, J. U., M.-C. Fok, E. R. Sanchez, D. S. Evans, D. C. Hamilton, and A. F. Nagy, The role of precipitation losses in producing the rapid early recovery phase of the Great Magnetic Storm of February 1986, *J. Geophys. Res.*, *103*, 6801–6814, 1998a.
- Kozyra, J. U., V. K. Jordanova, J. E. Borovsky, M. F. Thomsen, D. J. Knipp, D. S. Evans, D. J. McComas, and T. E. Cayton, Effects of a high-density plasma sheet on ring current development during the November 2–6, 1993, magnetic storm, *J. Geophys. Res.*, *103*, 26,285–26,305, 1998b.
- Lawrence, D. J., M. F. Thomsen, J. E. Borovsky, and D. J. McComas, Measurements of early and late-time plasmasphere refilling as observed from geosynchronous orbit, *J. Geophys. Res.*, *104*, 14,691–14,704, 1999.
- Liemohn, M. W., G. V. Khazanov, and J. U. Kozyra, Banded electron structure formation in the inner magnetosphere, *Geophys. Res. Lett.*, *25*, 877–880, 1998.
- Liemohn, M. W., J. U. Kozyra, V. K. Jordanova, G. V. Khazanov, M. F. Thomsen, and T. E. Cayton, Analysis of early phase ring current recovery mechanisms during geomagnetic storms, *Geophys. Res. Lett.*, *26*, 2845–2848, 1999.
- Lindemann, F. A., Note on the theory of magnetic storms, *Philos. Mag.*, *38*, 669–684, 1919.
- Maurice, S., M. F. Thomsen, D. J. McComas, and R. C. Elphic, Quiet time densities of hot ions at geosynchronous orbit, *J. Geophys. Res.*, *103*, 17,571–17,585, 1998.
- Mayaud, P. N., *Derivation, Meaning, and Use of Geomagnetic Indices*, *Geophys. Monogr. Ser.*, vol. 22, AGU, Washington, 1980.



## Bibliography

---

- Maynard, N. C., and A. J. Chen, Isolated cold plasma regions: Observations and their relation to possible production mechanisms, *J. Geophys. Res.*, *80*, 1009–1013, 1975.
- McComas, D. J., S. J. Bame, B. L. Barraclough, J. R. Donart, R. C. Elphic, J. T. Gosling, M. B. Moldwin, K. R. Moore, and M. F. Thomsen, Magnetospheric plasma analyzer: Initial 3-spacecraft observations from geosynchronous orbit, *J. Geophys. Res.*, *98*, 13,453–13,465, 1993.
- McComas, D. J., R. C. Elphic, M. B. Moldwin, and M. F. Thomsen, Plasma observations of magnetopause crossings at geosynchronous orbit, *J. Geophys. Res.*, *99*, 21,249–21,255, 1994.
- McIlwain, C. E., Plasma convection in the vicinity of the geosynchronous orbit, in *Earth's Magnetospheric Processes*, edited by B. M. McCormac, pp. 268–279, D. Reidel, Norwell, Mass., 1972.
- McIlwain, C. E., A  $K_p$  dependent equatorial electric field model, *Adv. Space Res.*, *6*(3), 187–197, 1986.
- McIlwain, C. E., and E. C. Whipple, The dynamic behavior of plasmas observed near geosynchronous orbit, *IEEE Trans. Plasma Sci.*, *14*, 874–890, 1986.
- McPherson, D. A., D. P. Cauffman, and W. R. Schober, Spacecraft charging at high-altitudes: SCATHA satellite program, *J. Spacecr. Rockets*, *12*, 621–626, 1975.
- Menke, W., *Geophysical Data Analysis: Discrete Inverse Theory*, Academic Press Inc., Orlando, 1984.
- Mitchell, D. G., Guest editor's introduction, *Tech. Dig.*, vol. 11, Nos. 3 and 4, Johns Hopkins University Applied Physics Laboratory, 11100 Johns Hopkins Road, Laurel, MD 20723, 1990.
- Moldwin, M. B., M. F. Thomsen, S. J. Bame, D. J. McComas, J. Birn, G. D. Reeves, R. Nemzek, and R. D. Belian, Flux dropouts of plasma and energetic particles at geosynchronous orbit during large geomagnetic storms: Entry into the lobes, *J. Geophys. Res.*, *100*, 8031–8043, 1995.
- Neugebauer, M., and C. W. Snyder, Mariner 2 observations of the solar wind, 1, Average properties, *J. Geophys. Res.*, *71*, 4469–4484, 1966.
- Nishida, A., Formation of plasmopause, or magnetospheric plasma knee, by the combined action of magnetospheric convection and plasma escape from the tail, *J. Geophys. Res.*, *71*, 5669–5679, 1966.
- Nishida, A., Geomagnetic  $D_p$  2 fluctuations and associated magnetospheric phenomena, *J. Geophys. Res.*, *73*, 1795–1803, 1968.

## Bibliography

---

- Obayashi, T., and A. Nishida, Large-scale electric field in the magnetosphere, *Space Sci. Rev.*, *8*, 3–31, 1968.
- Ober, D. M., J. L. Horwitz, and D. L. Gallagher, Formation of density troughs embedded in the outer plasmasphere by subauroral ion drift event, *J. Geophys. Res.*, *102*, 14,595–14,602, 1997.
- Paolini, F. R., and G. C. Theodoridis, Charged particle transmission through spherical plate electrostatic analyzers, *Rev. Sci. Inst.*, *38*, 579–588, 1967.
- Phillips, W. S., and M. C. Fehler, Traveltime tomography: A comparison of popular methods, *Geophysics*, *56*, 1639–1649, 1991.
- Pilipp, W. G., and G. Morfill, The formation of the plasma sheet resulting from plasma mantle dynamics, *J. Geophys. Res.*, *83*, 5670–5678, 1978.
- Poincaré, H., Remarques sur une experience de M. Birkeland, *C. R. Acad. Sci.*, *123*, 530–533, 1896.
- Press, W. H., S. A. Teukolsky, W. T. Vetterling, and B. P. Flannery, *Numerical Recipes in FORTRAN*, 2nd ed. ed., Cambridge University Press, New York, 1994.
- Pulkkinen, T. I., D. N. Baker, R. J. Pellinen, J. Büchner, H. E. J. Koskinen, R. E. Lopez, R. L. Dyson, and L. A. Frank, Particle scattering and current sheet stability in the geomagnetic tail during the substorm growth phase, *J. Geophys. Res.*, *97*, 19,283–19,297, 1992.
- Purcell, E. M., The focusing of charged particles by a spherical condenser, *Phys. Rev.*, *54*, 818–826, 1938.
- Quinn, J. M., G. Paschmann, N. Sckopke, V. K. Jordanova, H. Vaith, O. H. Bauer, W. Baumjohann, W. Fillius, G. Haerendel, S. S. Kerr, C. A. Kletzing, K. Lynch, C. E. McIlwain, R. B. Torbert, and E. C. Whipple, EDI convection measurements at 5–6  $R_E$  in the post-midnight region, *Ann. Geophys.*, *17*, 1503–1512, 1999.
- Rairden, R. L., L. A. Frank, and J. D. Craven, Geocoronal imaging with Dynamics Explorer, *J. Geophys. Res.*, *91*, 13,613–13,630, 1986.
- Rich, F. J., and N. C. Maynard, Consequences of using simple analytical functions for the high-latitude convection electric field, *J. Geophys. Res.*, *94*, 3687–3701, 1989.
- Ritchie, R. H., J. S. Cheka, and R. D. Birkhoff, The spherical condenser as a high transmission particle spectrometer, *Nucl. Inst. & Meth.*, *6*, 157–163, 1960.
- Rodgers, F. T., On the theory of the electrostatic Beta-particle analyzer, *Rev. Sci. Inst.*, *22*, 723–726, 1951.

## *Bibliography*

---

- Roederer, J. G., *Physics and Chemistry in Space*, vol. 2, *Dynamics of Geomagnetically Trapped Radiation*, Springer Verlag, New York, 1970.
- Roelof, E. C., Energetic neutral atom image of a storm-time ring current, *Geophys. Res. Lett.*, *14*, 652–655, 1987.
- Roelof, E. C., ENA emission from nearly-mirroring magnetospheric ions interacting with the exosphere, *Adv. Space Res.*, *20*, 361–366, 1997.
- Rostoker, G., J. L. Kisabeth, R. D. Sharp, and E. G. Shelley, The expansive phase of magnetospheric substorms, 2, The response at synchronous altitude of particles of different energy ranges, *J. Geophys. Res.*, *80*, 3557–3570, 1975.
- Rufenach, C. L., R. F. Martin, and H. H. Sauer, A study of geosynchronous magnetopause crossings, *J. Geophys. Res.*, *94*, 15,125–15,134, 1989.
- Russell, C. T., R. C. Snare, J. D. Means, D. Pierce, D. Dearbourne, M. Larson, G. Barr, and G. Le, The GGS/POLAR magnetic field investigation, *Space Sci. Rev.*, *71*, 563–582, 1995.
- Sabine, E., On periodical laws discoverable in the mean effects of the larger magnetic disturbances, *Philos. Trans. R. Soc. London*, *142*, 103–124, 1852.
- Sauvaud, J.-A., and J. R. Winckler, Dynamics of plasma, energetic particles, and fields near synchronous orbit in the nighttime sector during magnetospheric substorms, *J. Geophys. Res.*, *85*, 2043–2056, 1980.
- Scales, J. A., P. Docherty, and A. Gersztenkorn, Regularisation of nonlinear inverse problems: Imaging the near-surface weathering layer, *Inverse Problems*, *6*, 115–131, 1990.
- Schild, M. A., J. W. Freeman, and A. J. Dessler, A source for field-aligned currents at auroral latitudes, *J. Geophys. Res.*, *74*, 247–256, 1969.
- Scudder, J., F. Hunsacker, G. Miller, J. Lobell, T. Zawistowski, K. Ogilvie, J. Keller, D. Chornay, F. Herrero, and R. Fitzenreiter, HYDRA – A 3-dimensional electron and ion hot plasma instrument for the POLAR spacecraft of the GGS mission, *Space Sci. Rev.*, *71*, 459–495, 1995.
- Shaw, P. R., and J. A. Orcutt, Waveform inversion of seismic refraction data and applications to young Pacific crust, *Geophys. J. R. astr. Soc.*, *82*, 375–414, 1985.
- Sheldon, R. B., and J. D. Gaffey, Particle tracing in the magnetosphere: New algorithms and results, *Geophys. Res. Lett.*, *20*, 767–770, 1993.

## Bibliography

---

- Smith, P. H., N. K. Bewtra, and R. A. Hoffman, Motions of charged particles in the magnetosphere under the influence of a time-varying large scale convection electric field, in *Quantitative Modeling of Magnetospheric Processes, Geophys. Monogr. Ser.*, vol. 21, edited by W. P. Olsen, pp. 513–534, AGU, Washington, 1979.
- Snyder, C. W., M. Neugebauer, and U. R. Rao, The solar wind velocity and its correlation with cosmic ray variations and with solar and geomagnetic activity, *J. Geophys. Res.*, *68*, 6361–6370, 1963.
- Sojka, J. J., C. E. Rasmussen, and R. W. Schunk, An interplanetary magnetic field dependent model of the ionospheric convection electric field, *J. Geophys. Res.*, *91*, 11,281–11,290, 1986.
- Southwood, D. J., and S. M. Kaye, Drift boundary approximations in simple magnetospheric convection models, *J. Geophys. Res.*, *84*, 5773–5780, 1979.
- Stern, D. P., Motion of a proton in the equatorial magnetosphere, *J. Geophys. Res.*, *80*, 595–599, 1975.
- Stern, D. P., Large-scale electric fields in the Earth's magnetosphere, *Rev. Geophys. Space Phys.*, *15*(2), 156–194, 1977.
- Strang, G., *Linear Algebra and its Applications*, 3rd ed. ed., Harcourt Brace Jovanovich Publishers, San Diego, 1988.
- Sugiura, M., Hourly values of equatorial *Dst* for the IGY, *Ann. Int. Geophys. Year*, *35*, 49, 1964.
- Svalgaard, L., Polar cap magnetic variations and their relationship with the interplanetary magnetic sector structure, *J. Geophys. Res.*, *78*, 2064–2078, 1973.
- Tarantola, A., *Inverse Problem Theory*, Elsevier Science Publishing Company, New York, 1987.
- Taylor, H. A., H. C. Brinton, and M. W. Pharo, Evidence of contraction of the Earth's thermal plasmasphere subsequent to the solar flare event of 7 and 9 July 1966, *Ann. IQSY*, *3*, 389, 1966.
- Theodoridis, G. C., and F. R. Paolini, The angular response of spherical plate electrostatic analyzers, *Rev. Sci. Inst.*, *40*, 621–631, 1969.
- Thomsen, M. F., S. J. Bame, D. J. McComas, M. B. Moldwin, and K. R. Moore, The magnetospheric lobe at geosynchronous orbit, *J. Geophys. Res.*, *99*, 17,283–17,293, 1994.
- Thomsen, M. F., D. J. McComas, G. D. Reeves, and L. A. Weiss, An observational test of the Tsyganenko (T89a) model of the magnetospheric field, *J. Geophys. Res.*, *101*, 24,827–24,836, 1996.

## Bibliography

---

- Thomsen, M. F., D. J. McComas, J. E. Borovsky, and R. C. Elphic, The magnetospheric trough, in *Geospace Mass and Energy Flow: Results From the International Solar-Terrestrial Physics Program*, *Geophys. Monogr. Ser.*, vol. 104, edited by J. L. Horwitz, D. L. Gallagher, and W. K. Peterson, pp. 355–369, AGU, Washington, 1998.
- Thomsen, M. F., E. Noveroske, J. E. Borovsky, and D. J. McComas, Calculation of moments from measurements by the Los Alamos Magnetospheric Plasma Analyzer, *Tech. Rep. LA-13566-MS*, Los Alamos National Laboratory, Los Alamos, NM 87545, 1999.
- Thomsen, M. F., H. Korth, and R. C. Elphic, The upper cut-off energy of the electron plasma sheet as a measure of magnetospheric convection strength, *J. Geophys. Res.*, submitted, 2001.
- Tinsley, B. A., The diurnal variation of atomic hydrogen, *Planet. Space Sci.*, 21, 686–691, 1973.
- Tinsley, B. A., R. R. Hodges, and R. P. Rohrbaugh, Monte Carlo models for the terrestrial exosphere over a solar cycle, *J. Geophys. Res.*, 91, 13,631–13,647, 1986.
- Toivanen, P. K., Effects of the large-scale electric field on particle drifts in the near-Earth tail, *J. Geophys. Res.*, 102, 2405–2415, 1997.
- Tsyganenko, N. A., Global quantitative models of the geomagnetic field in the cislunar magnetosphere for different disturbance levels, *Planet. Space Sci.*, 35, 1347–1358, 1987.
- Tsyganenko, N. A., A magnetospheric magnetic field model with a warped tail current sheet, *Planet. Space Sci.*, 37, 5–20, 1989.
- Van Allen, J. A., and L. A. Frank, Radiation around the Earth to a radial distance of 107,400 km, *Nature*, 183, 430, 1959.
- Van Allen, J. A., G. H. Ludwig, E. C. Ray, and C. E. McIlwain, Observations of high intensity radiation by satellites 1958 Alpha and Gamma, *Jet Propul.*, 28, 588–592, 1958.
- Vogt, J., and K.-H. Glassmeier, On the location of trapped particle populations in quadrupole magnetospheres, *J. Geophys. Res.*, 105, 13,063–13,071, 2000.
- Volland, H., A semiempirical model of large-scale magnetospheric electric fields, *J. Geophys. Res.*, 78, 171–180, 1973.
- Volland, H., Models of global electric fields within the magnetosphere, *Ann. Geophys.*, 31, 159–173, 1975.
- Volland, H., A model of the magnetospheric electric convection field, *J. Geophys. Res.*, 83, 2695–2699, 1978.

- Weimer, D. R., Models of high-latitude electric potentials derived with a least error fit of spherical harmonic coefficients, *J. Geophys. Res.*, *100*, 19,595–19,607, 1995.
- Weimer, D. R., A flexible, IMF dependent model of high-latitude electric potentials having “space weather” applications, *Geophys. Res. Lett.*, *23*, 2549–2552, 1996.
- Whipple, E. C., (U,B,K) coordinates: A natural system for studying magnetospheric convection, *J. Geophys. Res.*, *83*, 4318–4326, 1978.
- Whipple, E. C., J. S. Halekas, J. D. Scudder, W. R. Paterson, L. A. Frank, R. B. Sheldon, N. C. Maynard, D. R. Weimer, C. T. Russell, K. Tsuruda, H. Hayakawa, and T. Yamamoto, Identification of magnetospheric particles that travel between spacecraft and their use to help obtain magnetospheric potential distributions, *J. Geophys. Res.*, *103*, 93–102, 1998.
- Wing, S., and P. T. Newell, Central plasma sheet ion properties as inferred from ionospheric observations, *J. Geophys. Res.*, *103*, 6785–6800, 1998.
- Wolf, R. A., Magnetospheric configuration, in *Introduction to Space Physics*, edited by M. G. Kivelson and C. T. Russell, pp. 288–329, Cambridge University Press, New York, 1995.
- Wolf, R. A., M. Harel, R. W. Spiro, G. H. Voigt, P. H. Reiff, and C. K. Chen, Computer simulation of inner magnetospheric dynamics for the magnetic storm of July 29, 1977, *J. Geophys. Res.*, *87*, 5949–5962, 1982.
- Wrenn, G. L., J. F. E. Johnson, A. J. Norris, and M. F. Smith, GEOS-2 magnetopause encounters: Low energy (< 500 eV) particle measurements, *Adv. Space Res.*, *1*, 129, 1981.
- Young, D. T., Space plasma particle instrumentation and the new paradigm: Faster, cheaper, better, in *Measurement Techniques in Space Plasmas: Particles, Geophys. Monogr. Ser.*, vol. 102, edited by R. F. Pfaff, J. E. Borovsky, and D. T. Young, pp. 1–16, AGU, Washington, 1998.
- Young, D. T., H. Balsiger, and J. Geiss, Correlations of magnetospheric ion composition with geomagnetic and solar activity, *J. Geophys. Res.*, *87*, 9077–9096, 1982.

# Acknowledgements

The research for this thesis has been conducted at Los Alamos National Laboratory, New Mexico, USA, and during two separate visits to the Institut für Geophysik und Meteorologie der Technischen Universität Braunschweig in Germany. I wish to express my sincere gratitude to Prof. Dr. Karl-Heinz Glaßmeier for his interest and encouragement. The many interesting discussions, his useful advice, and his helpful criticism have been invaluable for this study. I also thank Prof. Dr. Peter Weidelt for providing an independent evaluation of this work.

I am deeply indebted to Dr. Michelle Thomsen for suggesting and funding the research of this thesis, for providing the MPA data, for the comments on this manuscript, as well as for her continuous support during my stay in Los Alamos. Dr. Thomsen has been an excellent mentor, who always took time to explain to me the “secrets” of space physics. The numerous inspiring discussions with her have significantly widened my knowledge in the field.

Furthermore, I wish to thank Drs. Joachim Birn, Joseph Borovsky, Richard Elphic, Michael Henderson, David McComas, and Scott Phillips at Los Alamos National Laboratory for many fruitful discussions. I am especially grateful to Prof. Dr. Elden Whipple at the University of Washington and Prof. Dr. Robert Sheldon at the University of Alabama for providing valuable insight into the  $(U, B, K)$  coordinate system.

My special thanks go to Dorothea Delapp and Evan Noveroske for their assistance with the processing of large amounts of MPA data used in this thesis.

Moreover, I thank the Drs. Reiner Friedel and Axel Korth for their comments on this work and my mother, Ursula Korth, for proofreading the final manuscript.

I further would like thank Eloisa Michel at Los Alamos National Laboratory and Brunhilde Görs at the Institut für Geophysik und Meteorologie for their numerous secretarial efforts. I am indebted to Christiane Stuntebeck for printing and binding this manuscript and for submitting the paperwork to the Technische Universität Braunschweig.

Last but not least I thank my wife Tracie for her continuous support, understanding, and patience during the course of this work.

This work was carried out under the auspices of the U. S. Department of Energy, with partial financial support from the National Aeronautics and Space Administration (NASA), the National Science Foundation (NSF), the Deutsches Zentrum für Luft- und Raumfahrt (DLR), and the German Bundesministerium für Bildung und Wissenschaft under contract 50OC0103.

# Lebenslauf

## Persönliche Daten:

**Name:** Korth  
**Vorname:** Haje  
**Geschlecht:** männlich  
**Geburtsdatum:** 01.11.1971  
**Geburtsort:** Northeim  
**Staatsangehörigkeit:** deutsch  
**Konfession:** evangelisch  
**Familienstand:** verheirated, 2 Kinder

## Schulbildung und Studium

**1978 – 1982** Martin-Luther Grundschule in Northeim  
**1982 – 1984** Thomas-Mann-Schule Orientierungsstufe in Northeim  
**1984 – 1988** Gymnasium Corvinianum in Northeim  
**1988 – 1989** Horlick High School in Racine, Wisconsin, USA  
**1989 – 1991** Gymnasium Corvinianum in Northeim  
**Mai 1991** Allgemeine Hochschulreife  
**1992 – 1994** Grundstudium Physik an der Technischen Universität Braunschweig  
**Okt. 1994** Vordiplom in Physik  
**1994 – 1998** Hauptstudium Physik an der Technischen Universität Braunschweig  
**Jul. 1998** Diplom in Physik  
**Seit Aug. 1998** Promotionsstudium am Los Alamos National Laboratory, Los Alamos, New Mexico, USA

## Berufstätigkeit

**1991 – 1992** Zivildienst im Albert-Schweitzer Krankenhaus in Northeim  
**1992 – 1998** Hilfwissenschaftler am Max-Planck-Institut für Aeronomie, Katlenburg-Lindau  
**1994 – 1998** Hilfwissenschaftler am Institut für Geophysik und Meteorologie der Technischen Universität Braunschweig